Meridional Overturning Circulation in the Tropical Atlantic

On the Meridional Ageostrophic and Geostrophic Transports, and Water Mass Properties

Dissertation

zur Erlangung des Doktorgrades

der Mathematisch-Naturwissenschaftlichen Fakultät

der Christian-Albrechts-Universität zu Kiel

vorgelegt von

Yao Fu

Kiel, 2017

Helmholtz-Zentrum für Ozeanforschung Kiel

Erster Gutachter: Prof. Dr. Peter Brandt
Zweiter Gutachter: Prof. Dr. Arne Biastoch
Datum der mündlichen Prüfung: 16.01.2018
Zum Druck genehmigt: 16.01.2018
Gez.: Prof. Dr. Wolfgang J. Duschl, Dekan

Abstract

The Atlantic meridional overturning circulation (AMOC) plays an important role in the global climate. It consists of northward flows in the upper, intermediate, and bottom water layers, and a southward flow in the deep water layer. Locally, the AMOC can be decomposed into a wind-driven Ekman transport near the surface and a geostrophic transport in the interior. Using hydrographic data, direct velocity observations, satellite and reanalysis wind data, assimilation data, and array-based analysis data, meridional Ekman transports, full-depth overturning volume, heat and freshwater transports, as well as the associated water mass property changes are investigated for the tropical Atlantic in this thesis.

The meridional Ekman volume transport in the tropics, which is driven by the strong trade winds is regarded as the primary ageostrophic component of the AMOC. In general, the Ekman volume transport is estimated from wind stress data. The Ekman heat and salt transports are then derived by combining the Ekman volume transport with sea surface temperature (SST) and salinity (SSS) data. However, unknown vertical structures of the Ekman velocity, upper-ocean temperature, and salinity potentially bias the Ekman volume, heat and salt transports. Zonal hydrographic surveys with direct velocity observations along 14.5° N and 11° S across the Atlantic enable detailed inspection of the directly observed Ekman velocity, and thus the Ekman transports. The derived ageostrophic velocities show an "Ekman spiral"-like structure in the upper 60 to 100 m of the water column. Integrating the ageostrophic velocity zonally along the sections and vertically from the surface to the top of the pycnocline (TTP) yields Ekman transport estimates of 6.2 ± 2.3 Sv at 14.5° N, and -11.7 ± 2.1 Sv at 11° S ("-" denotes southward). This agrees well with the Ekman transport derived from the in-situ wind stress data, and implies that the TTP is a good approximation for the Ekman depth. Additionally, the SST and SSS are found sufficient to represent Ekman layer mean temperature and salinity, and can therefore be used for the Ekman heat and salt transport calculation.

Since most climate models predict a weakening of the AMOC over the 21st century in response to global warming, it is of interest to seek evidence for the weakening of the AMOC from observations. Using repeated trans-Atlantic sections at 14.5° N (1989, 2013) and at 24.5° N (1992, 2015), the full-depth geostrophic component of the AMOC is determined from a box inverse model with surface Ekman transports as ageostrophic constraints. Direct comparison of the water mass properties between the different realizations at the respective latitudes shows that the Antarctic Intermediate Water (AAIW) became warmer and saltier at 14.5° N, and

that the densest Antarctic Bottom Water became lighter, while the North Atlantic Deep Water freshened at both latitudes. The inverse solution shows that the intermediate layer transport at 14.5° N was also markedly weaker in 2013 than in 1989, indicating that the AAIW property changes at this latitude may be related to changes in the circulation. At both latitudes, the AMOC was generally weaker during 2013/2015 than during 1989/1992 (14.7 ± 3.9 vs. 18.6 ± 2.7 Sv at 14.5° N, and 16.9 ± 1.6 vs. 19.2 ± 1.7 Sv at 24.5° N, respectively). However, comparison between the inverse solution, the GECCO2 ocean state estimate, the MOVE and RAPID array data suggests that the observed difference between the two periods may be explained by the strong seasonal to interannual variability of the AMOC rather than a long-term trend.

Nevertheless, the study on the ageostrophic transport also shows that the 14.5° N section is located near the latitudinal maximum climatological meridional Ekman transport in the North Atlantic, which poses the question whether the Ekman transport is particularly relevant at this latitude. Sensitivity experiments of the inverse solution suggest that the overturning structure of the AMOC, as well as the net heat transport across the section are sensitive to the Ekman transport at 14.5° N. Given the strong and variable trade winds driving the meridional Ekman transport and thereby inducing geostrophic anomalies in the upper ocean through isopycnal displacement, the results of the sensitivity experiments emphasize the need for a better knowledge of the Ekman transport to enhance the understanding of the AMOC in the tropics.

Zusammenfassung

Die Atlantische Umwälzzirkulation (engl., Atlantic Meridional Overturning Circulation, AMOC) ist von außerordentlicher Bedeutung für das Weltklima. Sie besteht aus nordwärtigen Strömungen in der Oberflächen-, Zwischenwasser- und Bodenwasserschicht, sowie einer südwärtigen Strömung in der Tiefenwasserschicht. Lokal kann die AMOC in einen windgetriebenen Ekman-Transport nahe der Oberfläche und einen geostrophischen Transport im Ozeaninnern zerlegt werden. Unter Verwendung von hydrographischen Daten, direkten Geschwindigkeitsmessungen, Satelliten- und Reanalysewinddaten, Assimilationsdaten und Analysedaten von Langzeitmessungen aus Tiefseeverankerungen wurden in dieser Arbeit zum einen die meridionale Ekman-transport und Transporte in der gesamten Wassersäule von Wärme, Frischwasser und Volumen im tropischen Atlantik untersucht. Des Weiteren wurden damit einhergehende Änderungen der Wassermasseneigenschaften analysiert.

Der meridionale Ekman-Volumentransport in den Tropen, welcher von starken Passatwinden angetrieben wird, gilt als wichtigste ageostrophische Komponente der AMOC. Im Allgemeinen werden Windstressdaten zur Berechnung des Ekman-Volumentransports verwendet. Die Wärme- und Salztransporte innerhalb der Ekmanschicht werden dann abgeleitet, indem der Ekman-Volumentransport mit den Daten der Meeresoberflächentemperatur (engl., sea surface termperature, SST) und des Meeresoberflächensalzgehalts (engl., sea surface salinity, SSS) kombiniert wird. Dabei ist nicht auszuschließen, dass die unbekannten vertikalen Strukturen der Ekman-Geschwindigkeit, sowie der oberflächennahen Temperatur und des Salzgehalts die Volumen-, Wärme- und Salztransporte innerhalb der Ekmanschicht potentiell beeinflussen. Zonale hydrographische Schnitte mit direkten Geschwindigkeitsbeobachtungen entlang 14,5° N und 11° S im Atlantik ermöglichen hier eine detaillierte Untersuchung der beobachteten Ekman-Geschwindigkeit und damit der Ekman-Transporte. Die daraus abgeleiteten ageostrophischen Geschwindigkeiten in den oberen 60 bis 100 m der Wassersäule ähneln in ihrer Struktur einer "Ekmanspirale". Durch Integration der ageostrophische Geschwindigkeit vom Ostrand zum Westrand und von der Oberfläche bis zur Oberkante der Pycnokline (engl., the top of the pycnocline, TTP) ergibt sich ein Ekman-Transport von 6.2 ± 2.3 Sv bei 14.5° N und -11.7 ± 2.1 Sv bei 11° S ("-" markiert südwärtigen Transport). Dies ist in guter Übereinstimmung mit dem vom Windstress abgeleiteten Ekman-Transport und impliziert, dass die TTP als Schätzung für die Ekman-Tiefe verwendet werden kann. Des Weiteren kann gezeigt werden, dass SST und SSS in guter Näherung der mittleren Temperatur und dem mittleren Salzgehalt inner-

halb der Ekmanschicht entsprechen, und daher für die Berechnung von Ekman-Wärme- und -Salztransporten verwendet werden können.

Als Reaktion auf den Klimawandel sagen viele Klimamodelle eine Schwächung der AMOC über das 21. Jahrhundert vorher. Daher ist es von Interesse, Hinweise für die Schwächung der AMOC in Beobachtungsdaten zu suchen. Unter Verwendung von transatlantischen Schnitten bei 14,5° N (1989, 2013) und bei 24,5° N (1992, 2015) wird die geostrophische Komponente der AMOC mit einem Inversmodell bestimmt. Dabei dienen die Oberflächen-Ekman-Transport als ageostrophische Randbedingung. Ein direkter Vergleich der Wassermasseneigenschaften zwischen den verschiedenen Schiffsschnitten an den jeweiligen Breitengraden zeigt, dass sich das Antarktische Zwischenwasser (engl., Antarctic Intermediate Water, AAIW) bei 14.5° N zwischen 1989 und 2013 erwärmt hat und salzreicher wurde und dass an beiden Breitengraden das dichteste Antarktische Bodenwasser leichter und das nordatlantische Tiefenwasser salzärmer wurde. Die Inverslösung zeigt ausserdem, dass der Transport in der Zwischenwasserschicht bei 14.5° N im Jahr 2013 deutlich schwächer war im vergleich zu 1989. Dies deutet darauf hin, dass die Eigenschaftsänderungen des AAIW entlang dieses Breitengrads mit Veränderungen in der Zirkulation zusammenhängen. Die AMOC war im Zeitraum 1989/1992 generell stärker als im Zeitraum 2013/2015 ($18,6 \pm 2,7$ gegenüber $14,7 \pm 3,9$ Sv bei 14,5° N und $19,2 \pm 1,7$ gegenüber $16,9 \pm 1,6$ Sv bei 24,5° N). Der Vergleich zwischen der Inverslösung, des GECCO2-Modells, der MOVE- und RAPID-Array-Daten deutet jedoch darauf hin, dass die beobachtete Differenz zwischen den beiden Zeiträumen durch die starke saisonale bis zwischenjährliche Variabilität der AMOC und nicht durch einen langfristigen Trend erklärt werden kann.

Die Studie zum ageostrophischen Transport zeigt auch, dass die Messungen bei 14.5° N in der Nähe der geographischen Breite des klimatologischen Maximums des meridionalen Ekman-Transports im Nordatlantik liegt. Dies wirft die Frage auf, ob der Ekman-Transport bei diesem Breitengrad eine besonders starke Rolle für die AMOC spielt. Sensitivitätsexperimente mit dem Inversmodell deuten darauf hin, dass die Umwälzstruktur der AMOC sowie der Netto-Wärmetransport an dieser Breite sensitiv zum meridionalen Ekman-Transport sind. Angesichts der starken und variablen Passatwinde, welche den meridionalen Ekman-Transport antreiben und dadurch geostrophische Anomalien im oberen Ozean durch eine Veränderung der Dichteschichtung hervorrufen, unterstreichen die Ergebnisse der Sensitivitätsexperimente die Notwendigkeit die Dynamik des Ekman-Transports besser zu verstehen, um damit das Verständnis der AMOC in den Tropen zu verbessern.

Contents

1 Introduction

1.1 Motivation and goals

The Atlantic meridional overturning circulation (AMOC), as part of the global overturning circulation, plays an important role in the global climate. By definition, AMOC describes a two-dimensional movement of waters in the meridional and vertical plane, which consists of a double cell with the northward flowing surface and intermediate waters, the southward flowing North Atlantic Deep Water (NADW), and the northward flowing Antarctic Bottom Water (AABW) (*Lozier*, 2012). The warm upper-ocean waters move northward away from the source region across the equator, carrying a large amount of heat to the subpolar North Atlantic, where they release heat to the atmosphere, lose buoyancy, and sink, resulting in the formation of NADW. The NADW then returns as a cold and deep southward flow mainly through the Deep Western Boundary Current (DWBC) and complex interior pathways Lozier2012.

Studies based on observational data show that the meridional heat transport associated with the AMOC amounts to about 1.1-1.5 PW in the tropics (*Hall and Bryden*, 1982; *Friedrichs and Hall*, 1993; *Klein et al.*, 1995; *Johns et al.*, 2011), contributing up to one-quarter to the total poleward heat transport by the ocean and atmosphere required to balance the unevenly distributed net radiation at the top of the atmosphere. Without the redistribution of heat by the coupled ocean-atmosphere system, the temperature difference between the North Pole and the tropical region would be much larger than the difference at present-day climate (*Gill*, 1982). The fifth assessment report of the Intergovernmental Panel on Climate Change (IPCC) concluded that it is very likely for the AMOC to weaken over the 21st century under a continuously warming climate (*Collins et al.*, 2013). Consequently, this would reduce the oceanic heat supply to the North Atlantic, which would eventually give rise to an atmospheric response in terms of stronger and deeper penetration of storms into Europe (*Jacob et al.*, 2005; *Brayshaw et al.*, 2009). Moreover, as the uptake of atmospheric CO_2 is assumed to be strong in the North Atlantic (*Takahashi et al.*, 2009), a weakening AMOC would reduce northward transport of carbon-rich surface waters, affecting the uptake and redistribution of CO_2 in the deep oceans. Given the importance of the AMOC, it seems essential to adequately understand the large-scale motions in the ocean, which would help to enhance the understanding of climate variability and to facilitate prediction of climate changes.

In this thesis, hydrographic data obtained along trans-Atlantic sections at 11° S (occupied

in 2013), 14.5° N (1989 and 2013), and 24.5° N (1992 and 2015) are analysed. In addition, ship-board velocity data, satellite-based and reanalysis wind stress data, assimilation model data, and mooring-based analysis data are used. The focus of this thesis is the AMOC in the tropical region. Dynamically, the AMOC at a certain latitude can be decomposed into surface ageostrophic component, which is the Ekman transport driven by the wind, and interior geostrophic component related to the basin-wide density gradient. The available datasets facilitate the estimation of the meridional ageostrophic and geostrophic components of the AMOC, the analysis of water mass property changes over the past two decades, and a verification whether a weakening of the AMOC is evident from observational data. In the following, observational results and model-based estimations of the AMOC, meridional Ekman transport, and water mass characteristics are introduced with emphasis on the tropical Atlantic, establishing the basis for this thesis.

1.2 Observations and model-based estimates of the AMOC

1.2.1 Early attempts to describe the Atlantic circulation

Over the years, oceanographers have spent tremendous efforts to continuously deepen our understanding of the AMOC. Early attempts to describe the Atlantic circulation at depth were made by *Wüst* (1935) through analysing water mass characteristics, and by *Defant* (1941), who studied the geostrophic circulation in the upper 2000 m. These studies were conducted using data measured during the early Atlantic expeditions (e.g. the Meteor expedition during 1925-1927 and several earlier expeditions). *Wüst* (1935) showed that the NADW flows southward in three layers, while the Subantarctic Intermediate Water and AABW flow northward characterized by a salinity minimum and density maximum, respectively. The horizontal maps of water properties and geostrophic circulation at different depth levels by *Defant* (1941) and *Wüst* (1949, 1957) further illustrated that the water masses spread away from their formation regions mainly within the western boundary currents.

1.2.2 AMOC estimates based on hydrographic data

1.2.2.1 Estimates from hydrography

More quantitative estimations of the AMOC in different regions of the Atlantic were conducted using hydrographic data measured along selected sections. These sections were occupied, for

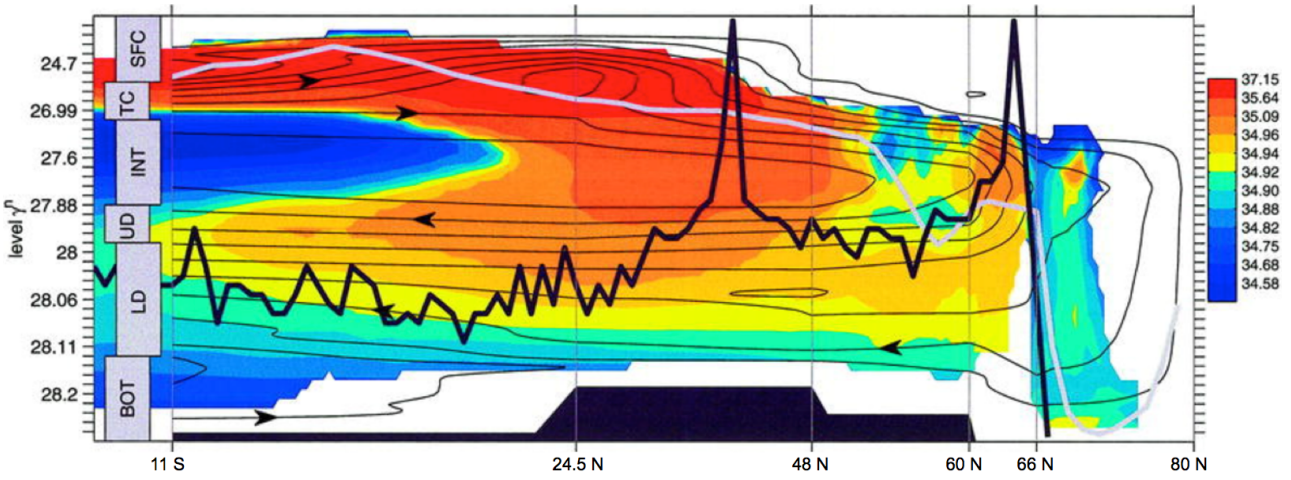

Figure. 1.1 | Meridional overturning transport in the tropical and North Atlantic, superimposed on zonally-averaged climatological salinity. SFC is the abbreviation for surface layer, TS for thermocline layer, INT for intermediate layer, UD for upper deep water layer, LD for lower deep water layer, and BOT for bottom layer. Light gray curve marks densest outcropping layer. Dark gray curve marks crest of the Mid-Atlantic Ridge, including the Azores Plateau and Iceland. This figure is adapted from *Lumpkin and Speer* (2003).

example, during International Geophysical Year (IGY) and World Ocean Circulation Experiment (WOCE), primarily at 34° S, 24° S, 11° S, 24.5° N, 36° N, and 48° N (*Bryden and Hall*, 1980; *Roemmich and Wunsch*, 1985; *Sloyan and Rintoul*, 2001; *Talley*, 2003; *Lumpkin and Speer*, 2003, 2007; *Bryden et al.*, 2011; *Garzoli and Baringer*, 2007). The focus of these studies is on the mean intensity of the AMOC, as well as the associated heat and freshwater transports. In the calculations, the Ekman components are computed from wind stress data, while the geostrophic components are derived from hydgrographic data. Since only the vertical shear of the geostrophic velocity can be determined from the density field, a method must be applied to infer the reference geostrophic velocity, so that the absolute geostrophic transport can be determined. Many studies apply the box inverse method, which has been shown to be an effective tool to estimate the circulation (*Wunsch*, 1978; *Roemmich and Wunsch*, 1985; *Klein et al.*, 1995; *Lumpkin and Speer*, 2003; *Lux et al.*, 2001; *Sloyan and Rintoul*, 2001; *Ganachaud and Wunsch*, 2000; *Ganachaud*, 2003; *Lumpkin and Speer*, 2007). The box inverse method will be briefly introduced later in this section; for a detailed description of the method, please refer to Sect. 3.3.

One of the most comprehensive estimates of the Atlantic meridional circulation is presented in the global inverse study by *Ganachaud and Wunsch* (2000) using WOCE sections. They

combined hydgrographic data with boundary current transports and Ekman transports derived from satellite-based wind measurements to carry out the calculation. The inverse solution shows that the strength of the AMOC is about 14 to 16 Sv with 2 Sv uncertainty throughout the Atlantic basin. *Lumpkin and Speer* (2003, 2007) further included air-sea flux estimates and allowed the air-sea flux induced water mass transformation in their version of box inverse model. They subsequently performed inverse studies both in the North Atlantic and globally with a larger number of sections and found that the strength of the AMOC ranges between 16.2 and 18.0 Sv in the North Atlantic, consistent with the estimates of *Ganachaud and Wunsch* (2000) (Fig. 1.1). The inverse solutions also indicate that the meridional heat transport associated with the AMOC peaks at about 24° N with about 1.2-1.3 PW.

Efforts have also been made to detect changes of the AMOC using repeated hydrographic sections. *Bryden et al.* (2005a) proposed that the AMOC was slowing down since the 1950s by comparing repeated hydrographic section data at 24.5° N measured in 1957, 1981, 1992, 1998, and 2004. However, following-up studies show that the proposed weakening was merely due to the unresolved seasonal cycle of the AMOC (e.g. *Kanzow et al.* 2010; *Atkinson et al.* 2012). *Hernández-Guerra et al.* (2010) examined Argo profiles and drift velocities at 24.5° N and 32° N between 2003 and 2007 by using the box inverse method, and concluded that it is unlikely that the AMOC has significantly changed since the 1950s through comparison with previous estimates. However, the inverse study by *Hernández-Guerra et al.* (2014) shows that the AMOC at 24.5° N and 7.5° N was significantly weaker in the 2010s then the 1990s. On the other hand, by analysing repeated sections at 48° N using the box inverse method, *Lumpkin et al.* (2008) found no significant change in the AMOC throughout the 1990s. Moreover, *Willis* (2010) combined the drift velocities and profiles of the Argo floats with satellite altimeter data and derived a time series (2002-2009) of the upper limb of the AMOC (upper 2000 m) at 41° N. He estimated a mean AMOC strength of 15.5 ± 2.4 Sv and found no significant trend in the AMOC. However, the method employed by *Willis* (2010) is limited to regions where continental slopes are steep, since the boundary currents cannot be accurately calculated in regions with water depth less than 2000 m due to the poor coverage with Argo measurements in those regions.

1.2.2.2 Box inverse method

Based on the thermal wind relation, the vertical shear of the geostrophic velocity relative to an arbitrary reference depth can be calculated from the density field between adjacent CTD

stations. However, to obtain the absolute geostrophic velocity, a reference velocity must be assigned to the shear at the reference level. A classical method of estimating the reference velocity, thus describing the ocean circulation, is the box inverse method, initiated by *Wunsch* (1977). A box inverse model requires an enclosed "box" in the ocean bounded by hydrographic sections and land masses. The "box" is vertically divided into layers by density surfaces according to water mass characteristics. By employing the thermal wind relation, conservation equations of properties (i.e. volume, salt, heat) in the whole box and layers can be formulated. A box inverse model is generally an underdetermined system of equations. In order to obtain physically reasonable solutions, the box inverse model must be properly weighted. The weighting is done by using the estimated uncertainty of the reference velocity and transport elements, as well as the variability of the properties within the layers and the whole box. The weighted system can be solved using Singular Value Decomposition (SVD) with a proper rank that allows the solution to satisfy the conservation, and at the same time to represent a realistic circulation (*Wunsch*, 1996). The uncertainty of the inverse solution can be estimated using a Gaussian-Markov estimator (*Wunsch*, 1996; *Tsubouchi et al.*, 2012; *Hernández-Guerra et al.*, 2014).

A powerful aspect of the box inverse method is that it allows to integrate additional information into the system as constraints, which are based on known circulation features, for instance, the Florida Current and the Bering Strait transport. However, the box inverse method also has drawbacks. The main critics are on the non-synoptic hydrographic sections used to build the box, which are normally completed in one or two months, and usually occupied in different seasons or years. This is a question that any large scale ocean inverse study must encounter, since it is practically impossible to find several hydrographic surveys conducted simultaneously and instantly. However, it is reasonable to assume that provided a time-averaged initial condition and constraints (i.e. using time-mean values of the Ekman transport and other circulation components as constraints), the inverse solution could represent a time-averaged circulation; and the hydrographic variation should be absorbed in the model error or cancelled by the correction to the initial reference velocity (*Ganachaud and Wunsch*, 2000; *Ganachaud*, 2003; *Lumpkin and Speer*, 2003).

In this thesis, the realizations of the 14.5° N and 24.5° N sections are used to build two "boxes", namely the 1989/1992 box and 2013/2015 box. By applying the box inverse method, full-depth meridional overturning transport and horizontal circulations for the two different periods are determined. The inverse solutions allow us to examine changes of circulation over

the past two decades. Moreover, by using different initial conditions in the box inverse model, the sensitivity of the inverse solution to Ekman transport, reference velocity, and hydrographic variability can be examined, which is essential for interpreting the inverse solutions.

1.2.3 Array-based AMOC observations

The first basin-wide array-based observing system to monitor the AMOC is the Rapid Climate Change/Meridional Overturning Circulation and Heat Flux Array (RAPID) at 26.5° N starting from April 2004. It is designed to provide a continuous estimate of the AMOC strength. It consists primarily of three components: (1) the Gulf Stream transport through the Florida Straits, which is estimated from submerged telephone cable voltage data; (2) the meridional Ekman transport estimated from wind stress data; and (3) the mid-ocean geostrophic transport measured by the end-point geostrophic moorings at the western and eastern boundaries and at both sides of the Mid-Atlantic Ridge (MAR). Using the first four years of data, *Kanzow et al.* (2010) estimated a mean AMOC strength of 18.7±4.8 Sv (mean ± rms) at 26.5° N. When using the RAPID AMOC time series to date, the mean AMOC strength is slightly weaker compared to that of the first four years of data and amounts to 16.9 ± 4.4 Sv.

Studies based on the RAPID array data have shown that the AMOC exhibits variability on time scales from seasonal to decadal (*Cunningham et al.*, 2007; *Kanzow et al.*, 2010; *Smeed et al.*, 2014; *Frajka-Williams et al.*, 2016), with different contributors to the AMOC variability dominating on different time scales. *Cunningham et al.* (2007) reported that on subseasonal time scales, the variability in the Ekman transport dominates the variability in the AMOC. *Kanzow et al.* (2010) showed that the seasonal cycle of the AMOC is mainly driven by the seasonality of the upper mid-ocean geostrophic transport (upper 1100 m excluding the Florida Straits), whose strength is set by the seasonal variability of the wind stress curl near the eastern boundary, while the Ekman transport plays a minor role on seasonal time scales. However, using ten-year records of the RAPID, *Frajka-Williams et al.* (2016) showed that on seasonal time scales the upper mid-ocean geostrophic transport is balanced by the Florida current transport, and therefore has only little net effect on the seasonal AMOC variability. In fact, it is the Ekman transport variability and the baroclinic response of the deep ocean to the Ekman transport contributing to the AMOC variability on seasonal time scales. A weak AMOC event is captured by the RAPID array between 2009 and 2010. *McCarthy et al.* (2012) showed that an anomalously strong southward upper mid-ocean geostrophic transport and a weaker than average Ekman transport are responsible for the weaker AMOC during this period. *Smeed*

et al. (2014) showed a decline of the AMOC between 2004 and 2012, and further illustrated that on interannual and longer time scales, the upper mid-ocean geostrophic transport plays the dominant role in modulating the strength of the AMOC. The updated time series indicate that the AMOC is recovering since 2012, yet it is still too early to tell whether the recovery will compensate the earlier decline.

Another major effort to monitor the AMOC is the Meridional Overturning Variability Experiments (MOVE) array at 16° N (*Kanzow et al.*, 2006), which is designed to measure the southward NADW transport (1200-4950 m) in the western basin (west of the MAR). Supported by numerical simulations, the underlying assumption for the configuration of the MOVE array is that the NADW layers in the western basin should capture (nearly) the entire southward returning limb of the AMOC on long time scales, and therefore represent an estimate of the AMOC strength (*Kanzow et al.*, 2008). The first 10-year records (2000-2009) of the MOVE array data shows large interannual variability in the southward NADW transport with 3.8 Sv rms, and a decreasing trend of 3.0 Sv decade^{-1} on 85% confidence interval (*Send et al.*, 2011). Updated estimates based on the MOVE data indicate a strengthening trend of 8.4 ± 5.6 Sv decade^{-1} between Apr 2004 and Oct 2013 (95% confidence interval). This is conflicting with the corresponding RAPID-based trend estimates (-4.1 ± 3.2 Sv decade^{-1}) during the same period (*Baringer et al.*, 2015). Furthermore, *Send et al.* (2011) showed that the interannual variability of the NADW was mainly due to the interannual variability in Labrador Sea Water (LSW) transport (as the primary component of the upper NADW) at 16° N. However, at 26.5° N RAPID-based analysis suggests that the lower NADW transport potentially balances the weaker northward transport in the upper ocean on interannual and longer time scales (*Smeed et al.*, 2014; *Frajka-Williams et al.*, 2016).

As introduced previously, part of the work in this thesis relies on the hydrographic sections at 14.5° N and 24.5° N, which are very close to the MOVE and RAPID arrays, respectively. Therefore, the inverse solution based on the hydrographic data will be compared to the analysis of the MOVE and RAPID data. This, on the one hand, provides validation of the results of the box inverse model, on the other hand helps to interpret changes of the AMOC estimated from the inverse method. The horizontal circulation patterns determined from the 14.5° N section may also provide information on the circulation over the MAR and in the eastern basin, which the MOVE array does not cover.

1.2.4 Model-based AMOC estimates

In general, model simulations forced by atmospheric reanalyses tend to return a large spread of AMOC, which highly depend on details of the model configurations, such as model resolution, and parametrizations of eddy fluxes and overflows (*Buckley and Marshall*, 2016). For instance, the mean strength of the AMOC in CMIP5 models ranges from 13 to 33 Sv, with the model-dependent maximum of the AMOC located between 20° N and 60° N (*Wang and Zhang*, 2013). Ocean state estimates that assimilate observational data potentially improve the agreement between the models and observations, but the strength of the AMOC and the associated heat transport still differ between state estimates and do not fully agree with observations. For instance, assimilations of the Estimating the Circulation and Climate of the Ocean (ECCO) (*Wunsch and Heimbach*, 2013) and the Geophysical Fluid Dynamics Laboratory (GFDL) (*Chang et al.*, 2013) underestimate the strength of the AMOC at 26.5° N in comparison to the estimate from the RAPID array data. An updated version of German ECCO state estimate (GECCO2) (*Köhl*, 2015), which is based on the ECCO model, shows improved consistency with the observations. For instance at 26.5° N the annual mean overturning stream function derived from the GECCO2 is in good agreement with the one derived from the RAPID data in the upper 2500 m.

Model simulations also suggest that the AMOC varies on time scales from subseasonal to multidecadal (e.g. *Jayne and Marotzke* 2001; *Biastoch et al.* 2008; *Wunsch and Heimbach* 2009; *Wang and Zhang* 2013). On short time scales (subseasonal to intra-annual), the magnitude of the AMOC variability is of the same order as the mean strength, while on interannual to decadal time scales the AMOC varies only by a few Sverdrups (*Buckley and Marshall*, 2016). The seasonal variability of the AMOC at low and mid-latitudes is dominated by the seasonal cycle of the wind-driven Ekman transport (e.g. *Jayne and Marotzke* 2001; *Wunsch and Heimbach* 2009), while the multidecadal variability is believed to be related to the Atlantic Multidecadal Oscillation (AMO) that manifests in the sea surface temperature (SST) change in the North Atlantic (e.g. *Latif et al.* 2004; *Wang and Zhang* 2013). Studies have demonstrated the ocean models' ability to reproduce large parts (70-80%) of the strong AMOC variability on short time scales as observed by the RAPID array (e.g. *Roberts et al.* 2013), if the models are forced by the observed wind even without data assimilation. This can be largely explained by the wind-driven Ekman transport variability and anomalies of the upper ocean geostrophic transport which are associated with isopycnal displacements induced by the wind. This result

further emphasizes the importance of the Ekman transport to the AMOC.

Climate model-based studies predicting the future of the AMOC suggest that the AMOC is likely to weaken under a continuously warming climate, and might result in a total breakdown in the next centuries (*Rahmstorf et al.*, 2005, 2015; *Böning et al.*, 2016). They attributed the weakening to the accumulated freshening in the deep water formation region. The fifth IPCC assessment report also suggest that over the 21st century the AMOC is very likely to weaken (*Collins et al.*, 2013), although observations have not shown solid evidence supporting the weakening.

In this thesis, the GECCO2 ocean state estimate will be compared with the inverse solution, and the MOVE and RAPID array data, as it has been shown to represent well the observed AMOC strength and variability at 26.5° N. Additionally, the hydrographic data used in this thesis date back to the late 1980s, with no other observational data available to validate the estimations by the inverse method. Instead, the GECCO2 can serve as a reference for the inverse solution, and allow inspection to the long-term changes of the AMOC at 14.5° N and 24.5° N.

1.3 Ekman transport

As the primary ageostrophic component of the AMOC, the meridional Ekman volume transport plays an important role in the AMOC. According to the classical linear theory of *Ekman* (1905), under the momentum balance between steady wind stress and Coriolis force, the wind-driven flow spirals clockwise with depth, forming the Ekman spiral. Vertically integrating the spiral results in a net volume transport to the right of the wind direction (northern hemisphere), the Ekman transport. The contribution of the Ekman transport to the AMOC differs with latitudes. For instance, in the tropical Atlantic strong and relatively steady trade winds generate a poleward Ekman transport amounting to about 8 to 13 Sv (*Chereskin and Roemmich*, 1991; *Garzoli and Molinari*, 2001), while in the subtropics (e.g. at 24.5° N) the meridional Ekman transport is only about 3.6 ± 1.9 Sv (*Atkinson et al.*, 2010). RAPID-based analyses show that temporal variations in the meridional Ekman transport cause barotropic adjustment in the ocean interior, which affect the intensity of the AMOC on subseasonal and seasonal time scales (*Cunningham et al.*, 2007; *Kanzow et al.*, 2010; *McCarthy et al.*, 2012). Model-based studies also indicate that the seasonal and intra-annual variability of the AMOC is largely explainable by the Ekman transport directly driven by the wind, and the wind-induced geostrophic anomalies

(*Roberts et al.*, 2013). The temperature and salt transports associated with the Ekman volume transport provide an important upper-layer constraint, for example, for estimating net heat and freshwater transports across a section using hydrographic data or geostrophic end point array data (*McCarthy et al.*, 2015; *McDonagh et al.*, 2015).

In general, Ekman transport can be estimated from wind stress data or from directly measured velocity data. The wind-stress-based method is commonly applied, since wind stress data are generally available through observations on different platforms (e.g. ships and satellites). For instance, the RAPID-based AMOC estimation initially used Quickscat wind measurements to infer the meridional Ekman transport (currently using the European Centre for Medium-Range Weather Forecasts (ECMWF) Interim Re-Analysis winds; *McCarthy et al.* 2015). The velocity-based method requires the calculation of an ageostrophic velocity that relies on both direct velocity and hydrographic data, which are rarely available. Only a few studies estimated the basin-scale meridional Ekman transport using both methods and found that the estimates of the two methods agreed with each other within 10 to 20% (*Chereskin and Roemmich*, 1991; *Wijffels et al.*, 1994; *Chereskin et al.*, 1997). However, both methods suffer different kinds of errors. For the wind-stress-based calculation, temporally varying wind fields, as well as momentum fluxes calculated from different bulk formulas introduce the largest uncertainty; for the velocity-based method, unknown Ekman depth, and non-Ekman ageostrophic components (e.g. near inertial internal waves) complicate the calculations.

To estimate the Ekman heat and salt transports, the Ekman volume transport must be combined with an Ekman layer temperature and salinity, respectively. Of particular interest is whether SST is a sufficient constraint for the Ekman layer temperature. Previous studies (e.g. *Wijffels et al.* 1994; *Friedrichs and Hall* 1993) show that the heat flux is primarily determined by the transport and less by the relatively small variability in temperature. However, the unresolved vertical structure of the upper-ocean temperature profile could cause an unknown bias in the Ekman heat transport estimation. An extreme case has been reported for the Indian Ocean at 8° N at the end of a summer monsoon event (*Chereskin et al.*, 2002), where the Ekman layer temperature was 1.1 °C cooler than the averaged SST. This resulted in a 5% smaller Ekman heat transport when using the temperature profile data in the Ekman layer instead of SST.

Given the strong trade winds and warmer upper-layer temperature in the tropical region, the meridional Ekman volume and heat transport is expected to play a bigger role in the AMOC and the associated total heat transport there compared to other regions. In this thesis,

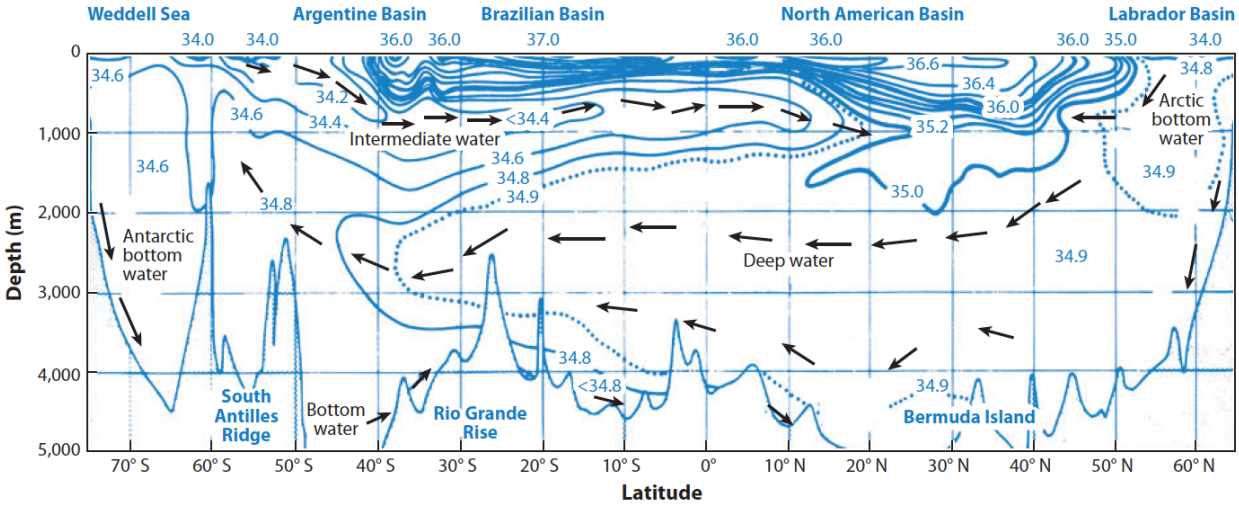

Figure. 1.2 | Meridional section of salinity in the western Atlantic. This figure is adapted from *Lozier* (2012), where it is a reprint from *Merz* (1925).

direct velocity observations are available for the 11° S section and the 2013 realization of the 14.5° N section. Together with the satellite-based and reanalysis wind stress data, they provide a unique opportunity to investigate the structure of the ageostrophic flow, and to estimate the meridional Ekman volume, heat, and salt transport using different methods and different datasets. This provides references for the full-depth AMOC study in this region. In turn, the sensitivity experiments using the box inverse model will reveal the importance of Ekman transport to the AMOC and the associated heat transport.

1.4 Water masses in the tropical Atlantic

Already in the preparation for the Meteor expedition during 1925-1927, *Merz* (1925) collected the best data available, and produced a schematic showing the meridional distribution of waters in the Atlantic (Fig. 1.2). A layer of water is indicated centred at about 800 m with a salinity minimum originating from the Antarctic and stretching to the subtropical North Atlantic. Also shown is a layer of high salinity water residing between 1500 and 4000 m originating from the subpolar North Atlantic and approaching the Antarctic continent, where it is upwelled to the upper layer. Today, it is widely accepted that the water mass distribution shown by *Merz* (1925) is closely related to the AMOC.

Since the region of interest in this thesis is the tropical Atlantic, water mass distribution and characteristics in this region will be briefly introduced. In general, water masses can be identified through their potential temperature (θ) and salinity (S) relation. In the following,

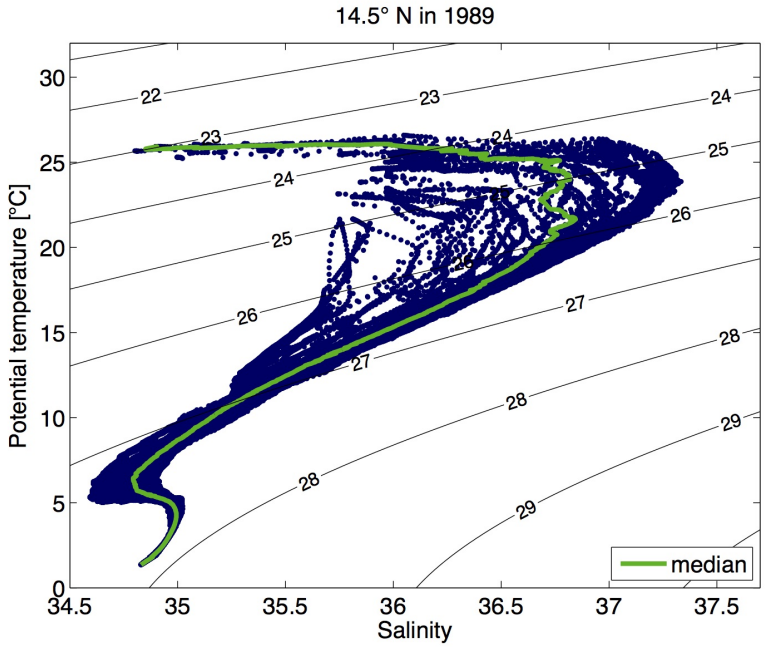

Figure. 1.3 | θ/S diagram using all the measurements (dark blue dots) from a zonal trans-Atlantic section along 14.5° N in 1989. The green curve is the median θ/S profile derived on neutral density surfaces.

the θ/S relation of the 1989 realization at 14.5° N is used as an example (Fig. 1.3).

Proceeding from the surface water of highest temperature downwards, the salinity maximum at about 24 °C marks the Subtropical Underwater (STUW), originating from the subtropical Atlantic due to excessive evaporation. The median θ/S diagram calculated on the neutral density surfaces shows two maxima between 25 and 22 °C, indicating that at 14.5° N this water mass consists of a mixture of STUW from the North (more saline) and South (less saline) Atlantic. Directly below the salinity maxima, a nearly linear θ/S relation over the θ range of 8-20 °C marks the Central Water (CW). CWs are formed by subduction within the subtropical gyre due to Ekman pumping, and subsequently move equatorward as a result of the Sverdrup balance (*Talley et al.*, 2011). At this latitude, CWs occupy the thermocline with a majority originating from the North Atlantic (referred to as NACW), and a small portion of the less saline South Atlantic Central Water (SACW), found in the θ range of 13 to 18 °C and near the eastern boundary. After crossing the equator, SACW is transported to the east within the zonal jets of the equatorial current system. When approaching the West African coast, it spreads further northward from where it diffuses into the eastern tropical North Atlantic (*Kirchner et al.*, 2009; *Brandt et al.*, 2015).

In the intermediate layer, Antarctic Intermediate Water (AAIW) is characterized by its

distinct salinity minimum signature. This water mass originates from the South Atlantic sector of the Antarctic Circumpolar Current (ACC), and is transported northward mainly along the western boundary (*Tsuchiya*, 1989). Due to mixing with surrounding waters on its way northward, AAIW gradually loses the salinity minimum signature, which can be tracked to about 20° N (Fig. 1.1 and 1.2). Another water mass in the intermediate layer is the Mediterranean Water (MW), characterized by its salinity maximum at mid-depth (1000-2000 m). MW enters the Atlantic through the Strait of Gibraltar from the Mediterranean Sea. Its high salinity is a result of strong evaporation and water mass formation in the Mediterranean Sea (*Talley et al.*, 2011).

The southward returning limb of the AMOC consists primarily of NADW. NADW can be divided into upper and lower NADW (referred to as UNADW and LNADW, respectively), according to their formation regions and the corresponding density ranges. UNADW is composed primarily of the LSW (*Talley and McCartney*, 1982), while LNADW consists of the overflow waters from the Nordic Sea (*Pickart*, 1992; *Smethie et al.*, 2000), namely Iceland Scotland Overflow Water (ISOW) and Denmark Strait Overflow Water (DSOW). These water masses spread southward within the DWBC and interior pathways. In the tropical North Atlantic, the LSW and DSOW at the western boundary are characterized by their higher oxygen concentrations (> 260 μmol kg^{-1}) than the neighbouring waters, and vertical separated by the ISOW with relatively lower oxygen concentration (**?**).

AABW, as the densest water in the World Oceans, is found in the tropical Atlantic primarily in the abyssal basin west of the MAR with neutral density larger than 28.125 kg m^{-3} and θ lower than 1.8 °C. The MAR, as a topographic barrier, prevents AABW flowing directly into the eastern North Atlantic basin, except at the Romanche Fracture Zone near the Equator and the Vema Fracture Zone at 11° N (*Wüst*, 1935; *McCartney et al.*, 1991). *Klein et al.* (1995) reported that the lowest salinity and temperature in the abyssal eastern basin found at 14.5° N was lower than that found at either 16° N and 8° N, indicating the existence of a pathway for the AABW across the MAR between 8° N and 14.5° N.

Observations show that both AAIW and AABW undergo property changes in the tropical Atlantic. For the AAIW, *Sarafanov et al.* (2008) showed that the AAIW at 6.5° N has become significantly warmer through comparison of hydragraphic data measured in 1957, 1993, and 2000. *Schmidtko and Johnson* (2012) reported an overall warming and shoaling of the AAIW core, and a warming and salinification trend in the tropical North Atlantic since the mid-1970s. For the AABW, *Johnson et al.* (2008) reported that the AABW in the subtropical North

Atlantic has become warmer between the 1980s and 2000s; and *Herrford et al.* (2017) showed that the temperature of the coldest AABW in the equatorial Atlantic increased since the 1990s. Additionally, freshening of the NADW in the formation region since several decades has been observed (*Dickson et al.*, 2002). The freshening signal has been shown to have crossed the equator and reaching the South Atlantic (e.g. *Hummels et al.* 2015).

The causes for the water mass property changes are still under investigation. Potential reasons include changes in the source water masses in the formation regions. *Arbic and Owens* (2001) and *Schmidtko and Johnson* (2012) suggested that the observed warming of the AAIW away from the formation region was a consequence of the atmospheric warming in the source region. The freshening of the NADW is attributed to the continuously increasing freshwater input in the subpolar North Atlantic in response to anthropogenic warming (*Dickson et al.*, 2002). Other aspects are changes in the circulation, which might either slowdown or accelerate the ventilation of the associated water masses, consequently extending or shortening mixing periods with surrounding waters. For instance, *Johnson et al.* (2008) attributed a warming of the AABW in the subtropical North Atlantic to a reduction in the transport of the bottom cell of the AMOC.

In this thesis, recently obtained full-depth temperature and salinity data along 14.5° N and 24.5° N are available (in 2013 and 2015, respectively). This allows a comparison with those data collected along the same sections about two decades ago (in 1989 and 1992, respectively), and potentially provides insights into water mass property changes over the past two decades. The hydrographic data also enable an estimation of the circulation at the two latitudes in the different periods, which allows examination of a potential connection between changes in the water masses and changes in the circulation patterns.

1.5 Scientific questions of this thesis

In light of the backgrounds above, this thesis focuses mainly on three aspects of the AMOC in the tropical Atlantic: the first one is on the meridional ageostrophic transport (Chapter 2). In this part, hydrographic data, directly measured velocity data, in-situ and satellite-based wind stress data, and GECCO2 ocean state estimate along trans-Atlantic sections at 11° S and 14.5° N (2013) are used. The following questions will be answered:

- What is the vertical structure of meridional ageostrophic flow? What are the Ekman transports across 11° S and 14.5° N and how deep does the Ekman flow penetrate?

The second aspect regards the water mass property changes (Chapter 3.2). Through comparison of potential temperature, salinity, dissolved oxygen, and neutral density data along 14.5° N between 1989 and 2013, and along 24.5° N between 1992 and 2015, the following question will be answered:

- How have water mass properties in the tropical Atlantic changed over the past two decades?

The last aspect is on the strength of the AMOC (Chapter 3.3 to 3.5). By applying a box inverse model to the hydrographic sections at 14.5° N, and 24.5° N, two "boxes" (1989/1992 box and 2013/2015 box) are designed. The absolute geostrophic transports across the sections are determined. Furthermore, the sensitivity of the inverse solution to the Ekman transport is tested. Through comparison between the inverse solution, the GECCO2 ocean state estimate, and the MOVE and RAPID array analysis data, the following questions will be answered:

- Are there circulation changes corresponding to the changes in the water mass properties? Has the AMOC at 14.5° N and 24.5° N weakened between 1989/1992 and 2013/2015, and how to interpret the changes?
- How does the Ekman volume transport affect the overturning structure and the total heat transport of the AMOC?

2 On the meridional ageostrophic transport in the tropical Atlantic

The meridional Ekman volume, heat, and salt transport across two trans-Atlantic sections near 14.5° N and 11° S were estimated using in-situ observations, wind products, and assimilation data. By using different datasets and different methods, the vertical structure of the ageostrophic flow was presented, the penetration depth of the Ekman flow was determined, the uncertainties of the Ekman transport estimation were documented. The results of this study gives insights into the meridional Ekman fluxes in the tropical Atlantic, and provides reference for studies on the Atlantic meridional overturning circulation.

The manuscript was published in Ocean Science in July 2017.

Citation: **Fu, Y., Karstensen, J. and Brandt, P.: On the meridional ageostrophic transport in the tropical Atlantic, Ocean Sci., 13(4), 531-549, doi:10.5194/os-13-531-2017, 2017.**

The candidate designed the study and analysed the ship-board, satellite-based, and assimilated data. He performed calibration and quality control of the underway CTD data. He produced all figures and authored the manuscript from the first draft to the final version.

Abstract

The meridional Ekman volume, heat and salt transport across two trans-Atlantic sections near 14.5° N and 11° S were estimated using in-situ observations, wind products and model data. A meridional ageostrophic velocity was obtained as the difference between the directly measured total velocity and the geostrophic velocity derived from observations. Interpreting the section mean ageostrophy to be the result of an Ekman balance, the meridional Ekman transport of 6.2 ± 2.3 Sv northward at 14.5° N and 11.7 ± 2.1 Sv southward at 11° S is estimated. The integration uses the top of the pycnocline as an approximation for the Ekman depth, which is on average about 20 m deeper than the mixed layer depth. The Ekman transport estimated based on the velocity observations agrees well with the predictions from in-situ wind stress data of 6.7 ± 3.5 Sv at 14.5° N and 13.6 ± 3.3 Sv at 11° S. The meridional Ekman heat and salt fluxes calculated from sea surface temperature and salinity data or from high-resolution temperature and salinity profile data differ only marginally. The errors in the Ekman heat and salt flux calculation were dominated by the uncertainty of the Ekman volume transport estimates.

2.1 Introduction

In the tropical Atlantic Ocean, strong and steady easterly trade winds generate a poleward meridional flow in the surface layer. According to the classical linear theory of *Ekman* (1905), under the momentum balance between steady wind stress and Coriolis force, the wind-driven flow spirals clockwise with depth, the Ekman spiral, while the vertical integration of the spiral results in a net volume transport to the right of the wind direction (Northern Hemisphere), the Ekman transport. A convergence is created in the subtropics, where the poleward Ekman transport induced by the trade winds interacts with the equatorward Ekman transport induced by the mid-latitude westerlies. In simple linear vorticity theory, the Ekman convergence in subtropics drives an equatorward Sverdrup transport that explains many aspects of the wind-driven gyre circulation, such as the Subtropical Cell (STC). *Schott et al.* (2004) calculated the Ekman divergence (21-24 Sv, 1 Sv=10^6 m^3 s^{-1}) between 10° N and 10° S in the tropical Atlantic using climatological wind to infer the strength of the STC; *Rabe et al.* (2008) further analysed the variability of the STC using the same sections based on assimilation products, and found that on timescales longer than 5 years to decadal, the variability of poleward Ekman divergence leads the variability of geostrophic convergence in the thermocline.

The meridional Ekman transport is, depending on the latitude, an important upper layer

contribution when estimating the strength of the Meridional Overturning Circulation (MOC *Friedrichs and Hall* 1993; *Klein et al.* 1995; *Wijffels et al.* 1996). The variations in the meridional Ekman transport have been found to cause barotropic adjustment of the MOC in the ocean interior on different timescales. *Cunningham et al.* (2007) reported that the upper ocean had an immediate response to the changes in Ekman transport at subseasonal to seasonal timescales, while *Kanzow et al.* (2010) found that on the seasonal timescale, the Ekman transport was less important than the mid-ocean geostrophic transport, whose seasonal variation was dominated by the seasonal cycle of the wind stress curl. *McCarthy et al.* (2012) analysed a low MOC case during 2009 and 2010, and also pointed out that on interannual timescales, although the Ekman transport played a role, its variability was relatively small compared to the variability in mid-ocean geostrophic transport, especially in the upper 1100 m.

Of interest for large-scale overturning studies are also the meridional Ekman-driven heat and freshwater fluxes that provide an important upper layer constraint, for example, for geostrophic end point arrays (*McCarthy et al.*, 2015; *McDonagh et al.*, 2015). In many cases, SST has been found to be a sufficient constraint for the Ekman layer temperature (*Wijffels et al.*, 1994; *Chereskin et al.*, 2002). This probably is not too much of a surprise as the heat flux is primarily determined by the transport and less by the relatively small variability in temperature. However, the unresolved vertical structure of the water column could lead to an unknown bias, for example, due to the difference between the mixed layer (MLD) and the depth of the Ekman layer. An extreme case has been reported for the northern Indian Ocean at 8° N at the end of a summer monsoon event (*Chereskin et al.*, 2002), where the direct Ekman temperature transport was 5% smaller when using the temperature within the top of the pycnocline (TTP) (as a proxy of the Ekman layer depth) than using the SST, and the corresponding mean temperature in the Ekman layer was 1.1 °C cooler than the averaged SST. In this case, the mean TTP depth was 92 m deeper than the mean MLD.

Assuming the upper layer ageostrophic flow in Ekman balance, the meridional Ekman transport (M_E^y) can be estimated indirectly from zonal wind stress data or directly from integrating observed ageostrophic Ekman velocity (v_E):

$$M_E^y = \frac{1}{\rho}\frac{\tau_x}{f} = \int_{-D_E}^{0} v_E dz, \tag{2.1}$$

where x is the zonal wind stress, ρ is the density of seawater, f is the Coriolis parameter of the respective latitude, D_E is the Ekman depth, and z is the upward vertical coordinate. D_E can be defined as the e-folding-scale depth of the Ekman spiral, leading to an analytical solution

of $D_E = \sqrt{\frac{2A_v}{f}}$, where A_v is a constant vertical eddy viscosity (*Price et al.*, 1987). Ekmans solution also reveals a surface Ekman velocity $V_0 = \frac{\tau}{\sqrt{\rho^2 f A_v}}$, which is 45° to the right (left) of the wind direction in the Northern (Southern) Hemisphere.

An ageostrophic velocity (v_{ageos}) can be calculated as the difference of the directly observed velocity (v_{obs}) and the geostrophic velocity (v_{geos}). The ageostrophic velocity might consist of an Ekman component (v_E) and components that are not in Ekman balance (e.g. inertial currents). Often the non-Ekman components are assumed to be 0, and v_E is expected to equal v_{ageos}. Under this assumption, the Ekman velocity can be derived as follows:

$$v_E = v_{obs} - v_{geos}. \tag{2.2}$$

Direct velocity profile data, for example from Acoustic Doppler Current Profiler (ADCP), and geostrophic velocities, from hydrographic data, are used in studies comparing direct with indirect Ekman transport estimates (e.g. *Chereskin and Roemmich* 1991; *Wijffels et al.* 1994; *Garzoli and Molinari* 2001). The Ekman transport is then derived from vertical integration of the v_E.

For both equations it is relevant to recall that the Ekman balance is derived for an ocean with constant vertical viscosity and infinite depth, forced by a steady wind field (*Ekman*, 1905). Such conditions are not found in the real ocean; therefore, applications of the indirect (Eq. 2.1) and direct (Eq. 2.2) approaches suffer from different kinds of errors. For the indirect approach (Eq. 1) the temporally varying wind field, the momentum flux calculated from the wind speed, and the unknown partitioning of the wind energy input into the Ekman layer at different frequency bands are probably the most important sources of errors introduced into any Ekman current/transport estimate. For the direct approach, unknown lower integration depth, momentum flux variability, errors introduced by the experimental design (e.g. an shipboard ADCP does not resolve the upper 10-20 m of the flow, which is often assumed equal to the values at the first valid bin) or instrument errors can impact obtained results.

Many observational studies on Ekman dynamics that compare indirect and direct approaches have been conducted in the trade wind regions, where at least the wind stress forcing is relatively constant. Using shipboard ADCP data together with Conductivity-Temperature-Depth (CTD) profile data, *Chereskin and Roemmich* (1991) directly estimated an Ekman transport of 9.3 ± 5.5 Sv at 11° N in the Atlantic by integrating an ageostrophic velocity from the surface to a depth equivalent to TTP. The ageostrophic velocity was obtained by subtracting the geostrophic velocity from the ADCP velocity. Using a similar direct method, *Wijffels et al.*

(1994) estimated an ageostrophic transport of 50.8 ± 10 Sv at 10° N in the Pacific. *Chereskin et al.* (1997) found Ekman transports of -17.6 ± 2.4 and -7.9 ± 2.7 Sv during and after a southwest monsoon event at 8.5° N in the Indian Ocean, respectively. In all the above studies, the direct estimates agree within 10-20% of the estimates obtained by using the in-situ wind data (Eq. 2.1). Both the direct and indirect approaches also show a consistent transport structure across all the basins, which can be seen from the cumulative meridional Ekman transport curves from one boundary to the other. An indication of the existence of an Ekman balance in the upper ocean is the occurrence of an Ekman spiral. In all the above publications an "Ekman spiral"-like feature has been identified. Because v_{geos} can be estimated only perpendicularly to the CTD stations and all studies are based on more or less zonal CTD sections, the three-dimensional structure of the Ekman spiral can not be obtained. However, the Ekman flow becomes evident by a near-surface maximum of the meridional ageostrophic velocity decreasing smoothly below within the upper 50-100 m to zero.

Despite the fact that the zonal wind in the above studies was predominantly uniform in one direction, their ageostrophic velocity showed a pattern of alternating currents. Also, the section-averaged ageostrophic velocity profiles often exhibited structures that are not a result of an Ekman balance. *Chereskin and Roemmich* (1991) reported signals of internal wave propagation that was responsible for a peak in their section-integrated ageostrophic transport profile below the Ekman layer. *Garzoli and Molinari* (2001) also reported on vertically alternating structures in the section-averaged ageostrophic velocity profile at 6° N in the Atlantic. They proposed several possible candidates that could contribute to creating this structure, such as inertial currents within the latitude range of the North Equatorial Counter Current (NECC), and tropical instability waves with northward and southward velocities. Besides, they argued that the advective terms in the momentum equations might also produce a large non-Ekman ageostrophic transport in the presence of large horizontal shears between the NECC and the northern branch of the South Equatorial Current (nSEC).

The appearance of these non-Ekman ageostrophic currents is not surprising, since it has been long recognized that the temporal variability of the wind field leads to wind energy input into the Ekman layer at subinertial and near-inertial frequencies. *Wang and Huang* (2004) estimated the global wind energy input into the Ekman layer at subinertial frequencies (frequency lower than 0.5 cycles per day) to be 2.4 TW, while *Watanabe and Hibiya* (2002) and *Alford* (2003) estimated that at near-inertial frequencies the wind energy input was 0.7 and 0.5 TW, respectively. *Elipot and Gille* (2009) estimated the wind energy input into the Ekman layer for

the frequency range between 0 and 2 cpd at 41° S in the Southern Ocean using surface drifter data. They found that the near-inertial input (between 0.5 f and 2 cpd) contributes 8% of the total wind energy input (here the "total" means the frequency range between 0 and 2 cpd), which may still underestimate the near-inertial contribution due to limitations in their data. All these studies suggest that at least about 10% of the wind energy (frequency range between 0 and 2 cpd) into the Ekman layer is at near-inertial frequencies, which is used to supply the non-Ekman ageostrophic motions (inertial oscillation, near-inertial internal waves, etc.). Therefore, complicated structures in the directly observed ageostrophic velocity as reported by *Chereskin and Roemmich* (1991) and *Garzoli and Molinari* (2001) can be anticipated.

The purpose of the present study is to estimate the Ekman volume, heat, and freshwater transport across two trans-Atlantic sections nominally along 14.5° N and 11° S by using direct and indirect methods, and to analyse the vertical structure of the ageostrophic flow by using high-resolution velocity and hydrographic data. In previous studies, the geostrophic velocity was estimated using CTD profile data with a station spacing of approximately 30-60 nm, and only in-situ and climatological wind data were available. In this study, we apply the recently introduced underway CTD (uCTD), which allows profiling with denser station spacing of about 8-10 nm or less and does not require additional station time by measuring from moving ships (e.g. volunteer commercial and research vessels). We first describe the processing of the uCTD data in detail, and then apply the uCTD data to calculate the Ekman transport. We also test the sensitivity of the Ekman transport estimates with respect to the CTD profile resolution. We then apply wind data from different sources to indirectly estimate the Ekman transport, including the in-situ (ship) wind, satellite-based wind product, and reanalysis wind products. In order to integrate the observation-based Ekman transport estimates into the large-scale tropical Atlantic context, we compared our results with the GECCO2 ocean state estimate. This work is structured as follows: the processing of the data is described in Sect. 2.2. The methods used in the calculation of Ekman volume, heat, and salt transport are described in Sect. 2.3. The vertical and horizontal structures of the ageostrophic velocity, together with the Ekman volume, heat, and salt transport estimated using different datasets and different methods are presented and discussed in Sect. 2.4, followed by a summary in Sect. 2.5.

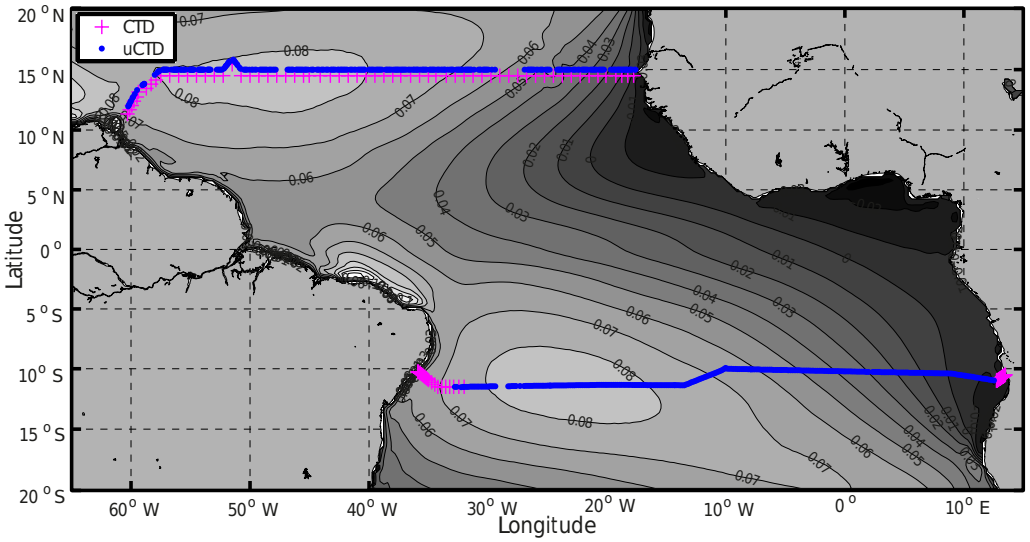

Figure. 2.1 | Positions of the CTD (magenta +) and uCTD (blue dots) measurements along the 14.5° N and 11° S sections. The 14.5° N section was completed during R/V Meteor cruises M96 (28 April to 20 May 2013, west of 20° W) and M97 (8 to 9 June 2013, east of 20° W), the 11° S section during M98 (6 to 23 July 2013). Note that the uCTD position for the 14.5° N section is artificially shifted to the north by 0.5° N for visual clarity. The grey shading with contours is the mean zonal wind stress calculated from NCEP/CFSr monthly wind stress between 1979 and 2011 in N m^{-2}.

2.2 Data

Two trans-Atlantic zonal sections near 14.5° N and 11° S were occupied by R/V Meteor on three cruise legs (M96, M97, and M98). The 14.5° N section began with cruise M96 off the coast of Trinidad and Tobago on 28 April 2013. The section ended on M96 at about 20° W on 20 May, and was continued to the African coast during M97 from 8 to 9 June (Fig. 2.1). During these surveys, 64 CTD stations were conducted along the 14.5° N section, with an average spacing of 40 nm (75 km). Parallel to the CTD system, the uCTD system was operated between the adjacent CTD stations when the ship was steaming at 10-12 kn. In total, 317 uCTD profiles were achieved, with an average spacing of 8 nm (15 km). The 11° S section was surveyed during M98 from 6 to 23 July 2013. In this section, the standard CTD was only operated on the shelf and at the shelf break; during the transit across the Atlantic, only the uCTD was in use. All together, 290 uCTD profiles were taken during the survey, with an average spacing of 11 nm (20 km). Shipboard ADCP and anemometer were in continuous operation through the entire cruises.

2.2.1 CTD and uCTD measurements

The CTD work was carried out with a Sea-Bird Electronic (SBE) 9 plus CTD system. The two temperature sensors were calibrated at the manufacturer just before cruise M96 in March 2013. The conductivity measurements were calibrated by comparing the bottle stop data with salinometer measurements of bottle samples. All CTD system quality control procedures followed the GO-SHIP recommendations (*Hood et al.*, 2010). The accuracy of the CTD data was estimated to be ±0.001 °C for temperature and ±0.002 g kg^{-1} for salinity.

The uCTD system used at both zonal sections was an Oceanscience Series II underway-CTD. It consisted of a probe, a tail, and a winch. The probe is equipped with a temperature (SBE-3F), a conductivity (SBE-4) and a pressure sensor from SBE. A tail spool reloading system allows the rope spooled on the tail to be paid out when the probe falls freely. The sensors record data at a frequency of 16 Hz. For most of the profiles about 250-300 m of rope were spooled on the tail spool (which set the fall depth) and the recording time length was set to 100 s, and about 1600 data recordings per cast were obtained. From the tail spool the probe sinks freely with a nominal speed of 4 m s^{-1}. However, due to the back-and-forth unspooling of the rope from one end of the tail to the other, the sinking speed typically varies from 3 to 4.5 m s^{-1}. After the rope on the tail is paid out completely, the probe still sinks at speeds less than 2 m s^{-1} in the last tens of metres of its sinking before being winched back to the ship and recovered back to deck. Three probes were used during the two section surveys (nos. 70200126 and 70200068 along the 14.5° N section; nos. 70200068 and 70200138 along the 11° S section). The uCTD winches were out of service several times during the three cruise legs. Although they were repaired on-board, several measurement gaps were left, for example, between 29 and 27° W (Fig. 2.1).

The post-calibration of the uCTD data was done in two major steps: the first step is a sensor calibration procedure, which corrects the temperature sensor error due to viscous heating, the conductivity sensor error due to thermal mass delay, and the lag between the conductivity and temperature sensors; the second step is data validation in reference to CTD profile data and to thermosalinograph (TSG) data. The first step was done following *Ullman and Hebert* (2014) (hereafter UH2014). We will briefly describe the process here; for details, please refer to their work. The uCTD is an unpumped CTD system, the rapid sinking speed of 4 m s^{-1} allowing water to pass through the sensor package at 3.56 m s^{-1} (UH2014). This flow rate is much higher than a pumped CTD system (1 m s^{-1}), which leads to a clear viscous heating effect of

the uCTD temperature sensor. This was corrected using a steady-state result of *Larson and Pedersen* (1996) for the perpendicular flow case (cf. Eq. 8 of UH2014). The thermal mass correction was performed following the algorithm of *Lueck and Picklo* (1990) and using the mean values of error magnitude and time constant from UH2014 (cf. Table 1 of UH2014).

From the uCTD profiles alone a time lag correction was determined from cross-correlation of temperature and conductivity sensor small-scale variability. The variability was calculated by subtracting a sixth-order Butterworth low-pass filtered profile with a cut-off frequency of 4 Hz from the corresponding temperature and conductivity time series of each profile. The highest correlation was found for a 1/16 s lag (conductivity leading), which equals the sampling frequency of 16 Hz data. Application of the lag eliminated most of the spikes in the salinity profiles when the sinking speed of the probe was above about 1.5 m s^{-1}. However, when the sinking speed was below 1.5 m s^{-1}, this correction would cause the spikes pointing in the opposite direction and indicates an inverse dependency of the lag on the sinking speed. This result is consistent with that reported by UH2014, and we corrected the lag following their lag model (cf. Eq. 7 of UH2014), but adjusted their parameters to match our data. The data recorded with a sinking speed smaller than 0.3 m s^{-1} were neglected (including all upcast data).

Validation of the lag corrected uCTD against CTD profile data revealed for the 14.5° N section a drift in the conductivity sensors of uCTD probes nos. 70200126 and 70200068. A bias correction in the sense of an absolute salinity offset (uCTD-CTD) was determined based on the temperature-salinity space (*Rudnick and Klinke*, 2007) by considering the conservative temperature range from 12 to 14 °C and using all uCTDs between adjacent CTD pairs. This particular temperature range was chosen because it belongs to the Atlantic central water, whose T/S relation is nearly linear, which implies that in this temperature range, the spreading of salinity measured during different uCTD casts should be tight. Besides, it was also surveyed by almost all uCTD casts along the section. For probe no. 70200126, the salinity offset fluctuates around a mean value of 0.038 g kg^{-1} west of 39° W (CTD station 34), east of which the offset shifts abruptly to around 0.151 g kg^{-1}. The calibration was done by applying the mean offset values to the salinity data in the corresponding groups of uCTDs. The salinity data of the last few profiles of probe no. 70200126 (between 30 and 29° W) were extremely noisy, and not possible to calibrate. This probe was not further used during the rest of the section due to its poor quality of the salinity data. For probe no. 70200068, the salinity offset remains around 0 west of 36° W (CTD station 38), and then abruptly shifts to around 0.295 g kg^{-1} between 36 and 23.5° W (CTD station 56). East of 23.5° W to the African coast, the offset

shows a linear decreasing trend. This is likely due to the increasing portion of SACW in the central water layer when approaching the coastal region, which is less saline than the NACW, and consequently shifting the slope of the T/S curve. As a result, the linear trend of the offset east of 23.5° W should not be due to instrument error. Therefore, only a mean offset was calculated and applied to calibrate each corresponding group of profiles made by no. 70200068. The reasons for the abrupt drift in the salinity (as obtained from the conductivity sensors) are not clear, but it is likely that due to the repeated intensive usage, the conductivity sensors were contaminated or impacted (hit ship hull).

The shipboard TSG provides another source of validation and calibration of uCTD data. On R/V Meteor, the TSG (SBE38 for temperature sensor, SBE21 for conductivity sensor) measures temperature and salinity at an intake at approximately 6.5 m depth. For all three legs, the TSG conductivity cell was calibrated from salinity analysis of water samples taken at the water intake, and a comparison with CTD data (if available) was also done. The uCTD salinity calibration was done by calculating the conductivity offset between the uCTD at 6.5m and the averaged TSG conductivity within 5 min before and after the uCTD downcast. For probe no. 70200126, the drift of its conductivity sensor manifests also east of 39° W, the conductivity offset west of 39° W is about -0.022 S m^{-1}, and east of that it is about 0.094 S m^{-1}. These differences in conductivity correspond to a change in salinity of -0.015 and 0.08 g kg^{-1}, respectively. For probe no. 70200068, the conductivity offset west of 36° W is indistinguishable from zero, while east of that it is 0.156 S m^{-1}, which corresponds to a salinity difference of 0 and 0.15 g kg^{-1}. No trend in the offset east of 23.5° W is detected. For the 14.5° N section, we had uCTD, CTD, and TSG data available and the respective calibrations uCTD/CTD and uCTD/TSG could be compared. This was done in order to see if in case only TSG data are available (as is the case for the 11° S section), still reasonable calibration results could be achieved. For both probes, the TSG-derived drifts occurred in the same longitude range as they were detected using the CTD data. However, the magnitude of the offset was generally smaller for the TSG compared to the CTD-based method, especially for probe no. 70200126 in the longitude range west of 39° W, where even the signs of the offsets were opposite to each other. Such a difference is likely due to the fact that the CTD-based method employs a specific conservative temperature range where the salinity variation is small, while the TSG-based method focuses only at near-surface values (6.5 m), where the salinity varies in a broad range. Therefore, we would trust more the CTD-based method, and note that if the TSG-based method returns a small conductivity offset (< 0.03 S m^{-1}), one might need more caution to

apply this offset to calibrate the uCTD. However, one needs also more caution when applying the CTD-based calibration in regions, where the T/S relation of the central water shows a mixture effect of NACW and SACW. At the 11° S section, CTD data were only available at the beginning and end of the section; we could use only the TSG data as the primary source for validation. Fortunately no drift was detected in the uCTD probes conductivity cell, but a stable offset with a mean value of 0.131 and 0.073 S m^{-1} was detected and applied for probes nos. 70200068 and 70200138, respectively.

After the offset/drift calibration, all the uCTD data were gridded vertically from the original resolution (0.25 m at a nominal sinking speed of 4 m s^{-1}) to 1 m for the geostrophic velocity calculation later. Following *Rudnick and Klinke* (2007), we estimated that the calibrated and gridded uCTD data have an accuracy of 0.02-0.05 g kg^{-1} in salinity and 0.004 °C in temperature.

All calculations in this study are based on the Thermodynamic Equation of State for seawater 2010 (TEOS-10, *McDougall and Barker* 2011. TEOS-10 is introduced to replace the previous Equation of State, EOS-80, and it provides a thermodynamically consistent definition of the equation of state in terms of the Gibbs function for seawater. The most obvious change in TEOS-10 is the adoption of conservative temperature (Θ) and absolute salinity (S_A) to replace the potential temperature and practical salinity. Although the new equation of state has a non-negligible effect on the density field in the deep ocean, its effect in the upper ocean is expected to be small; therefore, our results obtained using TEOS-10 should be comparable with the previous studies.

2.2.2 ADCP measurement

Direct current velocity profiles were measured continuously during all three cruise legs with vessel-mounted 75 and 38 kHz Teledyne RDI Ocean Surveyors (OS75 and OS38). The OS75 was configured to measure at a rate of 2.2 s and a bin size of 8 m. The measurement range varied between 500 and 700 m. The OS38 was set to measure at a rate of 3.5 s and at 16 m (32 m) bin size during the 14.5° N (11° S) section. The measurement range was mostly 1200 m. Ship navigation information was synchronized to the ADCP system. The misalignment angles and amplitude factors were calibrated during post-processing. The processed data contain 10 min averaged absolute velocities in earth coordinates; the first valid bin for OS75 is centred at 18 m at 14.5° N and 13 m at 11° S, for OS38 is 21 m at both sections. In this study, only the OS75 velocity was used since it has a higher accuracy in upper layers and higher vertical

resolution. The uncertainties of 1 h averages were estimated by *Fischer et al.* (2003) to be 1-3 cm s^{-1}.

2.2.3 Wind data

We used three different wind datasets in our analysis. First, we used the observed wind speed and direction recorded with the R/V Meteor anemometer, mounted at a height of 35.3 m. The wind data were stored with a temporal resolution of 1 min. True wind speed and direction were calculated using ship speed and direction from the navigation system. On-station measurements were removed. The reduction from the observation height to 10 m standard height was calculated according to *Smith* (1988) and wind stress was calculated according to *Large and Yeager* (2004) assuming neutral stability. The final wind stress used for the Ekman transport calculation was binned in 50 km ensembles to filter out small-scale variability.

The blended Satellite-based level-4 Near-Real-Time wind stress product (hereafter satellite wind stress) from the Copernicus Marine Environment Monitoring Service (CMEMS) was used. The wind speed data are derived from retrievals of scatterometers aboard satellite METOPA (ASCAT) and Oceansat-2 (OSCAT) and combined with the ECMWF operational wind analysis and gridded to $0.25° \times 0.25°$ resolution in space and 6 h in time. The wind stress data were estimated using the COARE 3 model (*Fairall et al.*, 2003).

Moreover, the NCEP/NCAR monthly zonal wind stress at 14.5° N and 11° S corresponding to the months of the cruises (i.e. May and July 2013) was used to calculate the Ekman transport.

2.2.4 GECCO2 ocean state estimate

In order to integrate our local observational results into a large-scale circulation, the GECCO2 ocean state estimate was used and compared (*Köhl*, 2015). GECCO2 is a German version of the MIT general circulation model "Estimating the Circulation and Climate of the Ocean system" (ECCO, *Wunsch and Heimbach* 2006. It has $1° \times \frac{1}{3}°$ resolution and 50 vertical levels. GECCO2 includes the Arctic Ocean with roughly 40 km resolution and a dynamic/thermodynamic sea ice model of *Zhang and Rothrock* (2000). GECCO2 uses the adjoint method to bring the model into consistency with available hydrographic and satellite data (*Köhl*, 2015). The prior estimate of the atmospheric state is included by adjusting the control vector, which consists of the initial conditions for the temperature and salinity, surface air temperature, humidity, precipitation and the 10 m wind speeds from the NCEP RA1 reanalysis 1948-2011 (*Köhl*, 2015). The surface

fluxes are derived by the model via bulk formulae of *Large and Yeager* (2004). For the study period from May to July 2013 monthly and daily output data were available. It is important to note that the in-situ observational data measured during the cruises were not assimilated in the GECCO2 state estimate, while the satellite measured wind speed was assimilated but possibly modified via the GECCO2.

2.3 Methods

According to Eqs. 2.1 and 2.2, the meridional Ekman volume transport can be calculated from zonal wind stress data, as well as from observed ageostrophic velocity. Hereafter we refer to the wind-stress-based calculation as the "indirect method", and to the ageostrophic-velocity-based calculation as the "direct method". In this section, we describe some details of the geostrophic and ageostrophic velocity calculation, the definition of the penetration depth of the Ekman flow, the error estimate of the direct Ekman transport calculation, and different methods to derive the Ekman heat and salt fluxes.

2.3.1 Geostrophic and ageostrophic velocity calculations

According to the thermal wind relation, relative geostrophic velocity referenced to the velocity at the reference depth can be calculated from the density field measured by the CTD and uCTD. At 14.5° N, two sets of the relative geostrophic velocity were calculated independently from the CTD and uCTD datasets. For CTDs, the relative geostrophic velocity referenced to 200 m was computed between the adjacent stations (average distance about 75 km). For uCTDs, in order to take advantage of the high spatial resolution, the relative geostrophic velocity to 200 m was calculated between any closest pair of uCTD profiles with a minimum distance of 70 km (roughly the Rossby radius of deformation at this latitude). Along the 11° S section, CTD profiles were only taken in the vicinity of the coasts, and over most of the section only uCTD data are available (Fig. 2.1). Therefore the geostrophic velocity was computed from the combined CTD and uCTD dataset following the methodology applied to uCTD data at the 14.5° N section, except that at 11° S the minimum distance between the closest profiles was set to 90 km (roughly the Rossby radius of deformation at 11° S). Note that the distance between uCTD profiles for geostrophic velocity calculation is an arbitrary choice, and varying the distance from 70 to 110 km has a negligible effect on the total transport (less than 2 %).

To obtain the absolute geostrophic velocity, the reference velocity at 200 m was obtained

from the ADCP measurement. The ADCP velocity was projected to the normal direction of the cruise track and then averaged between the corresponding CTD/uCTD pairs. We did not include the ADCP velocity data recorded at the CTD stations, because velocity was repeatedly measured at a CTD station; zonally averaging the ADCP velocity would bias the result towards the on-station velocity. In previous studies (*Wijffels et al.*, 1994; *Chereskin et al.*, 1997; *Garzoli and Molinari*, 2001), the corresponding ADCP velocity at the reference depth was taken as the reference velocity, assuming that the flow at the reference depth was in geostrophic balance. However, the section-averaged ADCP velocity profile for the 14.5° N section shows a complicated vertical structure (Fig. 2.3a) and it is not obvious at which depth the flow is approximately in geostrophic balance. Thus, referencing the relative geostrophic velocity to the ADCP velocity only at a chosen depth may lead to a biased absolute geostrophic velocity. As a result, the ageostrophic velocity may be sensitive to the choice of the reference level. To overcome this problem, a reference velocity was calculated as an averaged offset between each relative geostrophic velocity and the corresponding ADCP velocity within a common depth range, over which the ageostrophic components are averaged to about 0. This averaged offset should represent the absolute geostrophic velocity at the reference depth and is roughly independent of the vertical variation due to the ageostrophic components. At 14.5° N, the common depth range for the CTD-based calculation is between 70 and 500 m, which is expected to be below the surface Ekman layer and covered by both CTD and ADCP measurement. Due to the limitations in the maximum deployment depth, the uCTD-based calculation covers the depth range between 70 and 250 m. At 11° S the depth range is between 100 and 300 m, which should also be below the Ekman layer and was covered by the uCTD and ADCP measurement.

The ageostrophic velocity was then calculated as the difference between the ADCP velocity and the absolute geostrophic velocity. Note that the choice of the depth range still affects the reference velocity due to the vertical variation in the ADCP meridional velocity. For example, using a depth range between 70 and 250 m for the CTD-based calculation (same as the uCTD depth range) would decrease the final ageostrophic velocity by 0.44 cm s^{-1}; using another depth range would not result in an absolute difference exceeding this value. This is much smaller compared to the uncertainty caused by using the ADCP velocity at a single depth as the reference velocity (up to 1.75 cm s^{-1}), as can be anticipated from the section-averaged meridional ADCP velocity (Fig. 2.3a). The sensitivity of the absolute geostrophic velocity to the choice of the reference level was also tested at 14.5° N. Changing the reference level from 150 to 250 m would make a change in the absolute geostrophic velocity indistinguishable from

zero.

2.3.2 Penetration depth of the Ekman flow

Because the ocean is not homogeneous, a control surface must be defined that characterizes the maximum penetration depth of the momentum flux into the upper ocean. One choice would be the MLD, which we defined as the depth where the density increased by 0.01 kg m^{-3} in reference to the value at 10 m (following *Wijffels et al.* 1994). Along both sections, the MLD is relatively shallow (on average 25.1 m at 14.5° N and 32.2 m at 11° S), and as such unlikely a representative of D_E (Figs. 2.3 and 2.4). According to the Ekman theory, D_E for water at 14.5° N with a typical vertical eddy viscosity A_v of 0.02 m^2 s^{-1} would be 33.1 m (see the definition of D_E in Eq. 2.1).

Alternatively a TTP has been defined as the shallowest depth at which the density gradient is larger than 0.01 kg m^{-4} (*Wijffels et al.*, 1994). The TTP is typically deeper than the MLD and better defines the transition depth between well-mixed and stratified ocean, up to which the momentum from the wind is transferred (*Chereskin et al.*, 2002). At some locations along both sections we observed two homogeneous layers of slightly different density and possibly a remnant of the seasonal mixed layer cycle. In these cases, the TTP depth was chosen as the deeper one of the depth that satisfies the density gradient criterion. Since TTP was defined based on a gradient criterion, it represents the bottom of a weakly stratified surface layer rather than a specific density surface. Along the 14.5° N section, the mean TTP depth is 45.8 m (Fig. 2.3a). At both ends of the section, the TTP coincides with the MLD and is relatively shallow, while in the remaining part of the 14.5° N section TTP is deeper than the MLD (Fig. 2.4c). Along the 11° S section, the mean TTP depth is 56.8 m, and the TTP is deeper than the MLD throughout the section (Figs. 2.3b and 2.4d).

2.3.3 Error estimate of the direct Ekman transport

The errors of the direct Ekman transport were estimated following *Chereskin and Roemmich* (1991) and *Wijffels et al.* (1994). Assuming that near-inertial motions are the dominant source of error, decorrelation length scales were calculated as the distance that the ship travelled in a quarter of the inertial period at 14.5° N (47.9 h) and 11° S (62.7 h) resulting in 130 and 230 km, respectively. In total, 38 segments of the 14.5° N section and 25 segments of the 11° S section were obtained by dividing the total distance of each section by the corresponding decorrelation

length scale, respectively. The westernmost and easternmost four segments of each section were omitted because of the anomalously weak wind near the eastern boundary and the strong boundary current in the western boundary region. The degree of freedom (DOF) of 30 and 17, respectively, was the number of the remaining segments. The ageostrophic transport within each segment was treated as an independent realization of the Ekman transport. Therefore, standard errors were calculated. Then the final error is given as the standard error times the DOF. Another factor that could lead to an uncertainty is the depth range used to calculate the reference velocity from the ADCP velocity. As discussed above, we argue that the vertical structure of the ageostrophic velocity should arise from the near-inertial motion and therefore, should be included already in this uncertainty estimate.

2.3.4 Ekman heat and salt flux calculation

The Ekman heat and salt fluxes, H_e and S_e, respectively, were calculated by combining the indirect and direct Ekman volume transport estimates with Θ and S_A from different sources. Note that in order to calculate the Ekman fluxes in the context of mass conservation (*Montgomery*, 1974), it has to be assumed that the Ekman volume transport in the upper layer is balanced by an equal and opposite geostrophic return flow at depth. This is a reasonable assumption and has been routinely adopted in many inverse studies (*Ganachaud*, 2003). To account for this return flow, an averaged conservative temperature, $\overline{\Theta}$, and absolute salinity $\overline{S_A}$ were subtracted from the in-situ Θ and S_A at each section. $\overline{\Theta}$ and $\overline{S_A}$ are the zonally and vertically (0-5000 m) averaged conservative temperature and absolute salinity, calculated from the annual climatology of the World Ocean Atlas 2013 v2 (*Locarnini et al.*, 2013; *Zweng et al.*, 2013) at each section. In the following, the calculation details of the Ekman heat flux and transport-weighed Ekman temperature are given; the calculation of the Ekman salt flux and transport-weighted Ekman salinity is an analogue.

2.3.4.1 Direct methods

By using the in-situ Θ together with the ageostrophic velocity within the layer from the sea surface to the TTP (referred to as the TTP layer), the Ekman heat flux H_e was calculated (referred to as the direct TTP/profile).

$$H_e = \rho C_p \int_{x_1}^{x_2} \int_{-TTP}^{0} (\Theta(x,z) - \overline{\Theta}) v_{ageo}(x,z) dz dx, \tag{2.3}$$

where C_p is the specific heat capacity of sea water at constant pressure, ρ is the density of sea water, in this study we assumed a constant $C_p = 4000$ J kg^{-1} K^{-1} and a constant $\rho = 1025$ kg m^{-3}, v_{ageo} is the ageostrophic velocity, Θ is the in-situ conservative temperature. $\overline{\Theta}$ is the mean conservative temperature at the corresponding section.

It is useful to consider the Ekman heat flux as the product of the Ekman volume transport, M_y, and the transport-weighted temperature, Θ_E. The transport-weighted temperature then can be calculated as follows:

$$\Theta_E = \frac{\int_{x_1}^{x_2}\int_{-TTP}^{0}\Theta(x,z)v_{ageo}(x,z)dzdx}{M^y_{direct}}. \tag{2.4}$$

As a comparison to the direct TTP/profile method, the Ekman heat fluxes using only in-situ SST from the CTD and uCTD were also calculated (referred to as the direct TTP/surface). This was done by replacing the in-situ $\Theta(x,z)$ in Eqs. (2.3) and (2.4) with the in-situ SST $\Theta(x,z=0)$.

The uncertainty of the direct Ekman heat and salt fluxes was estimated following *Chereskin et al.* (2002). Since the wind direction was predominantly uniform and westward, the uncertainty should mainly arise from the ageostrophic velocity that was opposite to the expected Ekman flow direction. Therefore, the uncertainty was calculated still using Eqs. (2.3) and (2.4), except that only southward or northward ageostrophic velocity was used in both the numerator and denominator for the 14.5° N or 11° S section, respectively.

2.3.4.2 Indirect surface method

Often Ekman heat and salt fluxes are estimated by combining the Ekman volume transport inferred from wind stress with the SST and sea surface salinity (SSS) from a climatology or satellite measurements (e.g. *McCarthy et al.* 2015). Here, we calculated the heat flux using in-situ wind and in-situ SST data (referred to as the indirect surface) to compare with the direct estimates. Additionally, annual Ekman heat and salt fluxes (referred to as the indirect annual) were calculated using an annual average of the monthly NCEP/NCAR reanalysis wind stress data between 1991 and 2013 and the annual average of SST and SSS from the *Roemmich and Gilson* (2009) monthly Argo climatology (hereafter RG climatology). Following *Levitus* (1987), the Ekman heat flux for the indirect surface method was calculated as

$$H_e = C_p \int (\Theta(x,z=0) - \overline{\Theta})\frac{\tau_x}{f}dx, \tag{2.5}$$

where τ_x is the in-situ wind stress in the tangential direction of the cruise track, f is the Coriolis parameter, and $\Theta(x,z=0)$ is the in-situ SST. The transport-weighted temperature

was calculated as follows:

$$\Theta_E = \frac{\int \Theta(x, z=0)\frac{\tau_x}{\rho f}dx}{M^y_{indirect}}. \tag{2.6}$$

The indirect annual method is an analogue to the indirect surface method, except that the Ekman volume transport and SST were derived from the NCEP/NCAR reanalysis wind stress and RG climatology, respectively.

2.3.4.3 Indirect TTP method

Wijffels et al. (1996) assumed a linear Ekman velocity profile between the surface and TTP and calculated the Ekman heat and salt fluxes using climatological wind stress data, combined with the in-situ temperature and salinity. Here we followed their method and used the in-situ Θ, S_A, and wind to calculate the Ekman heat and salt fluxes (referred to as the indirect TTP) as a counterpart to the direct TTP method.

$$H_e = C_p \int \left[\frac{2}{3}\Theta(x, z=0) + \frac{1}{3}\Theta(x, z=TTP) - \overline{\Theta}\right]\frac{\tau_x}{f}dx, \tag{2.7}$$

where $\Theta(x, z = TTP)$ is the in-situ conservative temperature at TTP depth from the CTD/uCTD. The transport-weighted temperature was calculated as follows:

$$\Theta_E = \frac{\int \left[\frac{2}{3}\Theta(x, z=0) + \frac{1}{3}\Theta(x, z=TTP)\right]\frac{\tau_x}{\rho f}dx}{M^y_{indirect}}. \tag{2.8}$$

2.4 Results and discussion

2.4.1 Upper layer hydrography at 14.5° N and 11° S

Along both sections (Fig. 2.2a, b) the typical upward tilting of isotherms towards the east, as a result of the subtropical gyre circulation, can be seen. Along the nominal 14.5° N section, the water in the upper 50 m, compared to that at 11° S, was relatively warm and fresh, with an averaged Θ and S_A of about 26.03 °C and 36.15 g kg^{-1}, respectively. The minimum S_A core near the western boundary probably originates from the freshwater runoff from the Amazon River (Fig. 2.2c). Together with the warm temperature, it forms the lightest water observed along the section (Fig. 2.2e). A subsurface salinity maximum layer of STUW is centred at 100 m depth with S_A greater than 37.2 g kg^{-1}. STUW is formed in the subtropical Atlantic with a SSS maximum due to excessive evaporation, and is subducted equatorward (*Talley et al.*, 2011). The upward tilt of the isopycnals from west to east is suggestive of a net southward geostrophic transport when excluding the western boundary, where sharp deepening of the

isopycnals implies a northward, intensified boundary current (Fig. 2.2g). At 11° S, the surface water was cooler and more saline than that at 14.5° N, with an averaged Θ and S_A of about 24.52 °C and 36.69 g kg^{-1}. The STUW with maximum salinity larger than 37.3 g kg^{-1} was centred at about 100 m, but was even saltier than that at 14.5° N. Likewise, a net northward geostrophic flow can be anticipated from the displacement of the isopycnals. At the western boundary, the North Brazil Undercurrent (NBUC) is characterized by a narrow and strong northward velocity band west of 35° W (*Schott et al.*, 2005) (Fig. 2.2h). In the hydrographic data Θ/S_A variability is seen at both sections that are associated with mesoscale eddies. For instance, at 14.5° N/25° W and 11° S/7° E, cyclonic and anticyclonic eddies were characterized by the upward peak of the isotherms, and were clearly visible from the geostrophic velocity sections (Fig. 2.2g, h).

The daily Θ and S_A data of the GECCO2 state estimate were extracted from the model grid to the nearest time and position of the ship measurement. In general, GECCO2 daily data reproduced the observed hydrographic structure very well (not shown). The upward tilt of the isopycnals from the west to the east and the subsurface salinity maximum with S_A larger than 37.2 g kg^{-1} were clearly captured by GECCO2. However, the most obvious difference was at the western boundary of 11° S, where the surface salinity was not as high as the observed values, and the isopycnals were not tilting in the same direction, indicating that the shallow western boundary current in the GECCO2 flowed in the opposite direction compared to the observation at 11° S. But we expect that this difference should not impact the ageostrophic velocity calculation, since the geostrophic velocity must be removed from the total velocity.

2.4.2 Vertical structure of the ageostrophic flow

Although northward (southward) ageostrophic velocity at 14.5° N (11° S) dominates the upper 50-70 m (Fig. 2.2i, j), as expected from the persistent westward trade winds, the appearance of southward (northward) velocity at 14.5° N (11° S) in the upper 50-70 m and below indicates the existence of non-Ekman ageostrophic components in the water column. This will be discussed in detail below. The section-averaged ageostrophic velocity based on CTD data at 14.5° N shows a relatively complicated vertical structure with multiple maxima and minima (Fig. 2.3a). It has a northward maximum velocity of 3.5 cm s^{-1} near the surface, and decreases to about 0.3 cm s^{-1} at about 60 m, followed by a minor peak at about 80 m before approaching 0 at 100 m. Another peak of 1 cm s^{-1} appears at about 150 m, and below 180 m the velocity changes direction. When the ageostrophic velocity is calculated based on the uCTD data, it

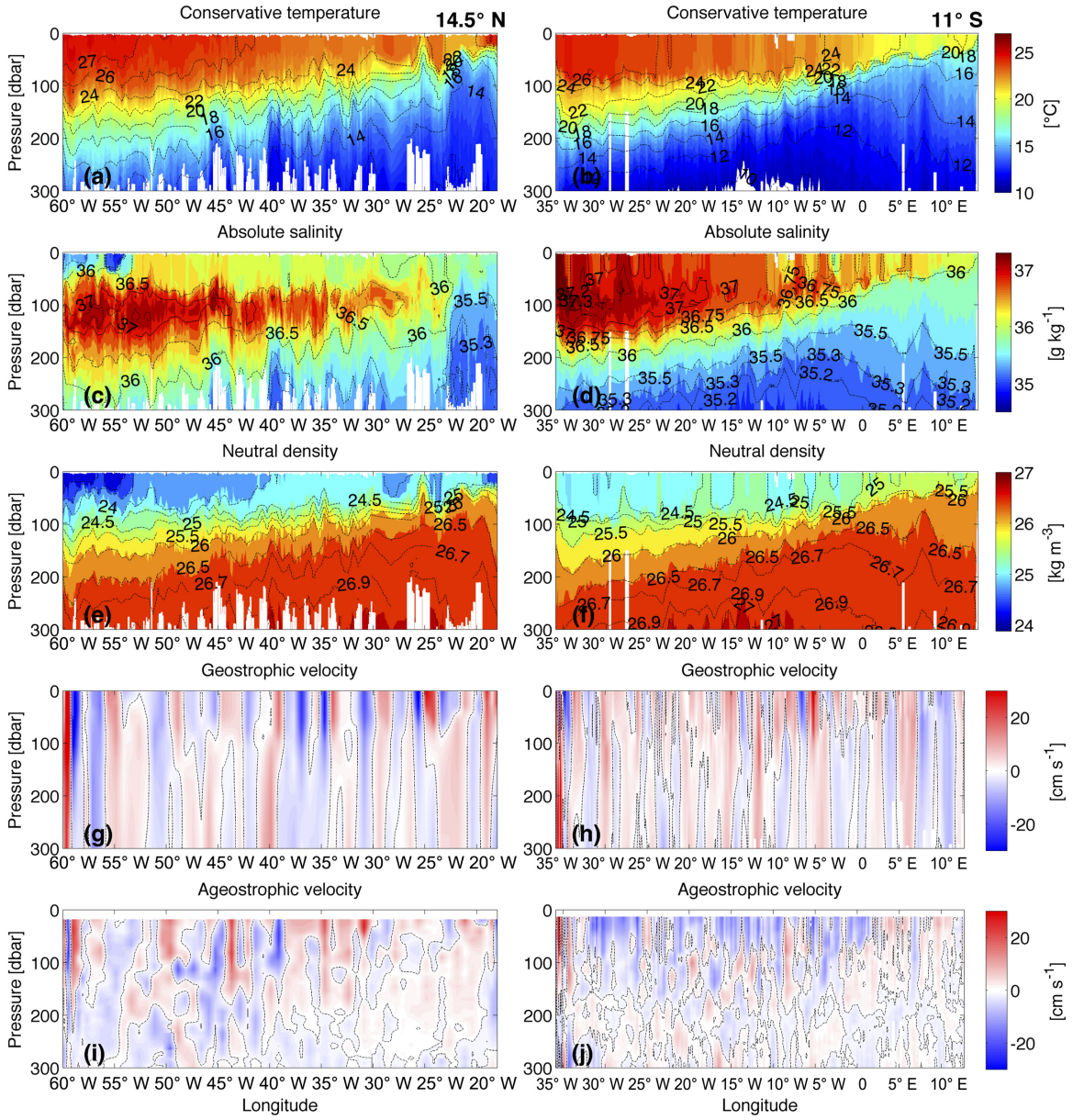

Figure. 2.2 | Vertical sections of conservative temperature in °C (a, b), absolute salinity in g kg^{-1} (c, d), neutral density in kg m^{-3} (e, f), geostrophic velocity in cm s^{-1} (g, h), and ageostrophic velocity in cm s^{-1} (i, j) at 14.5° N (left) and 11° S (right). All the available CTD and uCTD data were used to produce (a-f), and the contours were plotted with every fifth value for visual clarity. (g) and (i) were calculated using only CTD data, while (h) and (j) were calculated using CTD and uCTD data. The blanks were due to the shallow measurement depth of the uCTD.

has a very consistent structure and strength compared to the CTD-based ageostrophic velocity (Fig. 2.3a). This is meaningful information as the hydrographic data at 11° S consist primarily of uCTD data. The good agreement between the CTD and uCTD data analysis at 14.5° N justifies the use of either one or the other. At 11° S, the ageostrophic velocity shows a near-surface southward maximum of 4.3 cm s^{-1} , decreases almost linearly in the upper 70 m, and

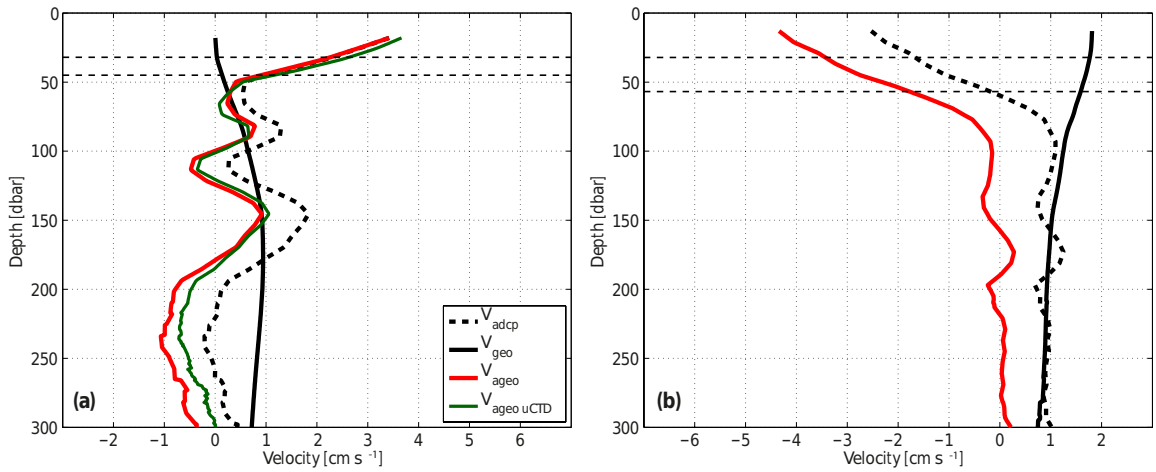

Figure. 2.3 | Section-averaged cross-track velocity profiles at (a) 14.5° N and (b) 11° S. In (a), the solid red curve and the solid black curve are the ageostrophic and geostrophic velocity calculated from the CTD data, respectively. The dark green curve is the ageostrophic velocity profile based only on the uCTD data. In (b), the solid red curve and solid black curve are the ageostrophic and geostrophic velocity calculated from the combination of the CTD/uCTD data, respectively. The dashed black curve is the ADCP velocity. The upper horizontal dashed line denotes the basin-wide averaged MLD and the lower one denotes the basin-wide averaged TTP depth.

gradually approaches 0 at about 100 m (Fig. 2.3b). In contrast to the northern section the vertical variations of the ageostrophic velocity profile below 100 m are very small.

Assuming that the Ekman balance would hold true along the analysed sections, the ageostrophic velocity would decrease undisturbed from its surface maximum to about 0 at a certain depth (Ekman depth, D_E). However, the observed wave-like structure at 14.5° N indicates that other processes must play a role in setting the section mean ageostrophic flow field. To identify this wave-like structure, we tried to separate the non-Ekman ageostrophic flow from the other components by using the ADCP velocity. A residual velocity was calculated by subtracting an 80 m boxcar filtered velocity profile from the original ADCP meridional velocity (Fig. 2.4a, b). The 80 m filter window was determined based on the vertical length scale of the wave-like structure in the section-averaged ageostrophic velocity profile by visual inspection. At 14.5° N, vertically alternating structures with wavelengths of 60-80 m are clearly visible, are coherent and persistent throughout the section, and are most pronounced between 52 and 46° W (Fig. 2.4a). At 11° S, similar signals are visible for most of the section, but are not as strong as at 14.5° N (Fig. 2.4b).

Zonally averaging the residual velocity results in a velocity profile with a vertically alternating structure similar to that in the section-averaged ageostrophic velocity in both strength and

structure, indicating that the vertical variation in the ageostrophic velocity mainly arises from the presence of high-order baroclinic waves. Figure 2.4c and d show the buoyancy frequency (N^2) for the two sections, respectively. It appears that the wave-like signals occur mainly in the strongly stratified layer (pycnocline) marked by high N^2 values. N^2 is calculated as follows:

$$N^2 = \frac{g}{\rho_0}\frac{\partial \rho(z)}{\partial z} \tag{2.9}$$

where g is the gravitational acceleration, $\rho_0 = 1025$ kg m^{-3} is the reference density, and $\rho(z)$ is the in-situ potential density as a function of depth, z. $\rho(z)$ was calculated by using a combination of CTD and uCTD profile data with a re-gridded vertical resolution of 5 m at both sections.

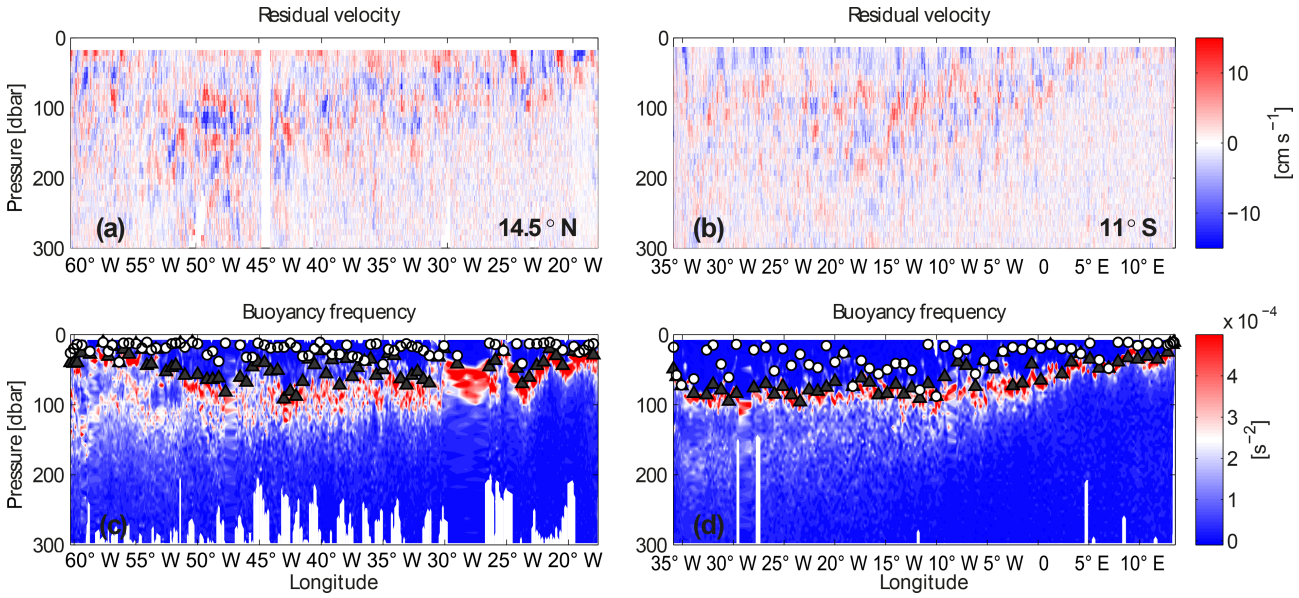

Figure. 2.4 | Vertical sections of residual meridional velocity in cm s^{-1} at (a) 14.5° N and (b) 11° S and of buoyancy frequency calculated from uCTD/CTD at (c) 14.5° N and (d) 11° S. Northward velocity in (a, b) is shaded in red, southward in blue. The residual velocity is calculated by subtracting an 80 m boxcar filtered profile from the original ADCP profile. The white circles in (c, d) denote the MLD; the black triangles denote the TTP (see text for details). The MLD and TTP plotted here are subsampled for visual clarity. Note that no uCTD measurements were conducted between 30 and 25° W at 14.5° N.

Chereskin and Roemmich (1991) also observed energetic, circularly polarized, relative currents of large horizontal coherence below the base of the mixed layer at 11° N in the Atlantic. They described the signal as the propagation of near-inertial internal waves and argued that the presence of a near-inertial peak in internal wave spectra, together with continuously varying wind forcing, would guarantee the appearance of these waves. Using satellite-based wind stress data, we examined the changes in wind stress at the measurement points within the last 2 weeks

before the ship arrived at the measurement points. Although the wind stress strongly changed along the whole section, it is still not indicative why the wave signal is strongest between 52 and 46° W at 14.5° N. It is tempting to believe that these waves are near-inertial internal waves. However, due to the fact that the ship moved nearly constantly except when it was on station, it is extremely difficult to identify what exactly these signals are. More sophisticated methods may be applied to analyse the wave-like signal; for instance, *Smyth et al.* (2015) took the Doppler shift in the shipboard current measurement into account, and translated observed Yanai wave properties into the reference frame of the mean zonal flow. But this is obviously beyond the scope of this work.

2.4.3 Ekman transport

2.4.3.1 Indirect method

According to Eq. (2.1), the Ekman transport can be calculated from the wind stress data (referred to as the indirect method) by integrating the left-hand side of Eq. (2.1) zonally. The in-situ wind stress data and a satellite-based wind stress product from CMEMS were used. The satellite wind stress data were extracted from the original grid to the nearest time and nearest position of the ship navigation. Both in-situ and satellite wind stress were projected to the tangential direction of the cruise track, so that the cross-sectional Ekman transport at each grid point was calculated. Note that both sections were occupied nominally zonally; therefore, we will refer to cross-sectional Ekman transport as meridional Ekman transport for simplicity hereafter.

Overall, the satellite wind stress agrees well with the ship wind stress (Fig. 2.5) except in the region between 40 and 30° W at 14.5° N, where the zonal ship wind stress is larger than the zonal satellite wind stress, and at 11° S the ship wind stress is generally smaller than the satellite wind stress. Since the 10-m wind speeds from the ship and satellite are very close to each other at both sections (not shown), the difference in the wind stress may be due to the use of a different drag coefficient formulation (COARE 3 for the CMEMS wind product; *Large and Yeager* 2004, for the ship wind stress). In comparison to the NCEP/NCAR monthly zonal wind stress, the weaker ship wind stress in the western half of the 14.5° N section indicates that the cruise started with anomalously weak winds, while at 11° S the observed wind stress (both ship and satellite observation) was consistent with the monthly mean wind stress. It is also reported that differences in the different wind stress data may also arise from the unresolved

local effect by the satellites and NCEP data (*Mason et al.*, 2011; *Pérez-Hernández et al.*, 2015). For instance, near the Canary Islands, the NCEP/NCAR monthly data do not resolve the Von Karman structure caused by the interaction of wind with the islands due to its low resolution.

As expected, at 14.5° N, the indirect estimate of the Ekman transport from the in-situ wind stress is 6.7 ± 3.5 Sv, only 0.4 Sv larger than that from the satellite wind stress. Using the monthly mean wind stress from NCEP/NCAR during the M96/M97 cruise month (May 2013), the total transport is 8.8 ± 1.4 Sv. The difference between the monthly wind estimate and in-situ wind estimate is mainly due to the anomalously weak wind when the cruise started from the western boundary (Fig. 2.5a). At 11° S, the indirect Ekman transport from the in-situ wind stress is -13.6 ± 3.3 Sv ("-" denotes southward transport), while the transport from the satellite wind stress is 2.0 Sv higher, due to the higher value of the satellite wind stress (Fig. 2.5b). The NCEP/NCAR monthly wind stress in July 2013 returns a transport of -15.1 ± 1.9 Sv. The errors shown with the indirect ship wind estimates are given by the standard deviation of the long-term Ekman transport calculated using 6-h NCEP/CFSr wind stress between the years 2000 and 2011 at the two latitudes. The errors of the monthly estimates are given by the standard deviation of the monthly mean Ekman transport in May (July) between 1979 and 2013 at 14.5° N (11° S) calculated from the NCEP/NCAR monthly wind stress. Another source of uncertainty may arise from the wind stress calculation using different bulk formulas, which could lead to an uncertainty as large as 20% (*Large and Pond*, 1981). This may explain the difference in the indirect estimates between using the in-situ wind stress and the satellite wind stress at 11° S.

2.4.3.2 Direct method

The direct meridional Ekman transport is derived from vertically integrating the ageostrophic velocity profiles (Eq. 2.1, right-hand side). As already mentioned, one critical assumption is the integration depth (D_E). Applying the TTP as an estimate of D_E, the total Ekman transport at 14.5° N based on CTD data is 6.2 ± 2.3 Sv, while applying a uniform depth of 50 m results in an alternative estimate of 6.5 ± 1.9 Sv, and applying the local MLD results in a transport of 5.1 ± 1.4 Sv. When integrating the ageostrophic velocity calculated from the uCTD data to the TTP, the Ekman transport is 6.6 ± 2.3 Sv. At 11° S, the direct estimate by applying the TTP, a uniform depth of 80 m, and the MLD is -11.7 ± 2.1, -12.0 ± 2.4, and -8.0 ± 1.4 Sv, respectively. The errors given with the transport estimates were calculated by considering the aliasing effect of the inertial waves during the cruises following *Chereskin and Roemmich*

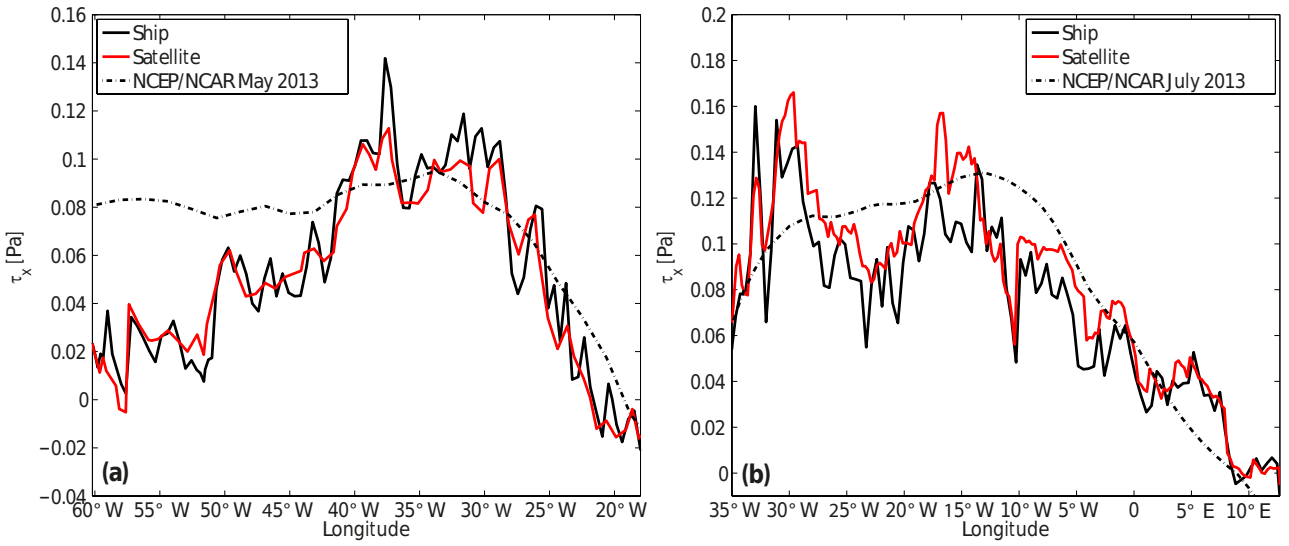

Figure. 2.5 | Zonal wind stress along (a) 14.5° N and (b) 11° S. Ship wind stress (black line) was binned in a 50 km interval. The satellite wind stress data (red) were extracted to the nearest ship time and position. The NCEP reanalysis monthly zonal wind stress (black dashed line) at the same latitude in the cruise month is also plotted.

(1991) as described in Sect. 2.3.3.

Because the shallowest valid bin depth of the ADCP measurement was 18 m (13 m) at 14.5° N (11° S), the ageostrophic velocity was extrapolated linearly to the surface using the value of the first two bins. Note that we did not assume a surface maximum of the ageostrophic velocity everywhere, since for individual profiles the ageostrophic velocity at the first bin depth may be smaller than that at the second bin, which would result in a smaller surface ageostrophic velocity. In previous studies (*Chereskin and Roemmich*, 1991; *Wijffels et al.*, 1994), the velocity above the first ADCP bin was assumed to equal the value at the first bin. Using this assumption would reduce Ekman transport at 14.5° N by 0.56 Sv (9% of total northward transport), and at 11° S by 0.14 Sv (1% of total southward transport). According to the classical Ekman theory, the surface Ekman velocity (V_0) is 45° to the right (left) of the wind direction in the Northern (Southern) Hemisphere and can be derived from the total wind stress (see the definition of V_0 in Eq. 2.1). As a comparison to the linear extrapolation above the first ADCP bin, we also calculated the meridional Ekman velocity at the surface using the total in-situ wind stress and a constant A_v of 0.02 m^2 s^{-1}. Then the meridional ageostrophic velocity above the first ADCP bin was linearly interpolated using the value at the first bin and the surface meridional Ekman velocity predicted from the in-situ wind stress. The resulting Ekman transport is 1.2 Sv (0.7 Sv) smaller than that using a linear extrapolation method at 14.5° N (11° S). Note that we chose a linear extrapolation method, because it resulted in a better agreement between the

indirect and direct estimates, but it may overestimate the total ageostrophic transport.

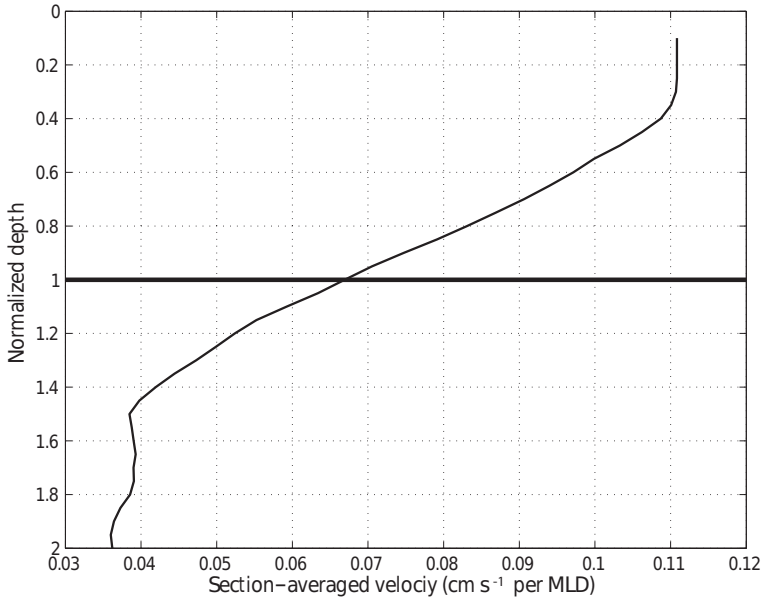

Figure. 2.6 | Section-averaged ageostrophic velocity at 14.5° N, normalized in depth by the local MLD. Velocity above 18 m is set equal to the velocity at 18 m. MLD is defined as the depth where the density is 0.01 kg m^{-3} different from the value at 10 m.

A question that follows is whether the ageostrophic flow in the mixed layer has shear or is constant with depth referred to a slab-like shape. Given the large variation of the MLD throughout the sections, basin-wide averages are inconclusive. *Chereskin and Roemmich* (1991) found shear structure in the mixed layer at 11° N in the Atlantic, while *Wijffels et al.* (1994) reported a slab-like shape at 10° N in the Pacific, and attributed the shear structure found by *Chereskin and Roemmich* (1991) to an improper definition of the MLD. Following their method, the depth was normalized by the local MLD before averaging the ageostrophic velocity across the basin (Fig. 2.6). At 14.5° N, for a slab-like ageostrophic structure, Fig. 2.6 would show a nearly constant profile from the surface to about the MLD. Instead, it shows strong shear above the MLD. Such strong shear is insensitive to the definition of the MLD. For example, choosing a density threshold of 0.005 kg m^{-3}, the shear still exists below 0.4 MLD. At 11° S, no slab-like structure in the ageostrophic velocity was found, either. The constant value above 0.4 MLD is a consequence of using a constant velocity above 18 m, the shallowest ADCP bin. Therefore, we would conclude that ageostrophic shear exists within the mixed layer in our cases, as expected from the classical Ekman theory.

The cumulative Ekman transport from the western to the eastern boundary shows an overall match between the direct and indirect methods (Fig. 2.7a, b). At 14.5° N, the in-situ wind was

relatively weak at the beginning and the end of the section. Correspondingly, the increment in transport within these two segments was moderate, while in the central part of the section, where the wind was strong, the rapid accumulation of Ekman transport is directly visible in both indirect and direct estimates. The direct estimates using TTP and 50-m depth are very close to the in-situ wind estimates. The estimate using 50-m depth tends to overestimate the transport close to both ends of the section. Applying the MLD as integration depth tends to underestimate the total transport by about 1.5 Sv, compared to the ship wind estimate. This is mainly because it fails to capture the increase between 30° W and 25° W. Note that the uCTD-based direct estimate is consistent with the CTD-based estimates, though it overestimates the transport in the middle of the section; the total transport as well as the transport structure are similar. This may be a result of the higher spatial resolution of the uCTD measurement, which captures more details in the horizontal features introduced by the wind.

At 11° S, the wind was strong in the western half of the basin and gradually weakened in the eastern half towards the eastern boundary. Correspondingly, the Ekman transport accumulates rapidly to about 12 Sv at 0° E, east of which the increment is very small for both direct and indirect estimates. Among the direct estimates, integrating the ageostrophic velocity to 80 m and TTP returns nearly identical transport in the western half of the section; the difference in the eastern half mainly reflects the shallower TTP towards the eastern boundary, while using the MLD for the integration underestimates the Ekman transport from the very beginning. Note that at both sections, the direct estimate using MLD is about one-fourth smaller than that using TTP depth. This agrees with the findings at 10° N in the Pacific by *Wijffels et al.* (1994), who reported that the Ekman flow within the mixed layer accounted for about two-thirds of the total Ekman transport, and the in-situ wind predicted the Ekman transport down to the TTP. Recalling the definition of D_E in Eq. (2.1), the vertical eddy viscosity A_v can be estimated by using TTP as a representative of D_E. At 14.5° N, the mean A_v is 0.038 $m^2\ s^{-1}$, and at 11° S, the mean A_v is 0.045 $m^2\ s^{-1}$. These results fall in the range of previous estimates of A_v, which vary by more than 1 order of magnitude (*Price et al.*, 1987; *Chereskin*, 1995; *Lenn and Chereskin*, 2009).

2.4.4 Ekman transport from GECCO2

The daily data of the GECCO2 state estimate (2008 to 2014) allowed us to estimate the model Ekman transport, inspect the vertical structure of the ageostrophic velocity in the model, and compare these results with the observations for the corresponding cruise time periods. The

daily data were first extracted from the model grid to the nearest ship time and position. The Ekman transport in GECCO2 was calculated in a similar manner to the direct method used for the observational data. An ageostrophic velocity was calculated as the difference between the geostrophic velocity and total velocity with a reference depth of 200 m. The geostrophic velocity was computed from the temperature and salinity of GECCO2. The direct estimate of the meridional Ekman transport in GECCO2 was obtained by integrating the meridional ageostrophic velocity vertically and zonally.

The section-averaged ageostrophic velocity at both sections shows a near-surface maximum at about 15 m, and then decreases sharply to 0 at about 50 m; the flow is purely geostrophic below 60 m (not shown). This vertical distribution of ageostrophic velocity indicates that the wind-driven Ekman component is the predominant contributor to the ageostrophic velocity in the GECCO2 model, and that nearly all the wind energy is utilized for the Ekman transport and confined to the upper 50 m at both sections. The total transport by integrating the ageostrophic velocity to 50 m is 7.6 Sv at 14.5° N and 12.0 Sv at 11° S, respectively (Fig. 2.7), which is close to the indirect Ekman transport estimates based on the GECCO2 daily wind stress of 7.4 Sv and 13.4 Sv, respectively.

This result agrees very well with the observed direct Ekman transport, which is likely due to the fact that the GECCO2 daily wind stress has a similar magnitude to the in-situ wind stress. The observed ageostrophic cumulative transport shows strong mesoscale fluctuations throughout the sections, which are characterized by the presence of northward and southward ageostrophic velocity even though the in-situ wind is persistently westward, while the GECCO2 ageostrophic transport accumulates smoothly (Fig. 2.7).

2.4.5 Ekman heat and salt fluxes

The Ekman volume, heat, and salt fluxes calculated using different methods are summarized in Table 2.1. In the previous sections, we have shown that the TTP is a reasonable assumption for the depth of D_E for both sections. Hence, the direct TTP/profile method should give us the best estimate of the heat and salt fluxes. It is clear that the differences in Ekman volume transports dominate the differences in the resulting Ekman heat and salt fluxes. The higher Ekman volume transport by the indirect methods leads to higher heat and salt fluxes compared to the direct methods at both sections. At 14.5° N, the transport-weighted Ekman temperature from the direct TTP/surface method is 0.10 °C higher than that from the direct TTP/profile method. This temperature difference corresponds to a change in the heat flux

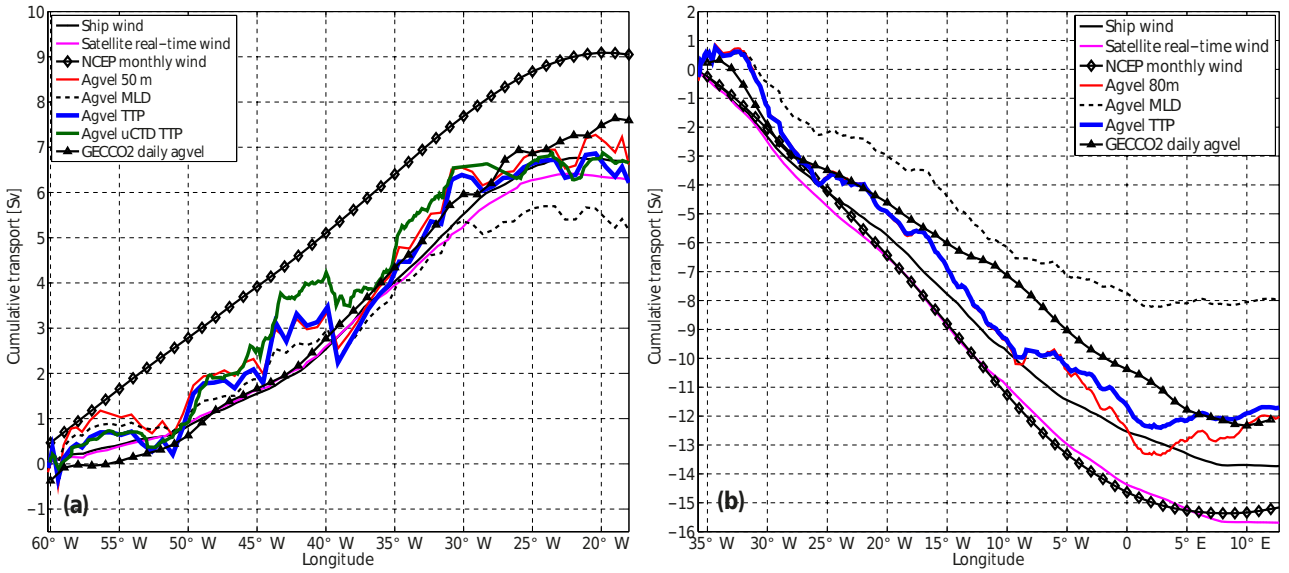

Figure. 2.7 | Cumulative meridional Ekman transport from the western to the eastern coast (a) at 14.5° N and (b) at 11° S. For both sections, the black solid curve marks the indirect Ekman transport estimate from the in-situ wind stress; the magenta solid curve denotes that from the satellite wind stress; and the black diamond line denotes that from the NCEP/NCAR monthly wind stress. The solid blue curve denotes the direct estimate by integrating the ageostrophic velocity to the TTP, the red solid to a uniform depth (50 m at 14.5° N and 80 m at 11° S), and the black dashed line to the MLD. The black triangle line represents the direct estimate based on the GECCO2 daily data. The dark green line in (a) represents the direct estimate integrated to the TTP based only on the uCTD data.

of only less than 1%, which is very small compared to the uncertainty caused by the volume transport uncertainty. The indirect TTP method returns the Ekman temperature and salinity value very close to that of the direct TTP/profile method, indicating that the assumption of a linear Ekman velocity profile between the surface and the TTP depth may be reasonable. This could be potentially interesting, since this method is independent of the ageostrophic velocity.

At 11° S, the difference between the direct TTP/profile and direct TTP/surface methods is negligible. The transport-weighted Ekman temperature from the indirect TTP and surface methods is significantly smaller than that from the direct methods. This may be caused by a combined effect of stronger Ekman volume transport by the indirect method near the eastern boundary (Fig. 2.7) and the cooler water temperature due to coastal upwelling. In other words, the indirect calculation tends to give excessive weighting to the cooler water, which results in lower values in the transport-weighted Ekman temperature. Such a combined effect has a limited impact on the Ekman salinity.

The difference in the Ekman heat flux when using temperature at the surface or within the TTP layer is much smaller than that for the extreme case at the end of the summer monsoon in

the Indian Ocean in September 1995 reported by *Chereskin et al.* (2002). The choice of Ekman temperature and salinity has a negligible effect on the resulting heat and salt fluxes across the sections studied here.

Note that at 14.5° N (except for the indirect annual method) the Ekman heat fluxes (0.41 to 0.44 PW) estimated using direct and indirect methods based on ageostrophic velocity and in-situ wind are generally smaller compared with the estimates of 0.7 to 0.8 PW by *Levitus* (1987) or 0.6 to 0.8 PW by *Sato and Polito* (2005). As described above, both the direct and indirect methods in this study reflect the Ekman transport driven by the in-situ wind, which is weak compared to the monthly wind, especially in the western basin (Fig. 2.5a). By using the annual mean wind stress from NCEP/NCAR reanalysis and SST from RG climatology, the Ekman heat flux is 0.58 PW, which is close to the estimates of *Sato and Polito* (2005). At 11° S, the direct and indirect Ekman heat fluxes (0.8 to 0.96 PW) are rather close to the estimate of 1.05 PW by *Levitus* (1987) or within the range of values (0.7 to 1.0 PW) estimated by *Sato and Polito* (2005). Here, the Ekman volume transports estimated from in-situ wind and from the annual averaged wind were similar.

It is worth noting that the Ekman salt flux presented in this study may not be representative of an annual or long-term mean Ekman salt flux, but it may provide insight into the sensitivity of the Ekman salt flux to changes in Ekman volume transport and Ekman-layer salinity. This might help in constraining salt conservation and resulting freshwater flux in studies of the meridional overturning circulation in the same region.

Table. 2.1 | Meridional Ekman volume (M_y in Sv), heat (H_e in PW) and salt (S_e in 10^6 kg s^{-1}) fluxes calculated using different methods, and the transport-weighted temperature Θ_E and salinity S_{AE} in the Ekman layer. Positive and negative fluxes denote northward and southward fluxes, respectively. The uncertainties of the Ekman heat and salt fluxes are 0.4 PW and 4.5×10^6 kg s^{-1} at 14.5° N, and 0.3 PW and 6.5×10^6 kg s^{-1} at 11° S, respectively. The uncertainties of the transport-weighted Ekman temperature and salinity is 0.20 °C and 0.15 g kg^{-1} at 14.5° N, and 0.11 °C and 0.10 g kg^{-1} at 11° S, respectively.

			Section									
			14.5° N					11° S				
			Θ_E	s_{AE}	M^y	H_e	S_e	Θ_E	s_{AE}	M^y	H_e	S_e
Method	Direct	TTP/profile	25.52	36.33	6.21	0.413	5.40	25.41	36.83	-11.71	-0.842	-17.69
		TTP/surface	25.61	36.34	6.21	0.415	5.49	25.41	36.80	-11.71	-0.842	-17.38
	Indirect	TTP	25.46	36.34	6.68	0.443	5.72	25.13	36.81	-13.64	-0.965	-20.50
		Surface	25.65	36.29	6.68	0.448	5.57	25.20	36.78	-13.64	-0.946	-20.04
		Annual	26.46	36.13	8.31	0.584	5.56	25.53	36.73	-11.02	-0.799	-15.49

2.5 Summary

The Ekman volume, heat and salt transport across zonal sections at 14.5° N and 11° S in the Atlantic were calculated by using an ageostrophic-velocity-based method (direct method) and a wind-stress-based method (indirect method). A cross-sectional ageostrophic velocity was calculated at each section following *Chereskin and Roemmich* (1991) and *Wijffels et al.* (1994) by subtracting the geostrophic velocity from the cross-section component of the ADCP velocity. At both sections, underway-CTD profiles were used for the ageostrophic velocity calculation. A comparison between the results based on standard CTD and uCTD data at 14.5° N revealed a consistent transport estimate with a robust vertical ageostrophic velocity structure and horizontal distribution of the Ekman transport. This has established our confidence in performing a similar calculation for the 11° S section, along which primarily uCTD profiles were taken.

The section-averaged ageostrophic velocity at 14.5° N and 11° S has a near-surface northward and southward maximum of 3.5 and 4.3 cm s^{-1}, and decreases below to reach about zero at 60 m and 100 m, respectively. This is an indication of the Ekman spiral, and is consistent with the findings of *Chereskin and Roemmich* (1991) at 11° N in the Atlantic, *Wijffels et al.* (1994) at 10° N in the Pacific, and *Chereskin et al.* (1997) at 8.5° N in the Indian Ocean. Near-inertial oscillations are regarded as a dominant source of ageostrophic noise, which is superimposed upon the Ekman flow, but zonal averaging or integration over several inertial periods should remove most of it. However, below the surface-intensified Ekman flow, the ageostrophic velocity along both sections shows wave-like structures of 50-80 m vertical scale with multiple maxima and minima. By applying a boxcar filter, these wave-like signals were separated from the cross-sectional ADCP velocity (Fig. 2.4). The appearance of these structures is mainly below the TTP and coincides with the layer of maximum buoyancy frequency. They are characterized by vertically alternating horizontal velocities with large horizontal coherence. *Chereskin and Roemmich* (1991) also reported the presence of such waves within the main thermocline, which were coherent over large horizontal space scales. These are thought to be near-inertial internal waves.

The section-averaged ageostrophic velocity had its maximum at the depth of the first valid bin of the ADCP (13-18 m), indicating that a shear existed within the ML, despite its homogeneous density. *Chereskin and Roemmich* (1991) examined this at 11° N in the Atlantic by zonally averaging a MLD-normalized ageostrophic velocity, and concluded that shear existed in the ML. However, *Wijffels et al.* (1994) applied the same technique and found a slab-like layer

of ageostrophic velocity above the MLD at 10° N in the Pacific and attributed the discrepancy to a loose definition of the MLD by *Chereskin and Roemmich* (1991). Following their methods, we also examined whether there was shear in the ageostrophic velocity within the ML along the two sections. It appears that at both sections, an ageostrophic shear existed in the ML, and this conclusion does not change if a more rigorous constraint on the MLD is used (Fig. 2.6).

The Ekman transport estimated by integrating the ageostrophic velocity zonally through the section and vertically to the local TTP depth is 6.2 ± 2.3 and -11.7 ± 2.1 Sv at 14.5° N and 11° S, respectively, which compares reasonably well to the estimates of 6.7 ± 3.5 and -13.6 ± 3.3 Sv by using the in-situ wind stress data. By using a fixed integration depth of 50 m at 14.5° N and 80 m at 11° S, the ageostrophic Ekman transport is not significantly different from those calculated using the TTP depth, while using the MLD as the integration depth, the ageostrophic Ekman transport is about one-fourth smaller than using the TTP depth. This is an indication that the wind-driven flow penetrates beyond the ML to the TTP, and it is consistent with the findings of *Wijffels et al.* (1994), who reported that at 10° N in the Pacific two-thirds of the wind-driven transport was within the ML and that the TTP is a reasonable choice for the integration depth of the Ekman flow. Note that above the first valid ADCP bin (13-18 m), the meridional ageostrophic velocity was linearly extrapolated using the values from the first two bins. However, when the surface meridional Ekman velocity is assumed equal to the velocity of the first valid ADCP bin (constant extrapolation), or extrapolated toward the theoretical Ekman solution for the surface velocity, the total ageostrophic transport would be up to 1.2 Sv smaller than the results shown above. Therefore, the linear extrapolation may to some extent overestimate the Ekman transport.

Between the two sections, the poleward Ekman transport divergence is 17.9 Sv, and the equatorward geostrophic convergence in the TTP layer is 6.2 Sv. This result agrees with the conclusion derived from theoretical consideration by *Schott et al.* (2004), who stated that the poleward Ekman divergence induced by the trade winds in both hemispheres is compensated by an equatorward convergence due to the geostrophic flow in the upper layer, but the compensation is generally assumed not to be strong enough to reverse the Ekman divergence.

Note that the Ekman volume transport and the Ekman divergence estimated above were obtained by using data sampled during two Atlantic transects. The time series of Ekman transport calculated from the 6-h NCEP/CFSr wind stress from 2000 to 2011 shows a clear seasonal cycle and interannual variability at both latitudes. The transport strength reaches its maximum in the winter months of the respective hemisphere, and its minimum in the summer

months of the respective hemisphere. The annual climatology with standard deviation from this time series is 7.9 ± 3.5 Sv at 14.5° N and -10.4 ± 3.3 Sv at 11° S. Our direct Ekman transport estimates agree well with the annual climatology. The uncertainties in the direct Ekman transport estimates are given by considering the aliasing effect of the near-inertial waves during the cruise. However, a larger uncertainty can be expected when the seasonal to interannual variability of the Ekman transport is taken into account.

The cumulative Ekman transport shows a rapid increase in the middle of the section and very little changes in the last quarter near the eastern boundary at both latitudes. This is because the zonal trade winds are generally strong and persistent in the western and middle parts of the basin, while relatively weak and unstable in strength and direction near the eastern boundary. Similar horizontal characteristics of Ekman transport were also seen at 11° N and 6° S in the Atlantic (*Chereskin and Roemmich*, 1991; *Garzoli and Molinari*, 2001) and 10° N in the Pacific (*Wijffels et al.*, 1994). The GECCO2 ocean state estimate daily data were also used to calculate the meridional Ekman transport at 14.5° N and 11° S in the Atlantic by using the direct approach, which agrees very well with the observed results in respect to horizontal transport structure throughout the basin and the total transport amount. This was mostly due to the fact that GECCO2 assimilates the observed wind, and with a daily temporal resolution, it is possible for GECCO2 to reproduce the strength of the in-situ wind, hence the Ekman transport. This good agreement has lent us more confidence in using GECCO2 as a reference in further studies on the MOC at the same latitudes.

An Ekman layer temperature and salinity must be assigned when calculating the Ekman heat and salt fluxes. Our results suggest that using the SST and SSS for the meridional Ekman heat and salt flux calculation at the two sections is only marginally different from calculations using the temperature and salinity in the TTP layer. It is rather the uncertainty in the Ekman volume transport estimates that dominates the uncertainties in the Ekman heat and salt fluxes. This is in good agreement with the finding at 10° N in the Pacific by *Wijffels et al.* (1994), while in striking contrast to that at 11° N in the Atlantic by *Chereskin and Roemmich* (1991), who found the transport-weighted Ekman temperature is 1 °C cooler than the surface value. The reason for such a contrast is not clear, but it is possible that in their case the TTP was much deeper than the MLD, especially in the western half of the basin.

Since Ekman volume, heat, and salt transport are significant upper layer components of the MOC with respect to the mass, heat and freshwater conservation, further studies on the vertical and horizontal structures of the Ekman flow, as well as on the Ekman heat and salt

fluxes, are expected to deepen our understanding and facilitate the studies on MOC strength and variability. This study would also provide some reference for the follow-up studies on the MOC at the same latitudes.

Acknowledgements

We thank Toste Tanhua for closing the M96 section towards the African coast during M97, as well as all the research teams and crews onboard R/V Meteor for their dedicated work during the three cruise legs. We thank Armin Köhl for providing the GECCO2 data and the information about the data. We also thank Richard Greatbatch for the comments on a previous version of the manuscript, and Gerd Krahmann for providing the matlab codes for uCTD sensor calibration. The blended level-4 wind stress data were provided by Copernicus Marine Environment Monitoring Service (CMEMS). This study is funded by the Deutsche Forschungsgemeinschaft as part of the cooperative project FOR1740 and by the German Federal Ministry of Education and Research as part of the cooperative projects RACE (03F0605B) and SACUS (03F0751A).

3 Atlantic meridional overturning circulation at 14.5° N and 24.5° N during 1989/1992 and 2013/2015: Volume, heat and freshwater fluxes

In this chapter, hydrographic data along 14.5° N measured in 1989 and 2013, and along 24.5° N measured in 1992 and 2015 were analysed. Through comparison between the realizations along the respective latitudes, the water masses in the tropical North Atlantic were identified, the property changes over the past two and half decades were observed. By applying the box inverse method to the data, full-depth meridional overturning transports across the two latitudes during 1989/1992 and 2013/2015 were determined. The comparison between the inverse solution, the GECCO2 ocean state estimate, the MOVE and RAPID array analysis data revealed consistencies but also discrepancies.

The manuscript was submitted to Ocean Science in Oct 2017, and is currently under review.

Citation: **Fu, Y., Karstensen, J. and Brandt, P.: Atlantic meridional overturning circulation at 14.5 N and 24.5 N during 1989/1992 and 2013/2015: volume, heat and freshwater fluxes, Ocean Sci. Discuss., doi:10.5194/os-2017-87, 2017.**

The candidate designed the study and analysed the ship-board and assimilation data. He performed the box inverse model and analysed the inverse solution. He produced all figures and authored the manuscript from the first draft to the submitted version.

Abstract

The Atlantic meridional overturning circulation (AMOC) is analysed using hydrographic data from trans-Atlantic sections along 14.5° N, occupied in 1989 and 2013, and along 24.5° N, occupied in 1992 and 2015. Comparison between the periods shows that the Antarctic Intermediate Water (AAIW) became warmer and saltier at 14.5° N, and the density of the densest Antarctic Bottom Water decreased at both sections. By applying a box inverse model, the absolute meridional velocity across the sections and dianeutral velocity across neutral surfaces were determined. Corresponding to the warming and salinification of the AAIW at 14.5° N, the intermediate layer transport was also considerably weaker in 2013 than in 1989. The AMOC was generally stronger during 1989/1992 than during 2013/2015 (18.6 ± 2.7 vs. 14.7 ± 3.9 Sv at 14.5° N, and 19.2 ± 1.7 vs. 16.9 ± 1.6 Sv at 24.5° N, respectively). The inverse solution suggests that the transport changes are caused by reduction in the northward thermocline and intermediate water transport, which is balanced by decrease in the southward upper North Atlantic Deep Water transport at both sections. The AMOC strength of the inverse solution agrees well with that of dynamically consistent and data-constrained ocean state estimate GECCO2 (15.8 ± 3.4 Sv at 14.5° N, and 17.7 ± 3.6 Sv at 24.5° N) and derived by the RAPID array data (16.9 ± 4.4 Sv), but is generally smaller than that derived by the MOVE array data (24.1 ± 4.1 Sv). Instead of any long-term trend, the GECCO2 shows strong seasonal to interannual variability of the AMOC at both latitudes, which may explain the observed changes of the AMOC in the box inverse model. Sensitivity tests of the inverse solution suggest that the overturning structure and heat flux across the 14.5° N section are sensitive to the Ekman transport, while freshwater flux is sensitive to the transport-weighted salinity at the western boundary.

3.1 Introduction

The Atlantic meridional overturning circulation plays an important role in the global climate. In the tropical and subtropical North Atlantic, it consists of the northward flowing surface, intermediate, and bottom waters, and the southward flowing NADW. The warm and shallow net northward flow carries a large amount of heat to the subpolar North Atlantic, where the heat is released to the atmosphere, resulting in the formation of NADW. The NADW then returns as a cold and deep southward flow mainly within the DWBC. The net heat flux from the tropics to the higher latitudes has large climate impact (*Wunsch*, 2005).

Since decades, oceanographers have continuously spent efforts investigating different aspects

of the AMOC. For instance, using the hydrographic section data obtained during the IGY, and the WOCE, many studies focused on estimating the volume transport, and heat and freshwater fluxes related to the AMOC (e.g. *Roemmich and Wunsch* 1985; *Macdonald* 1998; *Ganachaud and Wunsch* 2000; *Ganachaud* 2003; *Lumpkin and Speer* 2003). These pioneer studies revealed a consistent picture of the AMOC in terms of large-scale horizontal and overturning circulation. Recent studies based on end-point geostrophic mooring data (e.g. MOVE and RAPID array data), have shown that the AMOC exhibits variability on timescales from seasonal to decadal (*Cunningham et al.*, 2007; *Kanzow et al.*, 2008, 2010; *Smeed et al.*, 2014). At 26° N, different components of the AMOC have been analysed in details including the western boundary current (Florida Current, FC), the Ekman transport, and the interior geostrophic transport. Based on the RAPID array data, *Cunningham et al.* (2007) reported that on timescales from subseasonal to seasonal, the upper ocean has an immediate response to the change in the Ekman transport, while *Kanzow et al.* (2010) and *McCarthy et al.* (2012) have shown that on the seasonal to internannual timescales, the interior geostrophic transport plays a more important role in modulating the strength of the AMOC. Interestingly, studies based on the RAPID array at 26° N and on the MOVE array at 16° N often reveal contrary conclusions on the AMOC. For instance, RAPID-based estimates indicate that the AMOC decreased at a rate of -4.1 ± 3.2 Sv decade^{-1} between April 2004 and October 2013, while MOVE-based estimates indicate a strengthening trend of 8.4 ± 5.6 Sv decade^{-1} during the same period (*Baringer et al.*, 2015). *Smeed et al.* (2014) found that a strengthened southward thermocline water transport is responsible for the weakened AMOC at 26° N during 2004-2012, which was balanced by a decrease in the southward flow of the lower NADW. However, *Send et al.* (2011) found that changes in the LSW (as the primary component of the upper NADW) was responsible for the variability in the AMOC at 16° N.

A trans-Atlantic section nominally along 14.5° N was occupied twice in the past, in February, 1989, and in May-June, 2013 (Fig. 3.1). One of the unique feature of this section is that it lays roughly at the latitude of maximum annual mean northward meridional Ekman transport (about 8.3 Sv) in the tropical North Atlantic (*Fu et al.*, 2017). Therefore, it is expected that at this latitude, the meridional Ekman transport plays a more important role in the AMOC than at mid-latitudes, for instance, 26° N, especially in terms of meridional heat flux associated with the AMOC.

A classical method of estimating the AMOC is the application of a box inverse model to an oceanic box bounded by hydrographic sections and landmasses. By conserving the volume

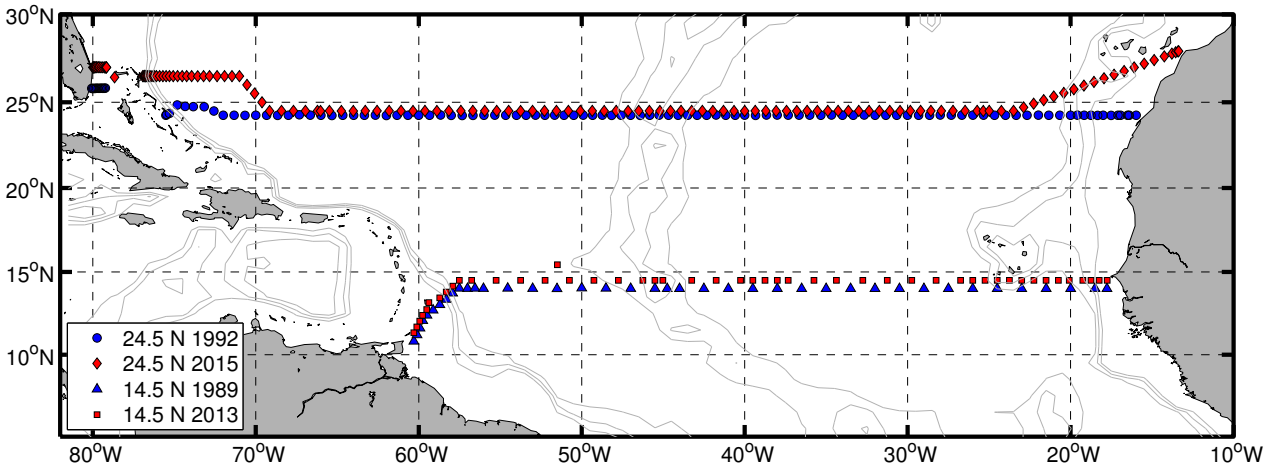

Figure. 3.1 | Geographic map showing the hydrographic sections occupied in 1992 and 2015 at 24.5° N and in 1989 and 2013 at 14.5° N. Note that only the stations with CTD profiles reaching the bottom are shown here, and that the cruise tracks at both sections are offset by 0.5 degree latitude for visual clarity.

(or mass) and other properties (e.g. heat and salt) in the whole box and layers, the absolute geostrophic velocity (thus the absolute transport) can be obtained (*Wunsch*, 1977, 1996). In this study, we apply a box inverse model to realizations of the 14.5° N (1989 and 2013) and 24.5° N (1992 and 2015) sections (Fig. 3.1). The results of the box inverse models for the two different periods will be presented and discussed. The 24.5° N section, aligned with the RAPID array, is one of the most frequently surveyed basin-wide zonal sections in the North Atlantic. Many aspects of the AMOC along 24.5° N, in terms of transport components, circulation patterns, and heat and freshwater fluxes, are well described, and provide reliable information on constraining a box inverse model (e.g. *Roemmich and Wunsch* 1985; *Ganachaud* 2003; *Lumpkin and Speer* 2003; *Atkinson et al.* 2012; *Hernández-Guerra et al.* 2014). Therefore, we chose this section in combination with the 14.5° N section for the box inverse model, which allow us to pay more attention to the less well studied features associated with the 14.5° N section.

Klein et al. (1995) calculated the meridional transport at 14.5° N from the 1989 realization by applying a box inverse model in combination with the 8° N section occupied in 1957. When compared to modern data (*Fu et al.*, 2017), *Klein et al.* (1995) used an extremely large annual and seasonal (winter) Ekman transport of 13.58 Sv and 15.94 Sv for the calculation, in contrast to an annual mean of 8.29±2.59 Sv calculated from the NCEP/CFSr monthly wind stress data. Besides, the large time difference between the occupations of the two sections (more than 30 years) could be problematic in the application of a box inverse model. As a result, the derived

transport of northward flowing water masses (e.g. Antarctic Intermediate Water, AAIW and Antartic Bottom Water, AABW) was surprisingly small. Therefore, it is also necessary to revisit the 1989 realization of 14.5° N in order to obtain a more reliable meridional overturning circulation for that year.

The paper is organized as follows: In section 3.2, the data used in this study are introduced; water mass distribution and property changes of the water masses between the two periods along the two latitudes are described. The details of the box inverse model and the calculation method for the heat and freshwater fluxes are given in section 3.3. The inverse model results are presented and discussed in section 3.4. A comparison between the inverse solutions, GECCO2 ocean state estimate, and the MOVE and RAPID array analysis data is presented in section 3.5. A conclusion is given as the final section.

3.2 Hydrographic data and water masses

3.2.1 Hydrographic sections at 14.5° N and 24.5° N

The first survey of the 14.5° N section was from 5 to 23 February 1989, and jointly completed by R/V Meteor (M09) and R/V Albatross IV, covering the eastern and western half of the section separated by the MAR (at about 42.5° W), respectively. At the western boundary, the cruise track of R/V Albatross was northeastward from 11.3° N/60.3° W to 14.5° N/ 57.5° W. It was necessary in order to complete the section perpendicular to the continental slope and to sample the western boundary currents (including the DWBC) there. During the cruise, CTD measurements were conducted. At the western boundary, all of the CTD profiles (westernmost 10 profiles) reached the bottom with an averaged horizontal spacing of 30 nm, for the rest of the section, the CTD depth alternated between the bottom and 2000 m with an averaged horizontal spacing of 45 nm. As a result, 39 CTD profiles in total reached the bottom for the entire section with a 1-m vertical resolution. The accuracy of the data set is expected to be ±0.002 °C for temperature, ±0.002 psu for salinity, and ±3 dbar for pressure, respectively (*Klein et al.*, 1995). The M09 CTD was also equipped with a Beckmann type polarographic oxygen sensor that measured the oxygen current (OC/A) and oxygen temperature (OT/°C). They were converted to dissolved oxygen concentration according to *Owens and Millard* (1985) and calibrated using the available bottle oxygen data. The final processed CTD oxygen data have an accuracy of ±10 μmol kg^{-1} (using a double root mean squared difference against bottle oxygen data). The R/V Albatross CTD oxygen sensor malfunctioned; only bottle oxygen data

were available. The processing details of the R/V Albatross and R/V Meteor CTD data have been described in *Wilburn et al.* (1990) and *Klein* (1992).

The second survey of the 14.5° N section was done in 2013 aboard R/V Meteor during the cruise M96 (28 April to 20 May 2013) and M97 (8 and 9 June 2013). The M96 leg covered the section from the coast of Trinidad and Tobago (11.3° N/60.3° W) to about 20° W, and the M97 leg covered from 20° W to the African coast (easternmost 4 stations). During the cruises, CTD measurements were performed on a grid similar to that of 1989. The westernmost part of the section (10 stations) was perpendicular to the coast and all profiles reached the bottom; for the rest of the section, CTD depth alternated between the bottom and 3000 m. In total 64 CTD stations were occupied along the 14.5° N section with a nominal resolution of 40 nm, and 48 profiles reached the bottom with a 1-m vertical resolution. The CTD work was carried out using a Sea-Bird Electronic (SBE) 9 plus system with double sensor packages for temperature, conductivity and oxygen. The accuracy of the temperature sensors is ±0.001 °C; after calibration by comparing the bottle stop salinity and oxygen with the measurements of salinometer and oxygen titration of bottle samples, the accuracy of salinity and oxygen sensors is ±0.002 psu and ±1.3 μmol kg^{-1}, respectively. Different from the 1989 occupation, the 2013 occupation also included direct velocity observations. During the M96 leg, two 300 kHz Teledyne RDI lowered ADCP (LADCP) were mounted to the CTD-Rosette for most of the stations, except for stations between 38° W and 33.5° W, where the large water depth (> 6000 m) prevented the use of the LADCPs. During the M97 leg, no LADCP system was installed. The LADCP data was post-processed with the GEOMAR processing routine v10.4 (*Fischer and Visbeck*, 1993; *Visbeck*, 2002). Additionally, two vessel-mounted Teledyne RDI ADCP (SADCP) were in operation at frequency of 38 kHz and 75 kHz. They are equipped with phased array transducers and can measure up to 1200 m and 800 m depth, respectively. Ship navigation information was synchronized with the system. Misalignment angles and amplitude factors were calibrated during the post processing. The uncertainties of 1-hour averages of the underway measurement is expected to be 2-4 cm s^{-1} (*Fischer et al.*, 2003).

At 24.5° N, the CTD section has been repeated several times (*Atkinson et al.*, 2012). In this study, we chose data measured during cruises from 14 July to 15 August 1992, and from 10 December 2015 to 20 January 2016 to combine with the 14.5° N section measured in 1989 and 2013, respectively (Fig. 3.1). The CTD data were provided through the CLIVAR and Carbon Hydrographic Data Office (CCHDO). All the profiles reached tens of meters above the ocean bottom with a 2-m vertical resolution. The distance between the adjacent CTD stations was

typically 25 to 30 nm. When surveying across boundary currents and continental slopes, the distance was reduced to resolve the boundary current structure. Within the Florida Straits, 11 profiles were collected as part of the 1992 section. During the 2015 occupation, Florida Straits was surveyed twice, but only profiles collected during the first survey were used in this study due to the higher spatial sampling resolution.

3.2.2 Water mass distribution and property changes

The water mass properties at 14.5° N have been introduced by *Molinari et al.* (1992) and *Klein et al.* (1995) based on the 1989 realization. At 24.5° N, the water mass properties have been described several times (e.g. *Roemmich and Wunsch* 1985; *Hernández-Guerra et al.* 2014). Here we briefly describe the water mass properties, and emphasize the differences between the former and latter periods at each section. The potential temperature (θ) and salinity (S) diagram drawn using data at the two sections provides an overview of the distribution of water masses (Fig. 3.2). The vertical sections of salinity, potential temperature, oxygen (O), and neutral density (γ_n), are presented for the different years at each section in Fig. 3.3-3.6.

As described in the previous section, at 14.5° N, except in the western boundary region, the CTD depth alternates between 2000 m (3000 m) and the ocean bottom for the measurement in 1989 (2013). For a better visual effect, a Gaussian weighting function with horizontal influence and cut-off radii of 0.5 and 1.5 degree in longitude, vertical influence and cut-off radii of 20 and 40 m were applied to interpolate and smooth the data. The horizontal and vertical resolution of the mapping was chosen as 0.25 degree and 20 m. At 24.5° N, no interpolation and smoothing are needed due to the high horizontal resolution. The difference of S and θ between the two time periods for each section is also shown to facilitate the discussion (Fig. 3.3c and 3.4c). To calculate the difference, the original S and θ were firstly transformed from pressure levels to uniform γ_n levels, then they were horizontally interpolated on each γ_n level onto a consistent horizontal grid; finally, the differences of S and θ were calculated between the two time periods, and transformed back to pressure level and smoothed using a Gaussian weighting function as described above.

At 14.5° N, only bottle oxygen data are available in the western half of the basin for the 1989 dataset (the Albatross IV leg). To obtain an oxygen section on the same regular grid, the bottle oxygen, θ and S data were used to derive oxygen as a function of θ and S in the θ/S space. Here a Gaussian interpolation function was applied to achieve a general functional relationship that finally allowed obtaining an oxygen distribution from the θ and S distribution

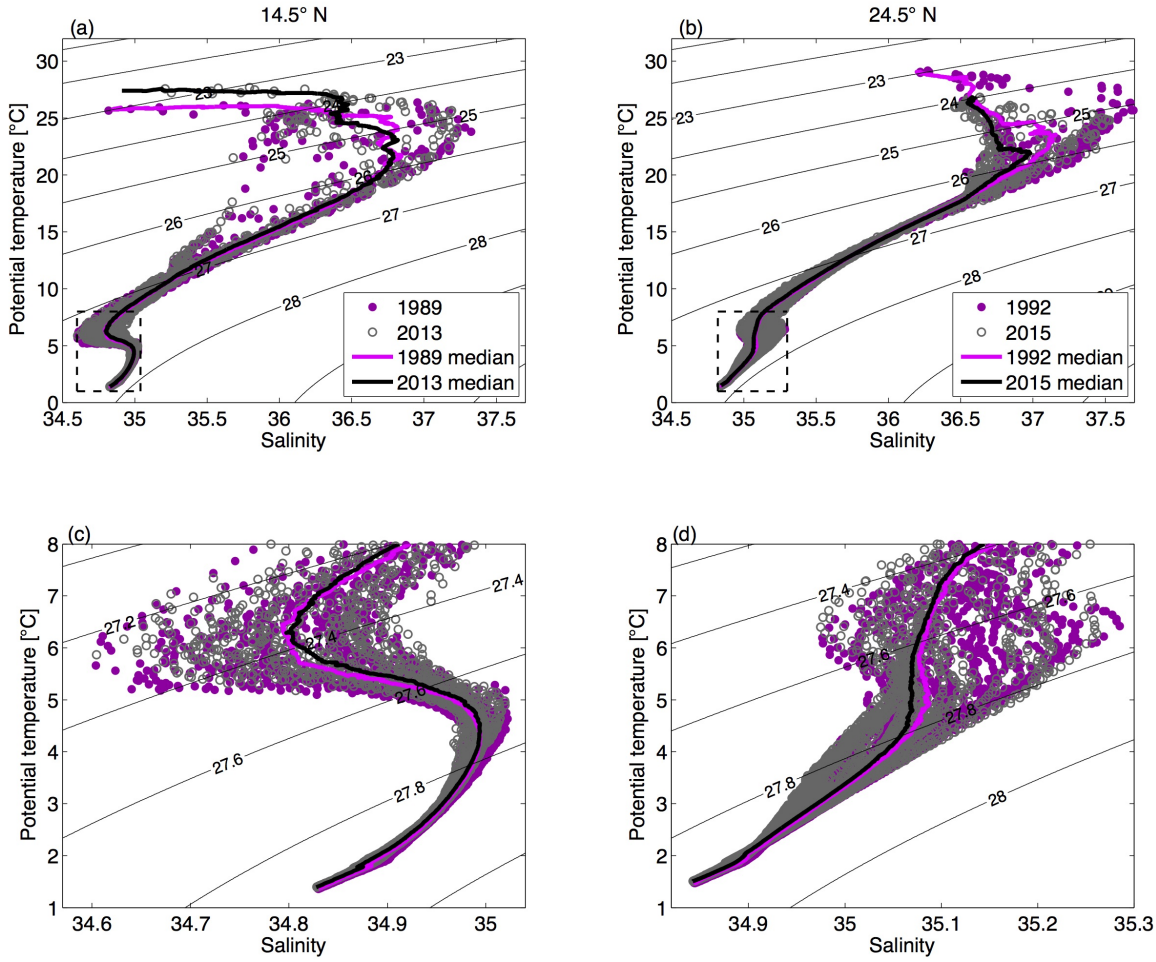

Figure. 3.2 | The θ/S diagram at 14.5° N (a, c) in 1989 (dark violet solid circles) and 2013 (grey open circles), and at 24.5° N (b, d) in 1992 (dark violet solid circles) and 2015 (grey open circles). The median θ/S profiles, calculated on common neutral density grids, are shown in black for the earlier realizations at the respective sections and in light violet for the more recent realizations (cf. legend in a and b). The lower panel is the zoom of the area within the black dashed box in the corresponding upper panel. Note that the data are subsampled for visual clarity as every other profile horizontally and every 20 m vertically.

along the section. To further correct for local variations that may not have been correctly represented by the functional relationship, we calculated an oxygen anomaly as the difference between derived oxygen and bottle oxygen data. The oxygen anomaly was interpolated onto the grid of the section and finally subtracted from the derived oxygen field. In this way, both general and local relations of the oxygen to the water masses were taken into account. The remaining eastern part of the 1989 oxygen section is directly from the CTD Beckman type oxygen sensor (cf. Sect. 3.2.1).

The water mass distribution can be inferred from the θ/S diagram (Fig. 3.2). At 14.5° N, proceeding from the surface, the long tail with homogeneous temperatures above 25 °C represents the surface water mainly in the mixed layer. The different temperature levels (with

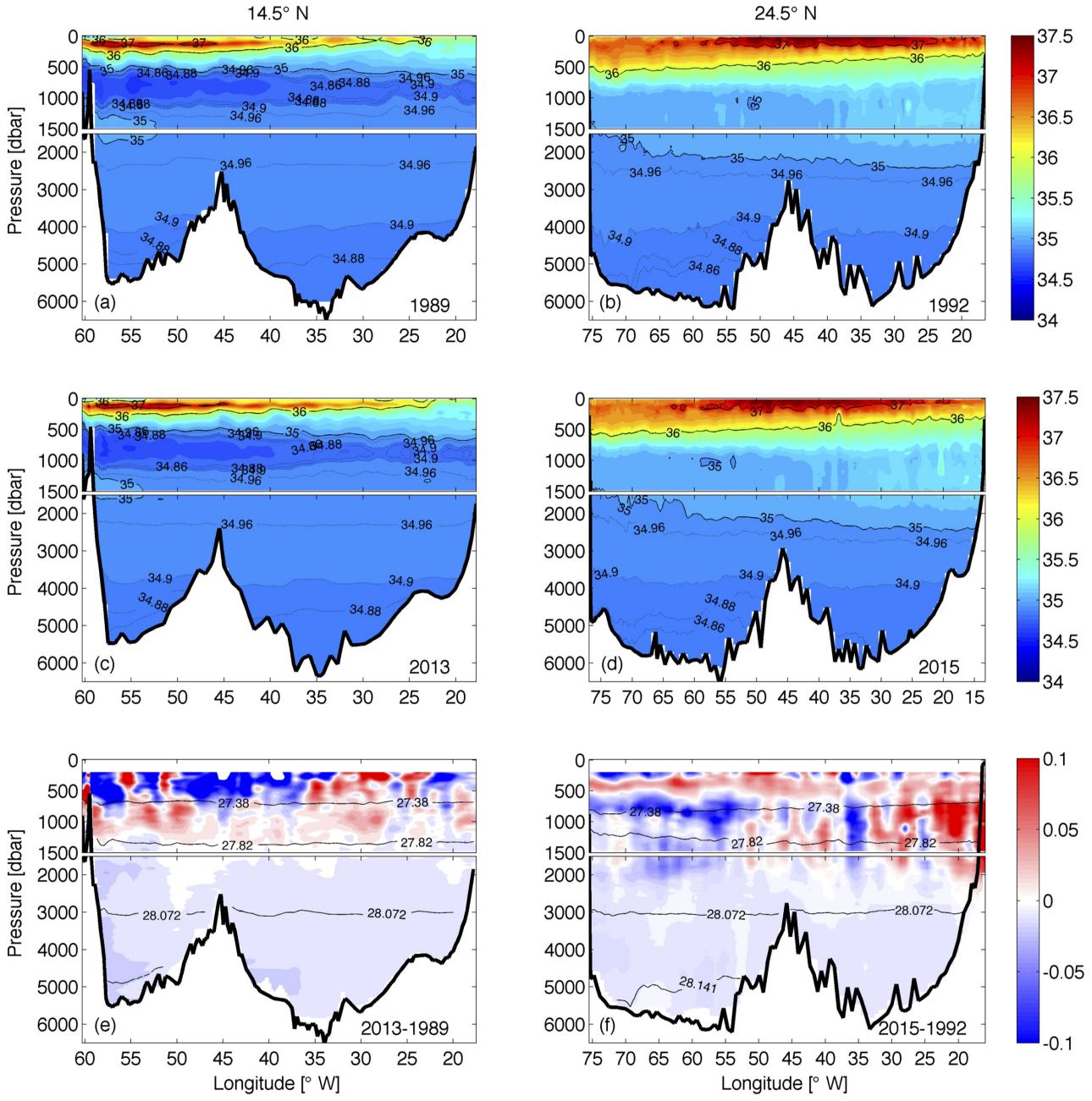

Figure. 3.3 | Vertical sections of salinity at 14.5° N in (a) 1989 and (c) 2013; and at 24.5° N in (b) 1992 and (d) 2015. Further shown is the salinity difference at (e) 14.5° N between 2013 and 1989, and (f) 24.5° N between 2015 and 1992. Note that the difference is calculated first on neutral density levels, then transformed back onto depth levels, and that the upper 200 m are neglected. The contours in (e) and (f) are the neutral density surfaces of 27.38, 27.82, 28.072, and 28.141 kg m^{-3}, which marks the boundaries of AAIW, UNADW, LNADW, and AABW. The upper 1500 m in each subplot are stretched.

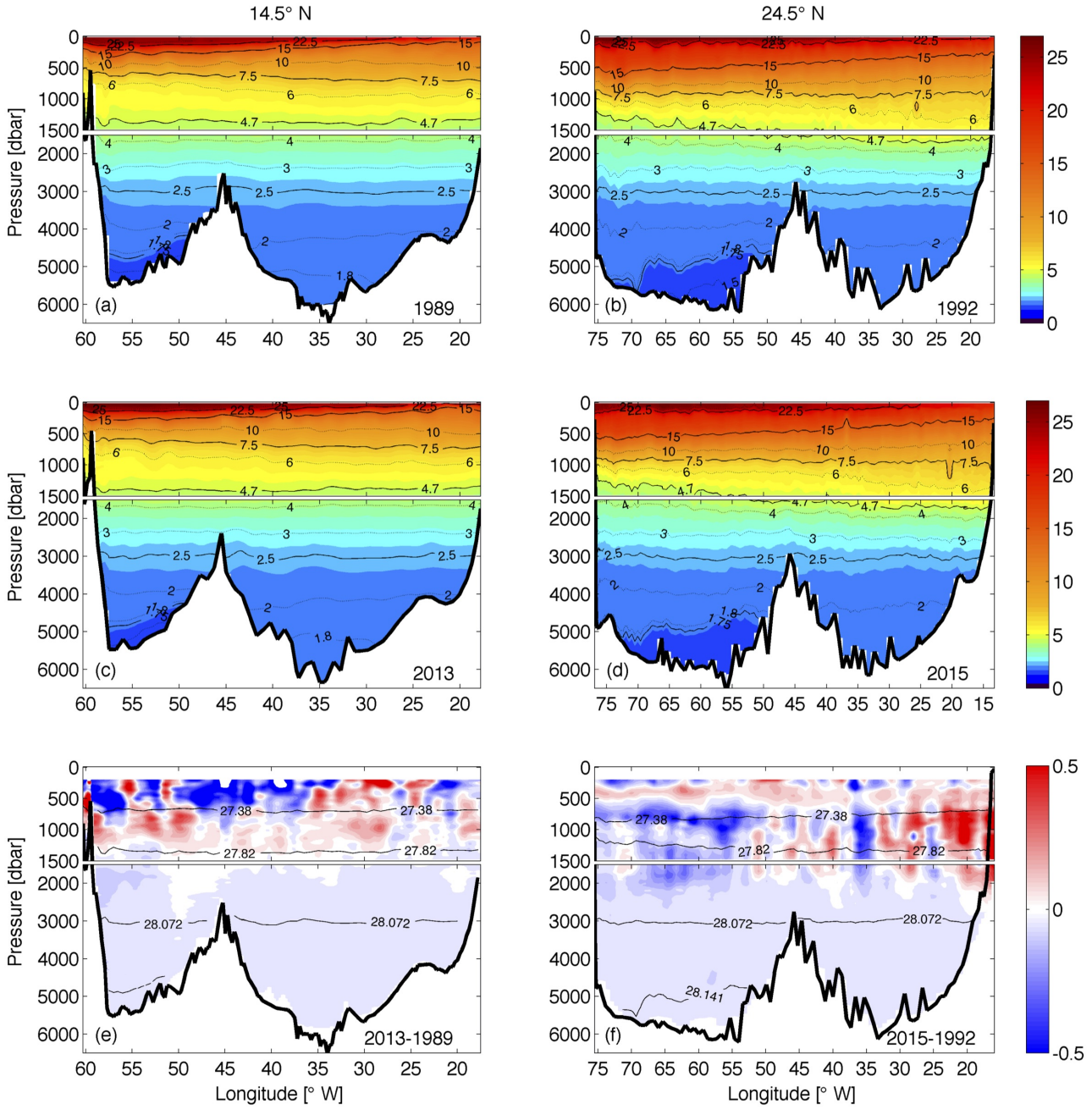

Figure. 3.4 | Vertical sections of potential temperature (°C) at 14.5° N in (a) 1989 and (c) 2013; and at 24.5° N in (b) 1992, (d) 2015. Further shown is the potential temperature difference at (e) 14.5° N between 2013 and 1989; and (f) 24.5° N between 2015 and 1992. Note that the difference is calculated first on neutral density levels, then transformed back to depth levels, and that the upper 200 m are neglected. The contours in (e) and (f) are the neutral density surfaces of 27.38, 27.82, 28.072, and 28.141 kg m^{-3}, which marks the boundaries of AAIW, UNADW, LNADW, and AABW. The upper 1500 m in each subplot are stretched.

a mean offset of 1.60 °C in the upper 50 m) are most likely caused by the different seasons when the occupations took place (February 1989 and May 2013, respectively). Slightly below the surface water, a salinity maximum at about 24 °C marks the STUW, corresponding to the subsurface layer centred at about 120 m in Fig. 3.3a and c. This water mass originates from the subtropical Atlantic, where evaporation exceeds precipitation, forming sea surface salinity (SSS) maxima at about 25° N in the North Atlantic (as shown in Fig. 3.3b and d at 24.5° N) and about 20° S in the South Atlantic. The SSS maxima are further subducted and transported equatorward and westward as part of the subtropical cells (*McCreary and Lu*, 1994; *Schott et al.*, 2004). The median θ/S diagram calculated on neutral density surfaces at 14.5° N shows two salinity maxima between 22 and 25 °C (Fig. 3.2a), indicating the presence of northern and southern origin of these water masses (*Klein et al.*, 1995).

Within the temperature range from 20 to 8 °C, the majority of water has a nearly linear θ/S relationship for both sections (Fig. 3.2) that is a characteristic of CW. CWs compose the main thermocline and are formed by subduction in the subtropical gyre. As a result of subtropical gyre circulation, CWs occupy a larger depth range in the west than in the east, which can be seen from the upward tilting of the isotherms toward east (Fig. 3.4a to d). Within the temperature range between 13 and 18 °C, a deviation from the linear θ/S relation is found at the 14.5° N section from profiles sampled east of 22° W, where the Cape Verde Frontal Zone (CVFZ) is located. East of the CVFZ, signatures from SACW are seen, which is less saline than NACW. The SACW takes routes along and parallel to the equator following, after crossing the equator in the western equatorial Atlantic, the different eastward jets of the tropical North Atlantic. When approaching the West African coast, it spreads further northward from where it diffuses into the eastern tropical North Atlantic (*Kirchner et al.*, 2009; *Brandt et al.*, 2015). The CW layer at 24.5° N consists primarily of NACW.

At 14.5° N, the CW layer is characterized by low dissolved oxygen (DO) concentration down to 40 μmol kg^{-1} at its core (Fig. 3.5a, c). This layer is within the Oxygen Minimum Zone (OMZ) in the eastern tropical North Atlantic, which is formed generally due to weak ventilation and oxygen consumption (*Luyten et al.*, 1983; *Brandt et al.*, 2015). Comparing the OMZ between 2013 and 1989, it shows that the thickness of the minimum oxygen core (DO$<$ 60 μmol kg^{-1}) increased, while the westward extent of this core reduced. Such changes created a complicated pattern of the DO difference between 2013 and 1989 (not shown). First of all, the vertical expansion of the minimum oxygen levels are in agreement with the findings by *Stramma et al.* (2010), and created a local decrease of DO below the near-surface layer down

to 500 m along the eastern boundary (west of 22° W). On the other hand, the reduction of its zonal extent led to an increase of DO to the east of the core position in 2013, indicating that the oxygen decrease is not spatially coherent with local processes, and/or that processes on shorter timescales might affect the oxygen evolution.

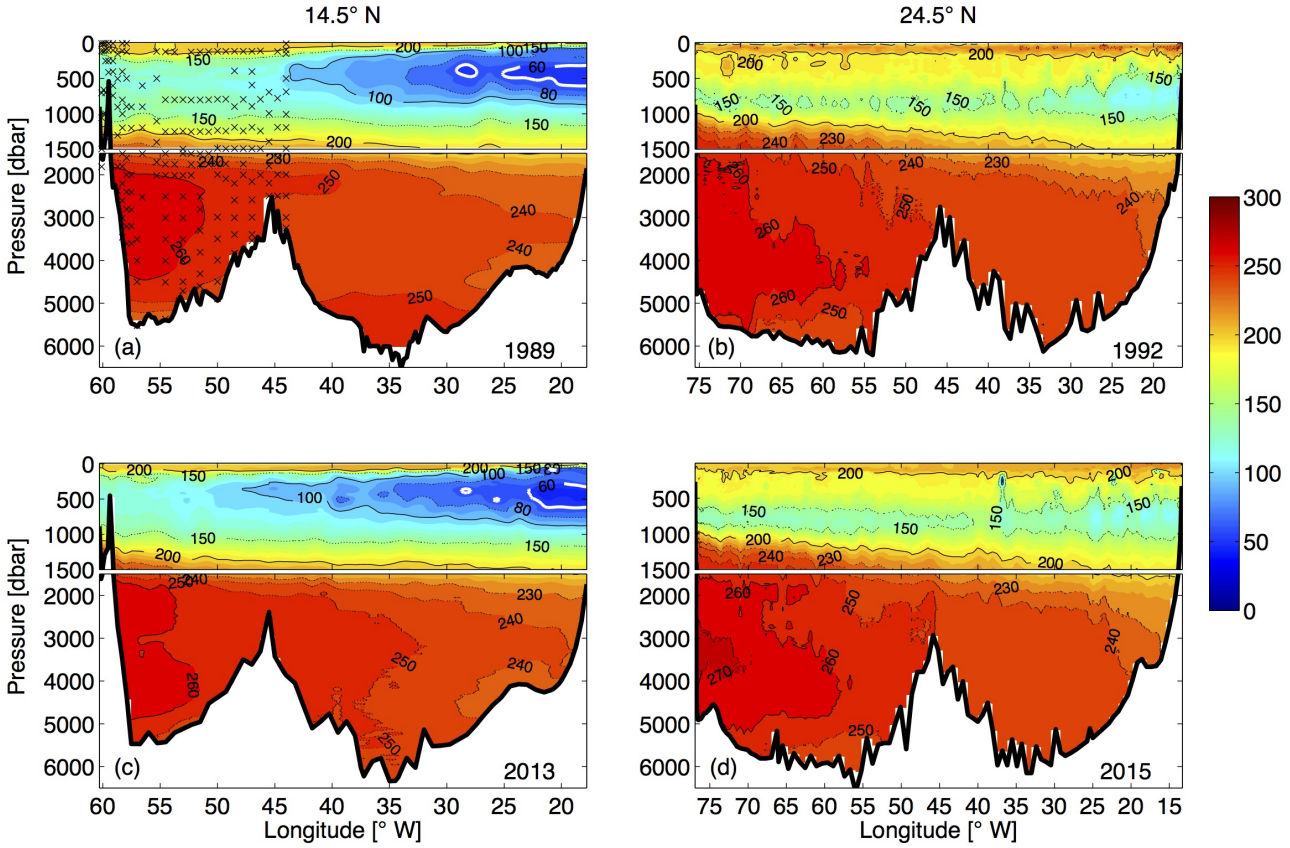

Figure. 3.5 | Vertical sections of oxygen (μmol kg^{-1}) at 14.5° N in (a) 1989 and (c) 2013; and at 24.5° N in (b) 1992 and (d) 2015. The "crosses" in (a) marks the position of bottle oxygen data, which are used to reconstruct the oxygen section in the western basin (see text for details). The white contour in (a) and (c) marks the 60 μmol kg^{-1} dissolved oxygen. The upper 1500 m in each subplot are stretched.

Directly below the CW is the intermediate water layer. At 14.5° N this layer consists predominantly of AAIW, while at 24.5° N AAIW and Mediterranean Water (MW) are both main contributors to this layer. AAIW is characterized by its salinity minimum centred at around 900 m (Fig. 3.3a, c), while MW is warmer and much saltier. The AAIW in the North Atlantic originates from the circumpolar South Atlantic, and is transported northward mainly along the western boundary (*Tsuchiya*, 1989). As a consequence of mixing with the surrounding waters on the way toward the north, AAIW gradually loses its salinity minimum signature in the northern hemisphere from the tropics to the subtropics. This can also be seen when comparing the 14.5° N and 24.5° N sections (Fig. 3.3a to d).

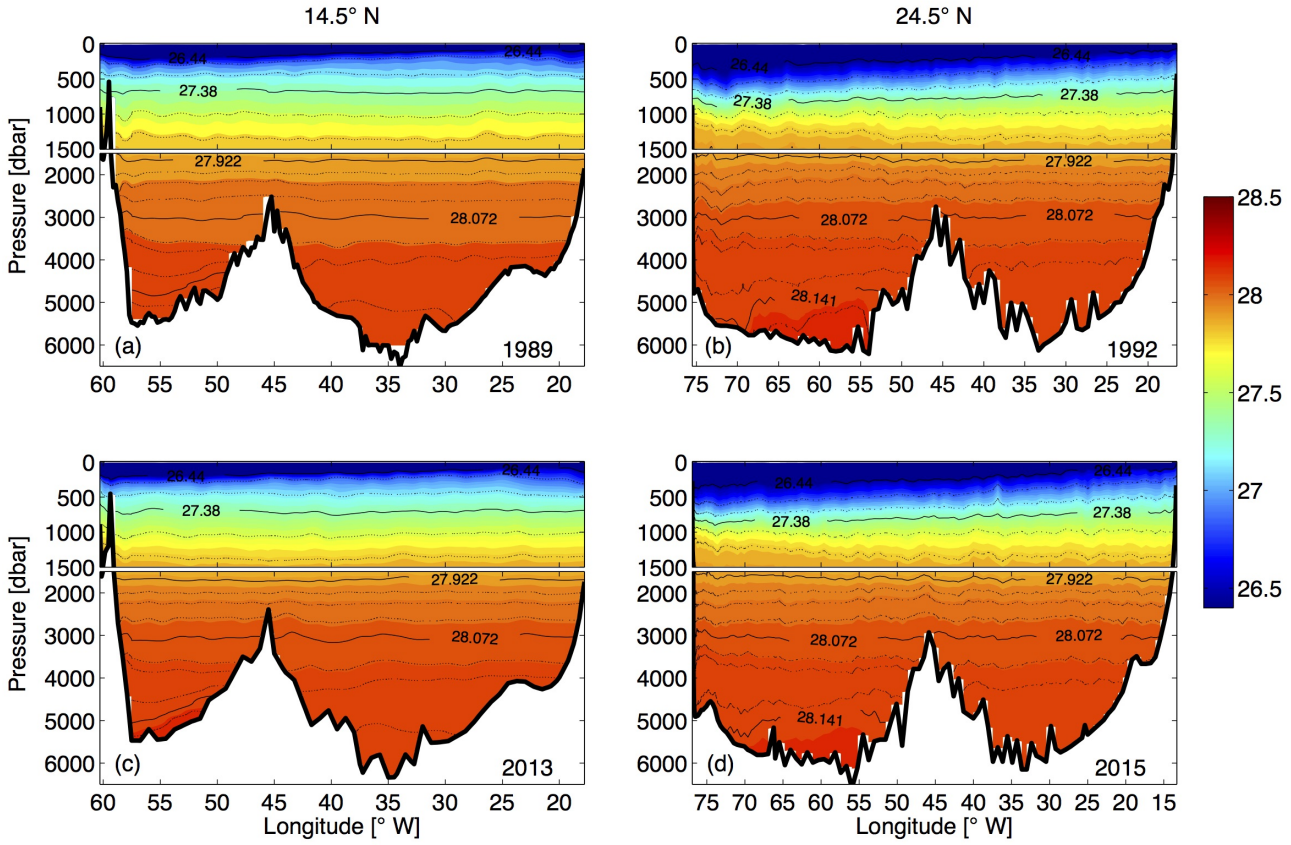

Figure. 3.6 | Vertical sections of neutral density (kg m^{-3}) at 14.5° N in (a) 1989 and (c) 2013; and at 24.5° N in (b) 1992 and (d) 2015. The upper 1500 m in each subplot are stretched.

From the θ/S diagram (Fig. 3.2a, c) and the vertical sections (Fig. 3.3e and 3.4e), it can be seen that the AAIW at 14.5° N became saltier and warmer between 1989 and 2013. This result is consistent with the previous studies on AAIW by *Sarafanov et al.* (2008), who found a significant warming of AAIW at 6.5° N between 1993 and 2000. *Schmidtko and Johnson* (2012) reported a warming and salinification trend in the AAIW core since 1970s throughout the tropical North Atlantic. They have attributed the cause of the warming trend to higher sea surface temperature in the AAIW formation region in the background of global warming, and to a strengthened Agulhas leakage associated with a low SAM during some periods of the 20th century. At 24.5° N, between 2015 and 1992, the waters in the intermediate layer are generally cooler and fresher in the western half of the section, while warmer and saltier in the eastern half of the section (Fig. 3.3f and 3.4f). Since the intermediate water at 24.5° N is composed of both AAIW and MW, the property change over time could be considered as an imprint of changing relative contributions of AAIW and MW along the section. On the basin scale, a strengthening of the gyre scale circulation would bring more AAIW on the western side from the tropics, while also more MW on the eastern side from the north, which would create a pattern like the

one we observed. Locally, for instance along the eastern margin, higher salinity in the 2015 realization than in the 1992 realization may reflect a seasonal intrusion of the less saline water near the African coast (*Roemmich and Wunsch*, 1985; *Hernández-Guerra et al.*, 2005). MW has been reported to occupy a greater portion of the eastern boundary during late winter and early spring, while AAIW contributes more in late fall and early winter (*Hernández-Guerra et al.*, 2003; *Fraile-Nuez et al.*, 2010). *Machín and Pelegrí* (2009); *Machín et al.* (2010) explained the seasonally varying contribution of the AAIW and MW with the stretching and shrinking of the intermediate water strata. Mediterranean eddies appeared at 24.5° N in both realizations and caused the maximum salinity values at about 7 °C in the θ/S diagram (Fig. 3.2b).

The NADW originates from the subpolar North Atlantic and is found at both sections (14.5° N and 24.5° N) in the γ_n ranges of 27.922-28.1295 kg m^{-3}. According to its formation region and the corresponding density ranges, NADW can be divided into UNADW, which is composed primarily of water formed in the Labrador Sea (LSW) (*Talley and McCartney*, 1982), and LNADW, originating from water masses formed in the Nordic Sea (*Pickart*, 1992; *Smethie et al.*, 2000), namely ISOW and DSOW. At both sections, a sharp isoneutral (surface of the same neutral density) slope in the NADW layers at the western boundary is indicative of the DWBC and its recirculation. The DWBC is a continuous feature between 24.5° N and 14.5° N, which is evident from the elevated oxygen concentration (DO$>$ 260 μmol kg^{-1}) along the continental slope at the western boundary (Fig. 3.5) due to a more recent contact with the atmosphere compared with surrounding waters in a similar density range. A dual-core structure of high oxygen at the western boundary is captured at 14.5° N in 2013, resulting from the ISOW with relatively low oxygen laying between the oxygen-rich LSW and DSOW. At 24.5° N, even higher oxygen concentration (DO$>$ 270 μmol kg^{-1}) is found in the DWBC region centred at about 3300 m in 2015, indicating the presence of more recently ventilated contributions to the LNADW. Throughout the NADW layers, the water became fresher and cooler on neutral density surfaces at both sections. The freshening is in agreement with previous studies showing that the NADWs in the formation region has been freshening since decades (*Dickson et al.*, 2002).

Isotherm and isohaline surfaces do not continue from the western into the eastern Atlantic across the MAR below 3500 m at both latitudes. Lower temperature and salinity but higher density is found in the western basin (west of the MAR) due to the influence of less saline and colder but also denser AABW (e.g. *Klein et al.* 1995). AABW is the densest water in the world oceans and is present at both sections primarily in the western basin with γ_n larger

than 28.1250 kg m^{-3} and θ lower than 1.80 °C. The MAR, as a topographic barrier, prevents AABW flowing directly into the eastern Atlantic basin, except at the Romanche Fracture Zone near the Equator and the Vema Fracture Zone at 11° N (*Wüst*, 1935; *McCartney et al.*, 1991). *Klein et al.* (1995) reported that the lowest salinity and temperature in the eastern basin found at 14.5° N was lower than that found at either 16° N and 8° N, indicating that a pathway for AABW crossing the MAR existed between 8° N and 14.5° N. It is believed that AABW gets warmer and saltier on its way to the north due to mixing with the overlying LNADW, therefore, it is not surprising that the densest AABW is warmer and saltier at 24.5° N than at 14.5° N.

It appears that at both latitudes, the AABW became cooler and fresher between the two periods (Fig. 3.3e, f and 3.4e, f). Note that we have calculated the changes on neutral surfaces, if the difference is calculated on pressure surfaces, it presents a different and complex picture. For example, at 14.5° N, the pressure-based difference shows that the AABW became warmer and salter west of 55° W, while cooler and fresher east of 55° W. At 24.5° N, the pressure-based difference shows that the AABW became mostly warmer but fresher, which is consistent with the previously observed warming of AABW at 24.5° N by *Johnson et al.* (2008), who also calculated the changes on pressure surfaces. At the same time, we noticed that the density of densest AABW observed at 14.5° N reduced from 28.1686 kg m^{-3} in 1989 to 28.1623 kg m^{-3} in 2013, and at 24.5° N from 28.1596 kg m^{-3} in 1992 to 28.154 kg m^{-3} in 2015. As a result, we believe that the warming of the AABW at 14.5° N and 24.5° N should not arise from property changes on the density surface, but should be due to depletion of the densest AABW core ($\gamma_n > 28.154$ kg m^{-3}) at both latitudes. This agrees with *Herrford et al.* (2017), who showed that in the equatorial South Atlantic, the coldest AABW became warmer since the early 1990s.

3.3 Methods

3.3.1 Inverse model setup

The box inverse method was applied to determine the meridional overturning transport across the 14.5° N and 24.5° N sections. Two boxes bounded by the ocean boundaries and the hydrographic sections measured in 1989/1992 (1989/1992 box) and 2013/2015 (2013/2015 box), respectively, can be built. Based on the thermal wind relation, the vertical shear of the geostrophic velocity relative to an arbitrary reference depth can be calculated from the density field between adjacent CTD stations. To obtain the absolute geostrophic velocity, a reference velocity must

be assigned to the shear at the reference level. A box inverse model is composed of equations that employ the thermal wind relation and conservation of properties (i.e. volume, salt, heat, Eq. 3.1). It adjusts the reference geostrophic velocity and vertical fluxes of properties from prior (initial) estimates to conserve the properties within the whole box and each layer of the box.

Following *Ganachaud* (2003) and *Hernández-Guerra et al.* (2014), we separated the two boxes into 17 vertical layers by neutral density surfaces specified according to the characteristics of water masses (Table 3.1). In this study, we applied the conservation of volume, salt anomaly, and heat at each layer and the whole box. The salt anomaly was calculated by subtracting a section-areal mean salinity from the salinity values. The conservation equation of a property C in a layer can be formulated in the general form

$$\sum_{j=1}^{J} \Delta x_j \int_{h_m}^{h_{m+1}} (v_j + b_j) C_j dz + [-w_m^C A_m C_m + w_{m+1}^C A_{m+1} C_{m+1}] \approx 0, \tag{3.1}$$

where j and m are indices for station pairs and layer interfaces, respectively; J is the total number of station pairs; Δx_j represents the horizontal distance between station pair j; h_m refers to the depth of layer interface m; v_j and b_j are the relative and reference geostrophic velocities at station pair j, respectively; C_j and C_m are the property concentration at station pair j and interface m, respectively; w^C is the dianeutral velocity of property C at the layer interfaces; A refers to the horizontal area of the layer interfaces within the boxes. Eq. 3.1 states that the total change of property C in one layer due to horizontal advections through the side boundaries and vertical fluxes through the upper and lower boundaries is approximately 0. Note that we define a dianeutral velocity for each property including the volume, salt anomaly, and heat. This has been proven to be an effective way of parametrizing the net dianeutral fluxes in inverse models (*McIntosh and Rintoul*, 1997; *Sloyan and Rintoul*, 2001; *Tsubouchi et al.*, 2012).

Except b and w, all other quantities in Eq. 3.1 are either known, or can be directly estimated from the hydrographic and topographic data. Note that for both realizations at 14.5° N, only profiles approaching to the bottom were used to construct the box inverse model (see Sect. 3.2.1 for details). For the 1989/1992 box, there are 149 CTD station pairs, the adjustment to the reference velocity at each station pair is treated as an unknown; the dianeutral velocity for each property across each layer interface is treated as an unknown, which adds 51 unknowns to the system. For the 2013/2015 box, there are 228 unknowns in total, including the adjustment to the reference velocity of 177 CTD station pairs and 51 dianeutral velocities.

Table. 3.1 | Neutral density surfaces (γ_n, kg m^{-3}) that separate the layers in the box inverse model. The water masses are labelled to the approximately corresponding layers.

Layer	Lower interface (γ_n, kgm^{-3})	Water mass
1	26.44	Surface water
2	26.85	
3	27.162	SACW/NACW
4	27.38	
5	27.62	
6	27.82	AAIW/MW
7	27.922	
8	27.975	
9	28.008	
10	28.044	UNADW
11	28.072	
12	28.0986	
13	28.11	LNADW
14	28.1295	
15	28.141	
16	28.154	AABW
17	bottom	

3.3.2 Constraints

To seek solutions for the unknowns b and w, other transport constraints at specific locations and depths can be applied in addition to the conservation equations of the properties in each layer and the whole box (Eq. 3.1). The details of the additional constraints are described here and summarized in Table 2. At 24.5° N, following *Hernández-Guerra et al.* (2014), we assumed a DWBC transport of -26.5 ± 13.5 Sv. The uncertainty range is given by half of the DWBC transport, when the large uncertainty in the different estimates based on moored observations is taken into account (*Bryden et al.*, 2005b; *Johns et al.*, 2008; *Meinen et al.*, 2013). This value was then applied to both time periods as the a priori constraint of the DWBC at 24.5° N between layer 7 and 14, 77° W and 72° W.

Table. 3.2 | Constraints for the box inverse model and the final adjusted transport after inversion. Note that the box inverse model does not adjust the meridional Ekman transport, which is prescribed using the annual zonal wind stress during the calendar year of the cruise. The unit of the transport is Sv. Southward transport is given with "-".

			1989/1992		2013/2015	
	Position	Layers	Constraints	Final	Constraints	Final
24.5° N						
Ekman transport	Full section	1	4.5	-	4.6	-
Florida Current	Florida strait	All	31.3 ± 1.1	31.2 ± 0.3	31.7 ± 1.1	31.8 ± 0.9
Bering strait	Full section	All	-0.8 ± 0.6	-0.9 ± 6.3	-0.8 ± 0.6	-0.8 ± 6.6
DWBC	77:72° W	7:14	-26.5 ± 13.6	-26.8 ± 4.6	-26.5 ± 13.6	-25.4 ± 4.1
14.5° N						
Ekman transport	Full section	1	8.8	-	8.3	-
Bering strait	Full section	All	-0.5 ± 0.6	-0.5 ± 7.8	-0.5 ± 0.6	-0.6 ± 8.3
Intermediate Water	Full section	4:6	Not applied	4.2 ± 2.2	2.8 ± 2.1	2.6 ± 1.7

A continuous time series of the FC transport has been constructed by using a succession of the submerged telephone cables across the Florida Straits between 26° N and 27° N (*Baringer and Larsen*, 2001; *Meinen et al.*, 2010). In this study, the FC transport was constrained using the annual mean value of 31.3 ± 1.1 Sv in 1992 and 31.7 ± 1.1 in 2015, calculated from the daily FC transport data. The uncertainties were given by the standard deviation of the annual mean FC transport between 1982 and 2016 estimated using the daily data. Note that both values are not significantly different from a long-term mean FC transport of 31.1 ± 2.4 Sv (adopted from *Atkinson et al.* 2010). Using the long-term mean value as the constraint for both boxes

would only alter the final solutions marginally.

The surface freshwater flux was constrained as 0.34±0.28 Sv for both boxes (positive denotes freshwater loss of the ocean). This value was estimated using the mean and standard deviation of the monthly freshwater flux from the Hamburg Ocean Atmosphere Parameters and Fluxes from Satellite 3.3 (HOAPS-3.3) dataset between 1989 and 2013 (*Kinzel et al.*, 2016).

About 0.8 ± 0.6 Sv water flows from the Pacific to the Atlantic through the Bering Strait (*Roach et al.*, 1995; *Woodgate et al.*, 2005). In previous inverse studies involving two zonal trans-Atlantic sections, the Bering Strait transport was often regarded as a net southward barotropic flux through both sections with equal amount of volume (*Hernández-Guerra et al.*, 2014). However, as a result, the surface freshwater flux between the atmosphere and ocean would be inevitably ignored. As described above, we have explicitly constrained the surface freshwater flux; therefore, it is reasonable to assume different net Bering Strait transport at the two sections. In this study, we constrained the Bering Strait transport through the 24.5° N section still as 0.8 ± 0.6 Sv, but 0.5 ± 0.6 Sv through 14.5° N in both boxes to account for the net surface flux to the atmosphere between the two sections.

At 14.5° N, an additional constraint on the AAIW transport of 2.8 ± 2.1 Sv for the 2013 realization was applied. We found that without this additional constraint, the final AAIW transport for the 2013 realization after the inversion would be southward, regardless what reference level or whether an a prior reference velocity based on the ADCP measurement was applied. This is contrary to the expected AAIW flow direction. Therefore, we constrained this quantity based on the annual mean AAIW transport from the monthly data of the dynamically consistent and data-constrained ocean state estimate GECCO2 (*Wunsch and Heimbach*, 2006; *Köhl*, 2015) at 14.5° N in 2013. The uncertainty was given by the standard deviation of the monthly AAIW transport in GECCO2 at 14.5° N between 1985 and 2015. The AAIW in GECCO2 is defined using the same neutral density range ($27.38 < \gamma_n < 27.82$ kg m^{-3}) as for the observed hydrographic data.

The Ekman transport in the box inverse model is prescribed in the first layer of each section, which is estimated using the monthly wind stress data from the NCEP/CFSr (from 1949 to 2010) and NCEP/CFS version 2 (NCEP/CFSv2) (from 2011-present). The annual mean Ekman transport in the calendar year of the cruise is used (cf. Table 3.2 for the values).

Considering the above listed additional constrains and the conservation equations for the properties in each of the 17 layers and the whole box, we can formulate in total 59 equations for the 1989/1992 box, and 60 equations for the 2013/2015 box. Given the much larger number

of unknowns, the box inverse model is always an underdetermined system. Conventionally, the equations can be written in a matrix form

$$Ax = b, \tag{3.2}$$

where A is a $M \times N$ matrix that consists of areas of the station pairs in layers multiplied by the property concentration, and areas of the neutral density surfaces multiplied by the property concentration on that surface; x is a $N \times 1$ matrix of unknowns that consist of reference geostrophic velocity at the station pairs and dianeutral velocity for the properties; b is a $M \times 1$ matrix that consists of property transport due to the relative geostrophic velocity; M is the number of equations; N is the number of unknowns.

3.3.3 Reference level and a prior reference velocity

The reference level for the geostrophic velocity calculation must to be chosen first. An ideal choice would be a level of no motion, but which is rarely found in the real ocean. Therefore, a density surface that separates the northward flowing water masses (i.e. AAIW and AABW) from the southward flowing water masses (i.e. NADW) is preferable for the reference level with zero velocity as an initial guess (e.g. *Klein et al.* 1995; *Ganachaud and Wunsch* 2000). For the 14.5° N section, the reference level for the 1989 realization was chosen following *Klein et al.* (1995) as the surface of $\gamma_n = 27.82$ kg m^{-3}, which separates the AAIW and the UNADW. For the 2013 realization along the 14.5° N section and both realizations along the 24.5° N section, the reference level was defined by $\gamma_n = 28.1295$ kg m^{-3}, which separates the LNADW and AABW (*Ganachaud and Wunsch*, 2000; *Hernández-Guerra et al.*, 2014). The neutral surfaces with $\gamma_n \geq 28.1295$ kg m^{-3} tilt upward toward the east on the western side of the MAR. Therefore, it would favor a northward flow in the AABW layers when using $\gamma_n = 28.1295$ kg m^{-3} as the reference level with zero reference velocity (Fig. 3.6). For all the sections, when the corresponding density level is deeper then the deepest common depth of the adjacent CTD station pairs, the deepest common depth was then chosen as the reference level. The bottom triangle was set by constantly extrapolating the velocity at the deepest common depth to the bottom. Using these reference levels with zero reference velocity for the sections results in an AMOC-like meridional transport with, for instance, water in the NADW layers (layer 7 to 14) generally flowing southward, and in the bottom layers (layer 15 to 17) flowing northward. However, the imbalance between the two sections has the same order of magnitude as the initial transport itself, indicating that the volume is not conserved in individual layers and the

whole box at this stage. Here initial transport corresponds to the transport derived from the geostrophic velocity assuming zero velocity at the chosen reference levels.

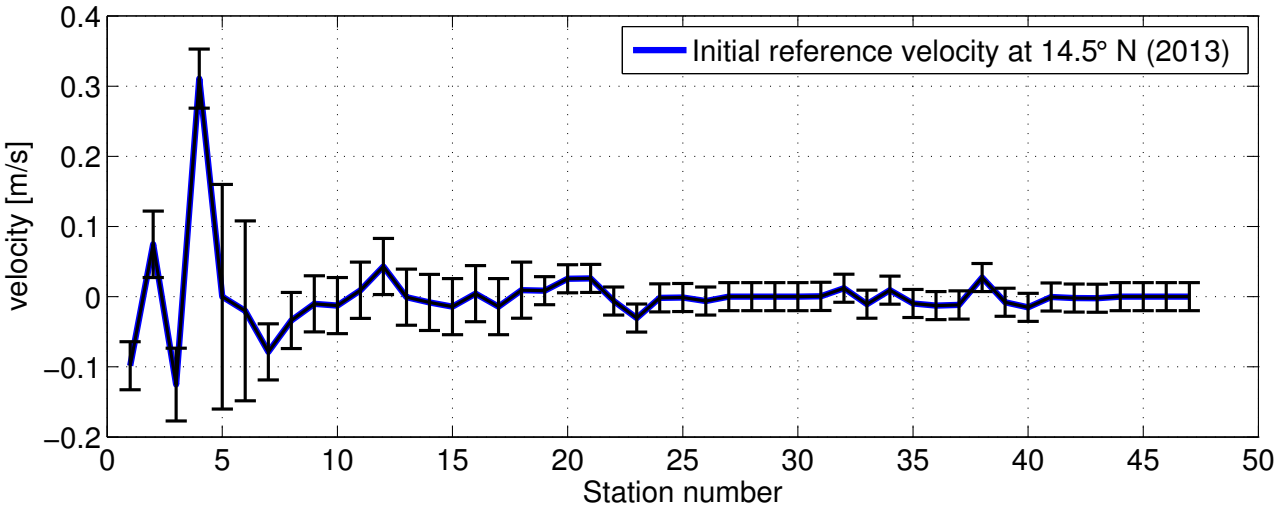

Figure. 3.7 | Initial reference velocity with error bars for the 2013 realization at 14.5° N, estimated from a combination of SADCP and LADCP (see text for details).

In the lack of a prior knowledge on the absolute velocity field, the reference velocities at the reference level are assumed to be 0. This is the case for both realizations at 24.5° N, and for the 1989 realization at 14.5° N. During the occupation along 14.5° N in 2013, both SADCP and LADCP were operated. These direct velocity observations provide valuable information about the velocity at the reference level. *Dengler and Quadfasel* (2002) showed that the vertically averaged LADCP velocity could serve as the reference geostrophic velocity for the corresponding CTD station pairs with an accuracy of 0.012 m s^{-1}. Following their method, the barotropic tide component was first removed from the cross-section LADCP velocity, and then the tide-removed LADCP velocity was averaged between the adjacent CTD stations. The barotropic tide velocity was estimated by using the Tide Model Driver (TMD) (*Egbert and Erofeeva*, 2002). *Fu et al.* (2017) showed that for the 2013 realization, meridional ageostrophic velocity existed mainly in the upper 200 m. Hence, the cross-section LADCP velocity and relative geostrophic velocity were averaged vertically between 200 m and 50 m above the bottom to avoid the influence of any ageostrophic component. Finally, the difference between the vertically averaged LADCP and relative geostrophic velocity was calculated to represent the reference geostrophic velocity. Note that at the western boundary region (westernmost 6 station pairs west of 57.5° W), cross-section velocity from the 38-kHz SADCP was used instead of LADCP velocity. Because the water depth is relatively shallow (less than 1300 m), and the 38-kHz SADCP covered most of the water column with a much higher horizontal resolution (10-minute

ensembles), which makes the horizontal average of the SADCP velocity profiles between the CTD stations more preferable than the two-profile average of LADCP velocities. As shown in Fig. 3.7, the reference velocity for the 2013 realization at 14.5° N shows large positive values at the western boundary, indicating a boundary intensified current. The error bars for station pairs 1-6 were estimated from the root mean squared error of the vertically averaged SADCP velocity (in the range of 200 m and 50 m above the last reliable bin) between each station pairs; for the rest of the station pairs, the uncertainties were given as 0.04 m s^{-1} in the western basin and 0.02 m s^{-1} in the eastern basin, which are larger than the value estimated by *Dengler and Quadfasel* (2002), but is generally assumed for the reference velocity in box inverse model studies (e.g. *Ganachaud* 2003).

3.3.4 Weighting and error estimates

The solution of the box inverse model depends on the a priori knowledge about transport variation as well as uncertainties in the reference velocity field. This can be translated into a row weighting matrix W $(M \times M)$ and a column weighting matrix E $(N \times N)$, which were applied to the system before inversion. Following *Tsubouchi et al.* (2012), the row weighting for volume conservation is defined as

$$W_{mm} = \frac{1}{\varepsilon_m}, \tag{3.3}$$

where ε_m is the a priori volume transport uncertainty for each layer and additional constraints (e.g. FC transport, DWBC, etc.). For property conservation, the row weighting is defined as

$$W_{mm} = \frac{1}{2\eta_m^C \varepsilon_m}, \tag{3.4}$$

where η_m^C is the standard deviation of properties within layer m. To take into account a possible correlations between the section averaged and mesoscale components of the noise in the property conservation equations, a factor of 2 was introduced in the denominator in the right hand side of Eq. 3.4 (*Ganachaud and Wunsch*, 2000; *Tsubouchi et al.*, 2012). Following *Ganachaud* (2003), we set the uncertainties for volume conservation equations to gradually decrease from 8.2 Sv in the surface layer to 0.5 Sv in the bottom layer, and 15.9 Sv for the whole box.

The column weighting was set based on the a priori uncertainties of the reference velocity, δb_j, and the dianeutral velocity, δw_m. For the reference geostrophic velocity, the column weighting is

$$E_j = [\delta b_j / A_j]^{1/2}, \tag{3.5}$$

and for the dianeutral velocity, the column weighting is

$$E_m = [\delta w_m / Q_m]^{1/2}, \tag{3.6}$$

where A_j and Q_m are the vertical area between the station pairs and the horizontal area of the layer interfaces (neutral density surfaces), respectively. Except for the 2013 realizations at 14.5° N, the a priori uncertainties for the reference velocity of the other three realizations were assumed to be 0.04 m s^{-1} at the western boundary region due to its large variability, and 0.02 m s^{-1} for the rest of the station pairs (*Ganachaud*, 2003; *Hernández-Guerra et al.*, 2014). For the 2013 realization, the a priori uncertainties at the western boundary were estimated based on the variability of the SADCP velocity (Fig. 3.7, see Sect. 3.3.3 for details). The dianeutral exchanges of volume, salt and heat are expected to be small in the tropical Atlantic, we set the a priori uncertainty of the dianeutral velocity to be in the order of 10^{-6} m s^{-1}.

Applying the row and column weightings to Eq. 3.2, we have

$$(WAE)(E^{-1}x) = Wb, \tag{3.7}$$

which can be written as

$$A''x' = b', \tag{3.8}$$

with $A'' = WAE$, $x' = E^{-1}x$, and $b' = Wb$. The weighted system can be solved by using SVD (*Wunsch*, 1996) by choosing a rank where data residual norms are of O[1 to 2 Sv] (*Sloyan and Rintoul*, 2001). An error covariance matrix P can be formulated using the Gauss-Markov method. The a posteriori errors of the solution were estimated as the square root of the diagonal components of P, where

$$P = E - EA^T(AEA^T + W)^{-1}AE. \tag{3.9}$$

3.3.5 Sensitivity tests of the inverse model

It is of interest to test how sensitive the inverse results are to the initial conditions and constraints. The 1992 realization at 24.5° N have been used in several previous studies (e.g. *Ganachaud* 2003; *Lumpkin and Speer* 2003; *Hernández-Guerra et al.* 2014), we found that the circulation structure and strength is very stable among these studies, even though different hydrographic sections were combined with this realization to build the box inverse models. This can be attributed to the similar steady-state initial condition and constraints applied to the box inverse models. To further quantitatively answer the question, we performed three sensitivity

experiments on the 14.5° N section as follows and referred to the box inverse model described in Sect. 3.3.1-3.3.4 as the "control run".

- Sensitivity to the meridional Ekman transport. In this experiment, we used the 1989/1992 box and artificially doubled the Ekman transport at 14.5° N to 17.6 Sv, everything else is identical to the control run.

- Sensitivity to the initial reference velocity. In the "control run" of the 2013/2015 box, the reference velocity for the 14.5° N section was estimated using the SADCP/LADCP velocity. In order to test how much the initial reference velocity affects the finial transport, we replaced the initial reference velocity at 14.5° N of the 2013/2015 box with 0, and kept everything else identical to the control run.

- Sensitivity to hydrographic variability. To assess the effect of hydrographic variability on the inverse model solution, we conducted 6 experimental runs using the 2013 realizations at the 14.5° N section in combination with six realizations of the 24.5° N section (1992, 1998, 2004, 2010, 2011, and 2015, data available from CCHDO and World Ocean Database). For all six experimental runs, we used the long-term mean Ekman transport calculated using the monthly NCEP/CFSr wind stress (1979-2010) for both sections and a long-term mean FC transport (31.1 ± 2.4 Sv) at 24.5° N, and kept everything else identical to the control run. In this way, we could examine the stability of the results at 14.5° N against the hydrographic variations at 24.5° N.

3.3.6 Heat and freshwater flux estimation

The heat and freshwater fluxes through the two sections were estimated using the results from the box inverse model. Note that after the inversion the total volume flux through a section should be quasi zero (except a 0.5-0.8 Sv Bering Strait transport). Therefore, the total heat flux through a section, H_{sect}, can be regarded as a sum of warm northward Ekman transport at the surface, H_e, and a much colder southward returning geostrophic flow over the full water column, H_g:

$$H_{sect} = H_e + H_g, \tag{3.10}$$

H_e was calculated as

$$H_e = \frac{C_p}{f} \sum_{j=1}^{N} \theta_j^{surf} \tau_j^x \Delta x_j, \tag{3.11}$$

where f is the Coriolis parameter; C_p is the specific heat capacity of seawater; θ_j^{surf} is the mean in-situ SST between the station pair; τ_j^x is the zonal wind stress from NCEP/CFSr. In this study, we use g and C_p as constants of 9.8 m s^{-2} and 4000 J kg^{-1} K^{-1}, respectively. Note that we only use the in-situ SST to calculate the Ekman heat transport, since it has been shown by *Fu et al.* (2017) that in the tropical Atlantic the Ekman heat fluxes estimated using in-situ SST and temperature profile data within the Ekman layer only differ marginally. H_g was calculated as

$$H_g = \rho C_p \int\int \bar{\theta} v^{abs} dx dz = \rho C_p \sum_j \sum_m \bar{\theta}_{m,j} v_{m,j}^{abs} \Delta x_j \Delta h_{m,j}, \tag{3.12}$$

where $v_{m,j}^{abs}$ is the absolute geostrophic velocity in the cell of layer m, bounded by station pair j, as obtained from the box inverse model; $\bar{\theta}_{m,j}$ is the mean in-situ potential temperature in the same cell of $v_{m,j}^{abs}$; $\Delta h_{m,j}$ is the thickness of layer m at station pair j.

Freshwater flux through a section was achieved in the sense of salt and mass conservation between the Bering Strait and the corresponding section. It can be expressed as follows (cf. *Friedrichs and Hall* 1993; *McDonagh et al.* 2015 for details):

$$F_{sect} = M_{net} - \frac{M_{BS}\overline{S_{BS}} + M_e\overline{S_e} + M_g\overline{S_g} + M_w\overline{S_w}}{< S >}, \tag{3.13}$$

where M_{net} is a net barotropic flow through the section; M_{BS}=0.8 Sv is the Bering Strait transport, and $\overline{S_{BS}}$=32.5 is the mean salinity at the Bering Strait; $< S >$ is the section-areal mean salinity; M_e, M_g, and M_w are the Ekman and interior geostrophic, and western boundary volume transport, respectively; $\overline{S_e}$, $\overline{S_g}$, and $\overline{S_w}$ are the Ekman, interior geostrophic, and western boundary transport-averaged-salinity. $\overline{S_e}$ and $\overline{S_g}$ are defined as follows, $\overline{S_w}$ is analogue to $\overline{S_g}$:

$$\overline{S_e} = \frac{\frac{1}{f\rho}\sum_j^{surf} \tau_j^x \Delta x_j}{M_e}, \tag{3.14}$$

and

$$\overline{S_g} = \frac{\sum_j \sum_m S_{m,j} v_{m,j}^{obs} \Delta x_j \Delta h_{m,j}}{M_g}, \tag{3.15}$$

where $\overline{S_{m,j}}$ is the mean in-situ potential temperature in the same cell of $v_{m,j}^{abs}$; S_j^{surf} is the mean in-situ SSS between the station pair j; τ_j^x is the zonal wind stress at station pair j; v is the absolute meridional geostrophic velocity. Note that the western boundary current region at 14.5° N is defined by the western most 6 station pairs, and in the upper 1000 m, while at 24.5° N it is the Florida Straits.

3.4 Inverse model results

3.4.1 Adjustment and final transport

The final adjustments to the reference velocity were achieved by solving the box inverse model built with the 14.5° N and 24.5° N sections for the two periods (Fig. 3.8). For both periods, the largest adjustments appear in the boundary regions, where the a priori uncertainty of the reference velocity is large. For the rest of the sections, the adjustments are small and not significantly different from zero. Similar to the previous inverse model studies, the a posteriori errors have similar magnitude of the a priori uncertainties of the unknowns (*Ganachaud*, 2003; *Hernández-Guerra et al.*, 2014).

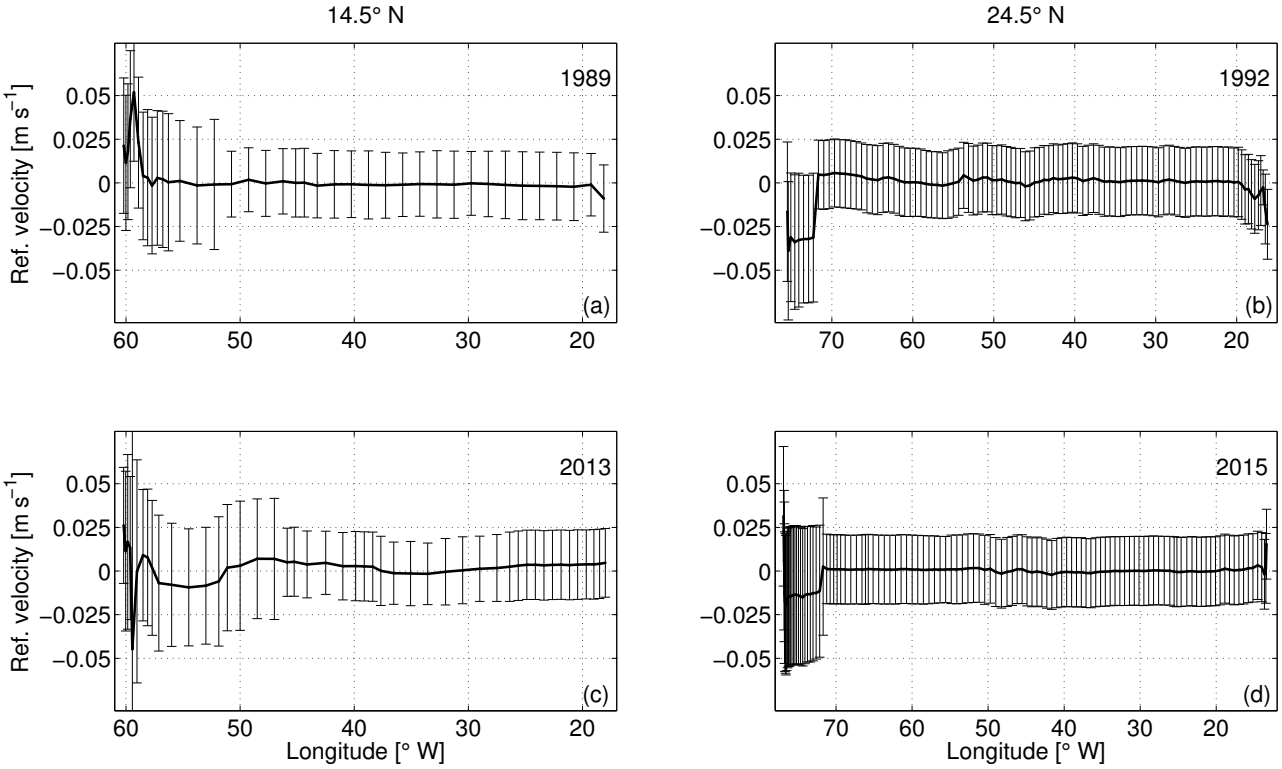

Figure. 3.8 | Final adjustments to the reference velocity with uncertainties along 14.5° N in (a) 1989 and (c) 2013; and along 24.5° N in (b) 1992 and (d) 2015. Note that except for the section along 14.5° N in 2013, the initial reference velocity is 0; therefore, the final adjustments in (a), (b), and (d) are equivalent to the final reference velocity.

In general, the dianeutral velocity is not significantly different from zero, except in the bottom layer (γ_n=28.152 kg m^{-3}) of the 2013/2015 period, where strong upward velocity is observed (Fig. 3.9). A similar structure of the dianeutral velocity was also achieved by *Ganachaud* (2003) for the tropical North Atlantic box bounded by 7.5° N and 24.5° N. The densest AABW

flows northward in the tropical North Atlantic at the bottom of the western basin, it mixes with the LNADW, resulting in water mass transformation and volume reduction of the AABW. Therefore, it is expected that upwelling occurs in the bottom layer. However, in the 1989/1992 period a downwelling velocity appears at γ_n=28.152 kg m^{-3} due to a divergence of the horizontal geostrophic transport in the bottom layer (Fig. 3.10a). Note that the horizontal area of the surface γ_n=28.152 kg m^{-3} is very small since it only exists in the abyssal basin west of the MAR. Therefore, a downwelling velocity in the bottom layer will not change the fact that the AABW as whole upwells, when the upwelling velocity and the much larger horizontal area of the layer surface γ_n=28.141 kg m^{-3} is taken into account.

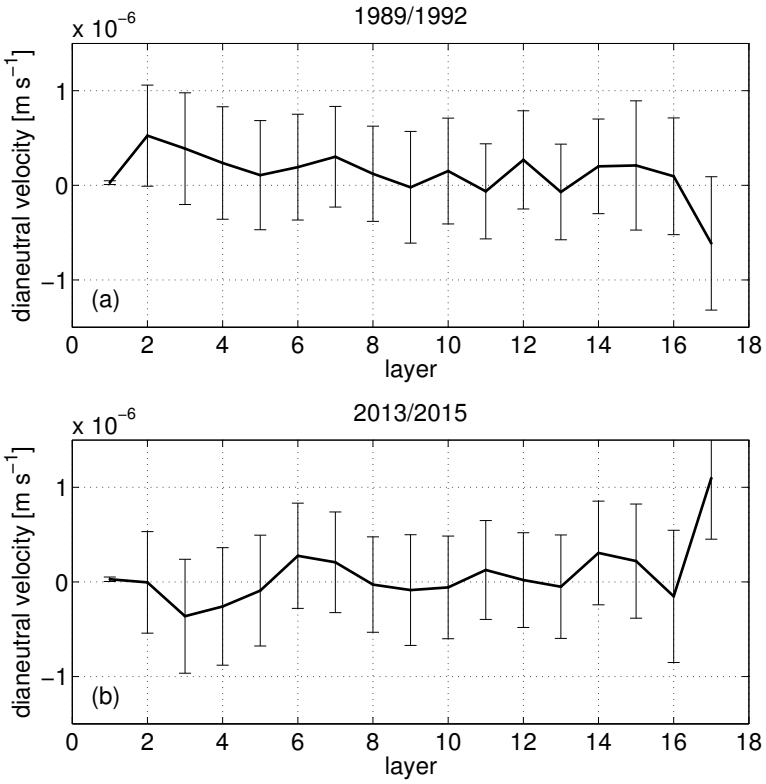

Figure. 3.9 | The dianeutral velocity across the layer interfaces between the two sections for the periods of (a) 1989/1992 and (b) 2013/2015.

Using the adjustments to the reference velocity and the dianeutral velocity, the zonally integrated final transport per layer is calculated, including the Ekman transport in the first layer (Fig. 3.10). Compared to the initial transport (not shown), clear overturning structures with southward NADW and northward upper, intermediate and bottom waters are achieved for both sections during the respective surveys. The imbalance in layers has been reduced indistinguishable from zero, which implies volume conservation in both boxes after inversion. The final transport of water masses can be then calculated by integrating the layer transport

Table. 3.3 | The final adjusted transport (Sv) of water masses, DWBC, and AMOC intensity at the two sections in the respective years. Southward transport is marked with "-". The values in the brackets at 24.5° N denote the transport results including the Florida current transport in the corresponding water mass layers.

	14.5° N		24.5° N (including Florida)	
	1989	2013	1992	2015
Thermocline	5.0±1.7	3.7±3.3	-18.0±1.1 (11.2±1.1)	-21.0±1.2 (9.3±1.2)
Intermediate	4.2±2.2	2.6±1.7	1.5±1.2 (3.5±1.2)	1.6±1.2 (3.1±1.2)
UNADW	-12.1±3.2	-6.8±2.6	-12.2±1.7	-9.4±1.9
LNADW	-8.6±6.1	-10.0±6.7	-9.9±5.2	-10.4±5.5
AABW	2.2±2.3	1.8±2.3	2.0±2.5	2.0±2.6
DWBC	-22.7±9.6	-17.9±8.0	-26.8±4.6	-25.4±4.1
AMOC	18.6±2.7	14.7±3.9	19.2±1.7	16.9±1.6

over the corresponding layers of a water mass. As summarized in Table 3.3, for the 14.5° N section, the thermocline water (layer 1-3) has northward transport of 5.0 ± 1.7 Sv in 1989, and 3.7 ± 3.3 Sv in 2013. The intermediate water (layer 4-6) transport is 4.2 ± 2.2 Sv northward in 1989 while only 2.6 ± 1.7 Sv in 2013, which is considerably weaker in the latter period. Note that due to the higher weighting (small uncertainty in the constraints) of the intermediate water transport at 14.5° N in 2013, the final intermediate water transport in 2013 is very close to the prescribed value of 2.8 ± 2.1 Sv. It is important to point out that without this constraint, the final intermediate water transport would be even southward, no matter which reference level is chosen, and whether the SADCP/LADCP reference velocity is applied or not. This is undesirable and can be seen as a strong indication that the intermediate water transport in 2013 is substantially weaker than that in 1989. Recall the increasing temperatures and salinities in the AAIW layer at 14.5° N between 1989 and 2013, which may be explained by the reduction in the northward supply of fresh and cool AAIW water between the two periods.

In response to the much weaker northward thermocline and intermediate water transport, the UNADW (layer 7-11) transport of -6.8 ± 2.6 Sv in 2013 is also much weaker than that of -12.1 ± 3.2 Sv in 1989 ("-" denotes southward). The LNADW (layer 12-15) transport of the periods is very close to each other (-8.6 ± 6.1 Sv in 1989 vs. -10.0 ± 6.7 Sv in 2013). The AABW (layer 16-17) transport is very close between the two realizations, with 2.2 ± 2.3 Sv in 1989, and 1.8 ± 2.3 Sv in 2013, but the northward core of AABW transport shifts to a denser layer (from layer 16 to 17) between 1989 and 2013.

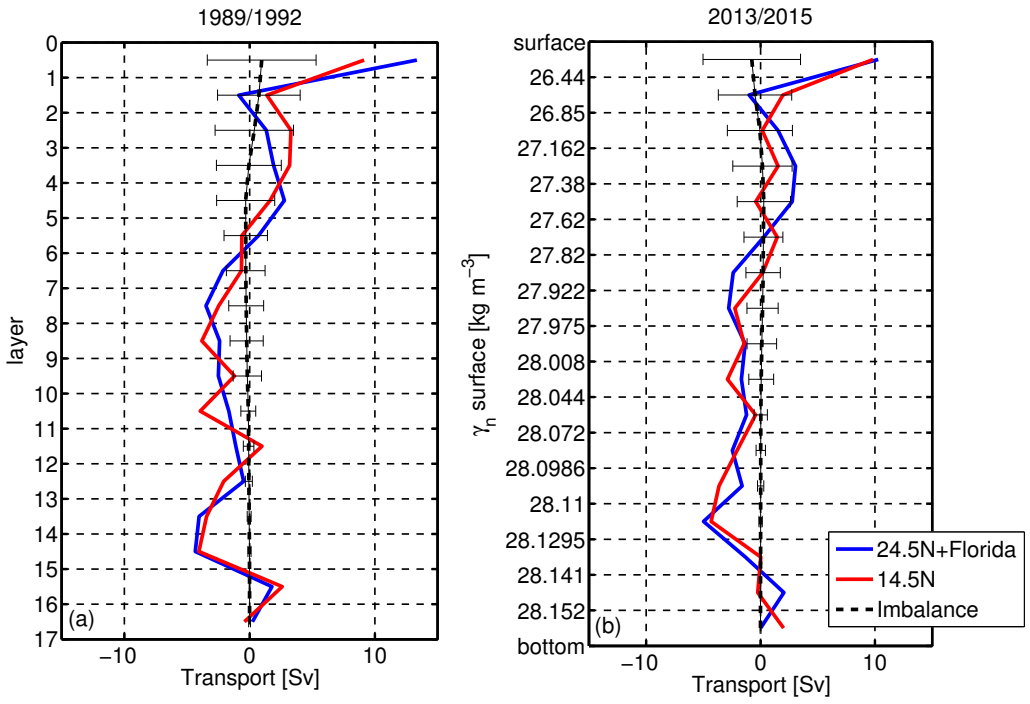

Figure. 3.10 | Final layer transports for the periods (a) 1989/1992 and (b) 2013/2015. The blue curves are the transports at the 24.5° N section including the Florida current transport, the red curves mark the transport at the 14.5° N section, the black dashed lines are the final imbalance of the layers with error bars.

At 24.5° N, in contrast to the 14.5° N section, the circulation structure is relatively stable between 1992 and 2015 (Fig. 3.11b). The transport of thermocline water (layer 1-4) excluding the FC transport is -18.0 ± 1.0 Sv in 1992, while it is -21.0 ± 1.1 Sv in 2015, which is stronger southward. The northward intermediate water (layer 5-6) transport is also slightly weaker in 2015 (3.1 ± 1.2 Sv) than in 1992 (3.5 ± 1.2 Sv). A stronger southward transport in the thermocline water and a weaker northward transport in the intermediate water indicate together a weaker northward transport in the upper ocean in the more recent period than in the former period. As a result, the southward UNADW (layer 7-11) transport of -9.4 ± 1.9 Sv in 2015 is also weaker than that of -12.2 ± 1.7 Sv in 1992. The LNADW (layer 12-15) transport is indistinguishable between the two periods (-9.9 ± 5.2 Sv in 1992 vs. -10.4 ± 5.5 Sv in 2015). The AABW transport is also nearly identical between the two periods (2.0 ± 2.5 Sv in 1992 vs. 2.0 ± 2.6 Sv in 2015).

In order to compare the intensity of the AMOC between the different periods, an overturning stream function of each realization was calculated by cumulatively integrating the layer transport from the surface to the bottom (Fig. 3.11). The AMOC strength is defined as the maximum northward transport of the overturning stream function. At 14.5° N, the AMOC strength is 18.6 ± 2.7 Sv in 1989, and 15.3 ± 3.8 Sv in 2013. At 24.5° N, the AMOC strength is

19.2 ± 1.5 Sv in 1992, and 17.7 ± 1.6 Sv in 2015. It appears that at both latitudes the AMOC is weaker during 2013/2015 than during 1989/1992, although not significantly. As described above, at both latitudes, we see a reduction of northward thermocline and intermediate water between the two periods, which is compensated by a decrease of the southward UNADW transport. It is worth to note that, the 1992 realization at 24.5° N has been used by many global and regional inverse studies (*Ganachaud*, 2003; *Lumpkin and Speer*, 2003; *Hernández-Guerra et al.*, 2014). Despite the fact that various other sections are combined with this realization to perform box inverse models, the vertical circulation structure and the transport strength are strikingly similar for this realization. All these studies have imposed a more or less time-mean Ekman transport and FC transport, as well as similar a priori errors (weightings) to the box inverse model. This indicates that given a steady-state initial condition, stable inverse results may be achieved, though the baroclinic structures and measurement errors (e.g. due to internal wave field) of the combined section are very different.

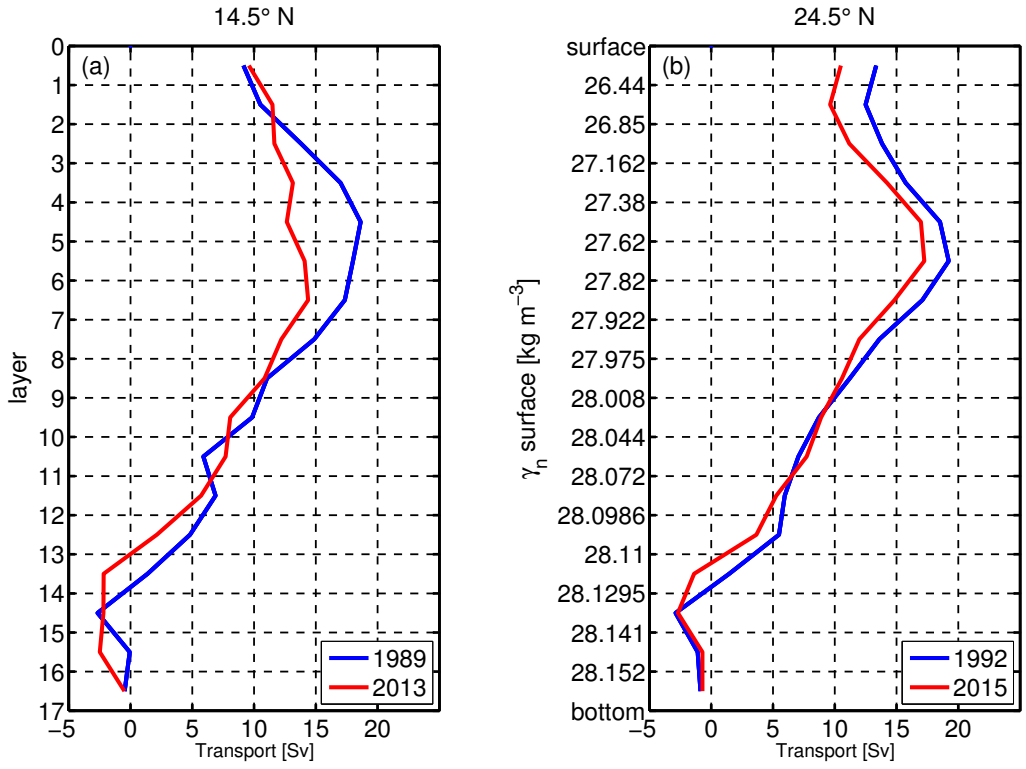

Figure. 3.11 | Meridional overturning stream function from the inverse model at (a) 14.5° N and (b) 24.5° N. It is calculated by cumulatively integrating the layer transport from the surface to the bottom. The vertical coordinate in (a) is the layer number, and in (b) the corresponding neutral density surface. For the 14.5° N section, the blue curve stands for the 1989 realization, the red curve for the 2013 realization. For the 24.5° N section, the blue curve stands for the 1992 realization, and red curve for the 2015 realization.

3.4.2 Horizontal circulation pattern

The absolute geostrophic velocity sections are shown in Fig. 3.12. In the upper 1000 m at 14.5° N, intensified northward currents are confined at the western boundary. In 1989, the two branches of the western boundary current with nearly equal amount of transport are located within a narrow channel and along the continental slope. A very weak southward flow separates the two branches in between. The western boundary current transport at 14.5° N in 1989, estimated by integrating the final total velocity from the western boundary to the eastern extent (58.30° W) of the northward current in the upper 1000 m, is 27.6 ± 3.2 Sv, which is somewhat larger than an estimate of 18 to 24 Sv by *Klein et al.* (1995). However, the difference does not come surprisingly, since their result was obtained by using a seasonal Ekman transport of 15.94 Sv, which is more than two times higher than an annual mean value of 7.9 ± 3.5 Sv estimated by *Fu et al.* (2017). As Ekman transport and western boundary current are the dominant northward components of the AMOC in the tropics, such a strong Ekman transport would result in, to the lowest order of volume conservation, a weaker western boundary current. The impact of a large Ekman transport on the transport results is discussed as a case study later.

In 2013, the western boundary current was not evenly distributed into two branches; instead, it was much more confined in the narrow channel, and amounted to 26.9 ± 3.7 Sv. This value compares favorably with a transport of 25.3 ± 9.2 Sv estimated using the LADCP cross-section velocity and errors within the channel. Along the continental slope it was much weaker, and almost replaced by a much stronger southward flow compared to that in 1989. At 24.5° N, the western boundary current system is primarily the FC with a transport of 31.2 ± 0.3 Sv and 32.0 ± 0.9 Sv in 1992 and 2015, respectively. These values are not significantly different from the constrained values (cf. Table 3.2), and are consistent with a long-term mean value of 31.1 ± 2.4 estimated by *Atkinson et al.* (2010).

Along the western boundary at greater depth, two southward velocity cores can be seen in all sections over a neutral density range of 27.82 to 28.072 kg m^{-3} and 28.072 to 28.141 kg m^{-3}, respectively (Fig. 3.12), which are associated with the DWBC. The high oxygen concentration found in the deep western boundary region roughly coincides with the depth of the DWBC velocity cores (Fig. 3.5). For the 2013 realization at 14.5° N, the dual-core structure mentioned above is also evident in the oxygen section with oxygen concentration larger than 260 μmol kg^{-1}. The relatively lower oxygen concentration at about 3000 m between the two

cores also coincides with a minimum southward flow in the corresponding neutral density layer ($28.044 < \gamma_n < 28.072$ kg m^{-3}, Fig. 3.10b). This structure is consistent with the vertical structure of the NADW transport observed in the western basin by the MOVE at 16° N (*Send et al.*, 2011). *Send et al.* (2011) showed that the annual mean NADW transport has two southward maxima located at 2000 m and 4000 m, corresponding to the LSW and DSOW, respectively, and a minimum in between centred at 3000 m, corresponding to the ISOW. The high oxygen concentration in this area also implies the presence of relatively recently formed waters of northern origin (LSW, ISOW, and DSOW), which is also evident from higher transient tracer concentrations (e.g. Chlorofluorocarbon, CFC; *Molinari et al.* 1992).

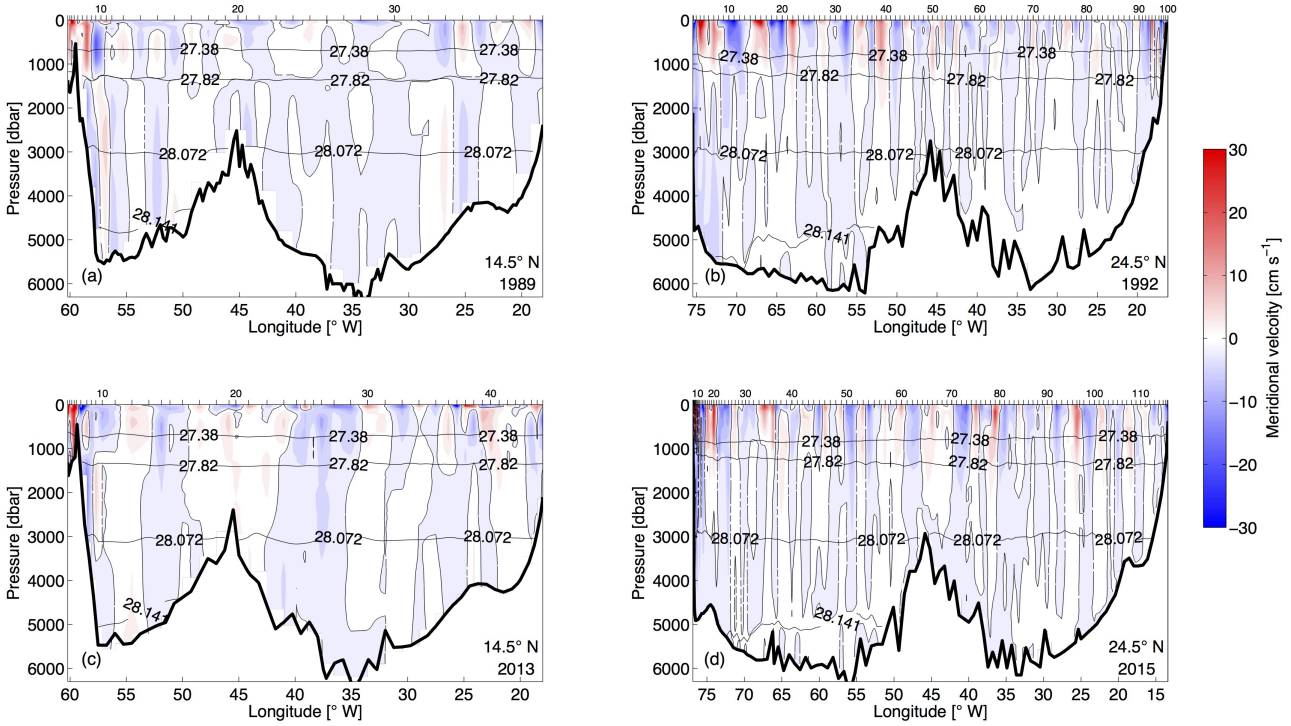

Figure. 3.12 | Absolute meridional geostrophic velocity (cm s^{-1}) along 14.5° N in (a) 1989 and (c) 2013, and along 24.5° N in (b) 1992 and (d) 2015. The station pair number is marked on the top horizontal axis. The black dashed contour line is the zero velocity contour. The black solid lines with values are the neutral density surfaces for the corresponding sections, which typically separate the thermocline water, AAIW, UNADW, LNADW, and AABW.

In order to calculate the DWBC transport, an eastern boundary of the DWBC must be defined for integration purpose. This boundary is defined by the eastward extension of the southward velocity in the NADW layers ($27.82 < \gamma_n < 28.141$ kg m^{-3}) in the western basin. At 14.5° N, we used 51° W for both realizations as the eastern boundary of the DWBC, which coincides with the high-CFC cores measured during the 1989 realizations (cf. Fig. 3 in *Molinari*

et al. 1992), and with the high-oxygen cores measured during the 2013 realizations (Fig. 3.5c), respectively. Note that this definition includes the northward recirculation branches near the continental slope. The resulting DWBC transport is -22.7 ± 9.6 Sv in 1989 and -17.9 ± 8.0 Sv in 2013, respectively. For the 24.5° N section, we used 72° W as the eastern boundary of the DWBC for both realizations, resulting in a DWBC transport of -26.8 ± 4.6 Sv in 1992 and -25.4 ± 4.0 Sv in 2015, respectively.

The DWBC transport estimates at 14.5° N compare favorably with an estimate of 25 Sv at 10° N in the Atlantic by *Speer and McCartney* (1991), and a mean DWBC transport of 26.0 ± 8.0 Sv in the tropical North Atlantic by *Molinari et al.* (1992), which is calculated by using repeated cruise sections between 14.5° N and the equator. *Friedrichs and Hall* (1993) have shown that at 8° N in the Atlantic, 27 Sv were transported southward within the DWBC along the continental slope, which was accompanied by a northward recirculation of 16 Sv primarily along the western flank of the MAR. They further schematically showed that the whole tropical North Atlantic adopted such a circulation pattern. However, in this study, at 14.5° N, northward recirculation occurred at the western flank of the MAR, but also near the continental slope to the east of the southward cores of the DWBC. For the 1989 realization, the recirculation near the continental slope accounts to 12.5 Sv, while that at the western flank of MAR is 14.8 Sv. For the 2013 realization, the recirculation near the continental slope is 16.9 Sv, while northward velocity is found in a large area over the MAR, which is likely a compensating flow of the strong southward velocity with similar strength between 42 and 35° W (Fig. 3.12). Due to the limitation of the maximum operation depth (6000 m), the LADCP was not operated in this area. But a strong southward flow is still evident in the SADCP sections in the upper 1200 m (not shown).

3.4.3 Sensitivity of the box inverse model

As described in Sect. 3.3.5, three sensitivity experiments were conducted to test the sensitivity of the box inverse model to the different initial conditions and constraints. The results of the sensitivity tests are presented here and compared with the results presented in Sect. 3.4.1 and 3.4.2 (referred to as "Control run").

3.4.3.1 Response to meridional Ekman transport

This experiment shows that the upper ocean geostrophic transport has an immediate response to the change in the Ekman transport at the same section. When the Ekman transport at 14.5° N in the 1989/1992 box is artificially doubled (from 8.8 Sv in the control run to 17.6 Sv in the experimental run), the thermocline and intermediate water transport strongly decreases, from 5.0 ± 1.7 Sv and 4.2 ± 2.2 Sv (in the control run) to -0.6 ± 1.7 Sv and 1.5 ± 2.2 Sv, respectively. The NADW and AABW transport as well as the overturning strength change only marginally. The transport at 24.5° N is also insensitive to the change in the Ekman transport at 14.5° N. This may explain the very small (even southward) AAIW transport (-0.7 Sv) in the seasonal case of *Klein et al.* (1995), who applied an extremely large Ekman transport (15.94 Sv) at 14.5° N to a box inverse model combining the 1989 realization at 14.5° N and 1957 realization at 8° N.

3.4.3.2 Sensitivity to reference velocity

This experiment shows that the circulation pattern is sensitive to the reference velocity, but the AMOC strength is not. As shown in Fig. 3.7, the initial reference velocity (2013 at 14.5° N) along the continental slope (station pair 7 to 10) is mainly southward. Removing the initial reference velocity of the 2013 realization at 14.5° N would decrease the UNADW transport from 6.8 ± 2.6 Sv to 4.6 ± 2.6 Sv, and the total DWBC transport from 17.9 ± 8.0 Sv to 11.9 ± 8.0 Sv, which is certainly too weak compared to the expected DWBC transport at this latitude (16-27 Sv, *Molinari et al.* 1992). Such a dramatic change in the DWBC is not surprising, provided the least-square nature of the box inverse method, it would always minimize the size of the correction to the initial reference velocity (*McIntosh and Rintoul*, 1997). Therefore, the experimental run can hardly reproduce the magnitude of certain circulation elements (e.g. DWBC) defined by the reference velocity that is far away from 0. Besides, initializing the reference velocity using known (observed) velocity field is common in box inverse studies (e.g. *Tsubouchi et al.* 2012), and we believe it provides us a robust circulation pattern in this study.

3.4.3.3 Effect of hydrographic variability

The results show that the hydrographic variation at one section does affect the circulation structure and strength at the other section. Taking the AMOC strength as an indicator, in the six experimental runs combining the 2013 realization of 14.5° N, the AMOC strength at

14.5° N varies between 11.4 ± 3.7 Sv (2013/2004 run) and 16.7 ± 3.7 Sv (2013/1992 run) with a mean value of 14.4 Sv. These results are not significantly different from that of the control run (15.3 ± 3.9 Sv). Since all the constraints and initial conditions were given using the long-term mean value and kept unchanged among the runs, the only candidate for the change is the different baroclinic and horizontal shear structures that are related to interannual to decadal variability or/and the measured eddy and internal wave field. Note that among the six experimental runs, the AMOC strength at 14.5° N from the combinations of 2013/2010, 2013/2011, and 2013/2015 is very stable (15.6 ± 3.7 Sv, 15.3 ± 3.6 Sv, and 14.8 ± 3.8 Sv, respectively). This is an indication of the importance to perform a box inverse model using sections occupied in the nearby years.

3.4.4 Heat and freshwater fluxes

At 14.5° N, we estimated the heat flux through the section as northward 1.03 ± 0.14 PW (1 PW = 10^{15} Watt) in 1989 and 1.11 ± 0.15 PW in 2013. Despite the fact that the strength of AMOC is weaker in 2013 than in 1989, the heat flux in 2013 is even slightly larger than that in 1989. This can be attributed to the source of the transport changes and to the higher mixed layer temperature (a mean offset of 1.60 °C in the upper 50 m) during the occupation in May 2013 than in February 1989. As shown in Fig. 3.11, the reduction of AMOC strength occurs mainly in the lower thermocline and intermediate water transport (layer 3-5), which carries much less heat northward compared with the surface water transport (layer 1-2). The surface water transport is even stronger in 2013 than in 1989. Compared with the estimates of 1.22 PW (annual case) or 1.37 PW (seasonal case) by *Klein et al.* (1995), our heat transport estimate for the 1989 realization is small. However, in the sensitivity test (Sect. 3.4.3), corresponding to a 17.6 Sv Ekman transport, the heat flux amounts up to 1.50 ± 0.14 PW, which explains the large heat fluxes in *Klein et al.* (1995). *Fu et al.* (2017) showed that in the tropical Atlantic SST can be used to represent the transport-weighted mean temperature in the Ekman layer, and that the uncertainty of the Ekman volume transport dominates the uncertainty of the Ekman heat flux. Combining their conclusion with the results of the sensitivity test to the Ekman transport, it is suggested that the total heat flux across 14.5° N is sensitive to the Ekman volume transport.

The heat flux through the 24.5° N section is estimated as northward 1.39 ± 0.10 PW in 1992 and 1.08 ± 0.11 PW in 2015. The strong decrease of the heat flux between the two years reflects the reduction of the northward transport in the surface layers (layer 1-4, Fig. 3.11). The heat

flux at 24.5° N has been estimated for several times in previous studies, especially for the 1992 realization; for instance, *Ganachaud* (2003) calculated a heat flux of 1.27 ± -0.15 PW in 1992; *Hernández-Guerra et al.* (2014) estimated the heat flux as 1.4 ± 0.1 PW in 1992 and 1.2 ± 0.1 PW in 2011. All the above listed heat flux estimates align with a RAPID array-based estimate of 1.25 ± 0.36 PW (mean $\pm$ standard deviation) by *Johns et al.* (2011) at 26.5° N.

Freshwater flux across the 24.5° N section was -1.24 ± 0.20 and -0.96 ± 0.20 Sv in 1992 and 2015, respectively. For the 1992 realization, the estimate here agrees well with that of -1.23 Sv by *Rosón et al.* (2003) and -1.16 Sv by *McDonagh et al.* (2015). The estimate in 2015 falls in the range of -0.93 to -1.26 Sv based on hydrographic data or -1.17 ± 0.20 Sv based on RAPID array data (see *McDonagh et al.* 2015 for a summary). At 14.5° N the freshwater flux was -1.00 ± 0.15 and -1.02 ± 0.22 Sv in 1989 and 2013, respectively. This is the first freshwater flux estimation at 14.5° N based on hydrographic data; compared to the estimates based on surface freshwater flux (i.e. integrating the evaporation, precipitation and river runoff from a northern latitude with initial condition; *Wijffels et al.* 1992), it is somewhat larger. However, given a net surface freshwater loss of about 0.3 Sv between 24.5° N and 14.5° N estimated using HOAPS data and -1.17 ± 0.20 Sv as the initial condition at 24.5° N, the estimates at 14.5° N are still within the uncertainty range.

Note that the uncertainties of the freshwater fluxes were estimated following *Friedrichs and Hall* (1993) as the amount of freshwater flux change due to an assumed salinity uncertainty of 0.2 psu in the western boundary at each section. This assumption is based on the fact that the freshwater flux is very sensitive to the transport-weighted salinity in the western boundary $\overline{S_w}$ rather than any transport component in Eq. 3.13. At both latitudes, an uncertainty of ± 0.2 psu in $\overline{S_w}$ leads to a freshwater uncertainty of 0.1-0.2 Sv, while about 10 Sv change in $\overline{M_w}$ would be required to obtain a freshwater flux change of the same amount.

3.5 Comparison with the GECCO2 state estimate, RAPID and MOVE analysis data

The inverse results for the two sections during two different periods have shown overturning structure of comparable strength with previous studies in similar regions. At 24.5° N, the RAPID array data provide estimates of meridional transports across the section from Apr 2004 to Oct 2015 (*Smeed et al.*, 2016). Here, we calculated the meridional overturning stream function using the absolute velocity field of the 2015 realization obtained from the inverse

model, and compared it with the mean meridional overturning stream function of the RAPID array in 2015. Note that the transport for the RAPID array is calculated based on depth levels. Therefore, for comparison, the overturning transport of the inverse results is also calculated as a function of depth. As shown in Fig. 3.13, the meridional overturning transport from the inverse method and the RAPID array are overall consistent with each other. The inverse result shows a slightly stronger overturning strength (16.9 ± 1.6 Sv for the inverse method, 16.1 ± 4.4 Sv for the RAPID array), which is defined as the maximum transport in the meridional overturning stream function, typically at about 1000 m. The uncertainty of the RAPID array is given by the standard deviation of the RAPID time series (Apr 2004-Oct 2015). Note that the definition of water masses for the RAPID array is based on depth levels (thermocline water 0-800 m, intermediate water 800-1100 m, UNADW 1100-3000 m, LNADW 3000-5000 m, AABW > 5000 m), while for the inverse model, the water masses are defined by the neutral density surfaces. To best represent the depth definition of water masses, we have chosen the neutral density surfaces of 27.38, 27.83, 28.072, 28.1295 kg m^{-3} as the boundaries between these water masses. Note that here the boundary between the LNADW and AABW is different from the previous definition only for comparison purpose. The thermocline water transport without the Florida current is -21.0 ± 1.2 Sv for the inverse method, and -20.1 ± 3.0 Sv for the RAPID array. The intermediate water transport of the inverse method (1.6 ± 1.2 Sv) is slightly stronger than the RAPID (0.6 ± 0.6 Sv). The largest difference in the overturning stream function between the two estimates occurs at about 3000 m, the transport approaches to each other gradually between 3000 and 5000 m. This indicates that in comparison to the RAPID array, the inverse model underestimates the UNADW transport (-9.4 ± 1.9 Sv for the inverse method, -11.1 ± 2.5 Sv for RAPID), and overestimates the LNADW transport (-9.1 ± 5.5 Sv vs -6.0 ± 2.9 Sv), but the total transport of the NADW appears to be very close (-18.5 ± 5.4 Sv vs -17.1 ± 4.0 Sv). The AABW transport is 0.7 ± 2.6 Sv for the inverse method, and 1.0 ± 0.6 Sv for RAPID array, also not significantly different from each other. This comparison shows that provided with time-averaged (annual mean) constraints, the box inverse model is able to reasonably reproduce the observed (RAPID) AMOC strength and structure.

In order to quantify the changes and variability of the AMOC with time, the AMOC strength was calculated using the results of the inverse method, and compared with that of the GECCO2 ocean state estimate (Jan 1985 to Dec 2014), the RAPID array data (Apr 2004 to Oct 2015), and MOVE array data (Feb 2000 to Feb 2016) (Fig. 3.14). *Köhl* (2015) showed that the annual mean overturning stream function calculated from GECCO2 agreed very well with that

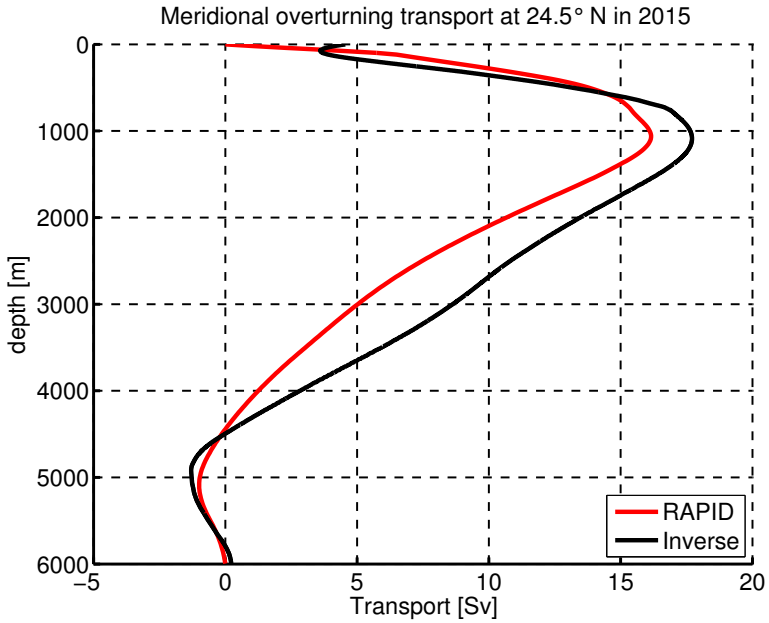

Figure. 3.13 | Meridional overturning transport at 24.5° N in 2015, calculated from the inverse method (black) and RAPID array (red).

from the RAPID array data in the upper 2500 m. In other words, GECCO2 represents the observed AMOC strength very well, as can be seen from the overlapping period between the assimilated (GECCO2) and observed (RAPID) AMOC strength time series (Fig. 3.14a). The overturning strengths of GECCO2 at both latitudes exhibit a strong seasonal cycle, with the maximum transport in boreal winter, and minimum in boreal summer. The seasonal difference of the strength can reach up to 15 Sv. The 20-month low-passed AMOC strength of GECCO2 also reveals interannual variability at both latitudes. For instance, a continuous decline of the AMOC strength between 2008 and 2012 is captured by GECCO2 at both latitudes, which is also observed by the RAPID array. *Smeed et al.* (2014) analysed different components of the AMOC (Ekman transport, western boundary current, mid-ocean geostrophic transport) at 26° N by using the RAPID array, and attributed the observed decline largely to a strengthened southward transport in the upper mid-ocean (less than 1100 m). *McCarthy et al.* (2012) also pointed out that on interannual timescales, the decrease of the AMOC strength was compensated by the strengthening of the horizontal gyre circulation. At the two latitudes, the AMOC strength calculated from the inverse method agrees with the GECCO2/RAPID AMOC strength in the respective years within error bars.

The 120-day low pass filtered MOVE array transport time series at 16° N is shown in Fig. 3.14b, as a representation and update of Fig. 2 in *Send et al.* (2011). The MOVE array is composed of a current meter mooring at the western boundary, and two end-point geostrophic

moorings at each end of the western basin at 16° N, which measures the DWBC and interior geostrophic transport between 1200 and 4950 m in the western basin. An assumption behind this mooring configuration is that the southward flow in the NADW layer in the western basin should represent (almost) entirely the southward return limb of the AMOC, thus the AMOC intensity (*Send et al.*, 2011). Note that the sign of the MOVE transport in Fig. 3.14b is reversed for comparison purpose. In contrast to the good agreement between the AMOC strength calculations from the inverse method, GECCO2, and RAPID at 24.5° N, the AMOC strength from the MOVE array does not seem to align with that of the inverse method and GECCO2 at 14.5° N (Fig. 3.14b). Although the MOVE transport also shows seasonal to interannual variability up to 20 Sv, the magnitude of the MOVE transport (24.1 ± 4.1 Sv) is generally larger than that of GECCO2 at 14.5° N (15.8 ± 3.4 Sv) throughout most of the overlapping period. Additionally, the MOVE transport shows a significant increase trend of 8.4 ± 5.6 Sv decade^{-1} since April 2004 (*Baringer et al.* 2015; by using data from Apr 2004 to Oct 2013 and 95% confidence interval), whilst the RAPID transport has a significant decrease trend of -4.1 ± 3.2 Sv decade^{-1} over the same period. Extending the data to the last available time, the trend at 26° N reduces to -3.0 Sv decade^{-1}, while at 16° N it remains similar 8.2 Sv decade^{-1} (both are significant using two-sided t-test on 95% confidence interval). Since the NADW originates from the subpolar North Atlantic, and is transported southward, any long-term signal observed in the RAPID section should appear later in the MOVE section. Assuming the same transit speed as the water traveling from the Labrador Sea to 26° N (9 years, *van Sebille et al.* 2011), it would take 2-3 years for the same water to reach 16° N (*Smeed et al.*, 2014). However, this does not seem to be the case when comparing results from this two observation systems. Speculations can be made to explain these discrepancies, such as whether the assumption behind the MOVE array that the NADW through the western basin is representative of the whole southward return limb of the AMOC, or whether the reference level of no motion vary with time, etc., are fulfilled. The geostrophic velocity sections at 14.5° N (Fig. 3.12a, c) show northward recirculation over the MAR, which may not be fully resolved by the eastern most mooring of the MOVE array. However, it is impossible to verify whether it is a standing or transient feature based on the available data.

The AMOC strength derived from the GECCO2 state estimate does not show any trend at both latitudes over the presented period. Instead, the seasonal to interannual variability in the monthly and low-passed time series dominates the changes over different time periods. Therefore, we believe that the differences in the AMOC obtained from the inverse method

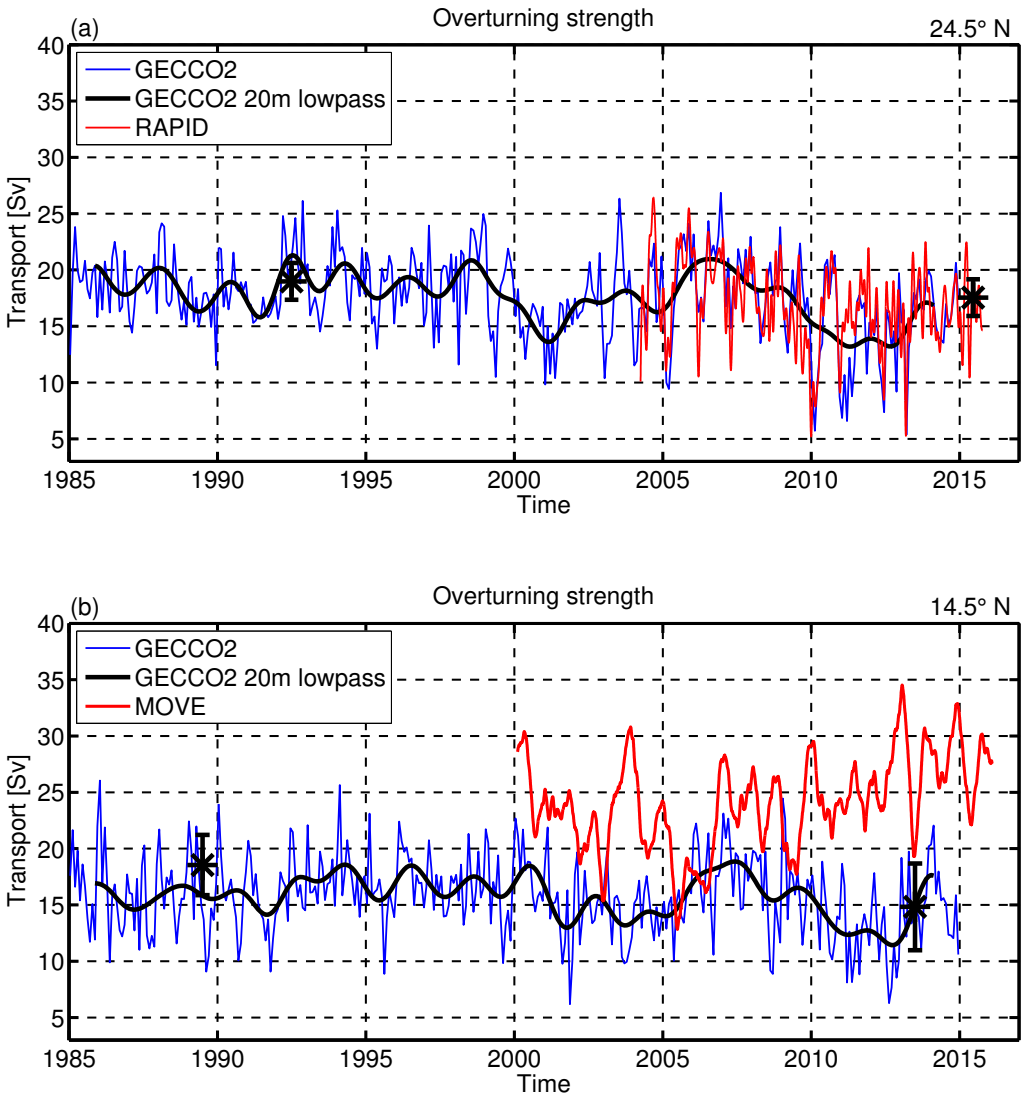

Figure. 3.14 | Meridional overturning strength at (a) 24.5° N and (b) 14.5° N, calculated from the GECCO2 (blue), RAPID (red in a), MOVE (red in b), and inverse method (black stars with error bars for the respective years). The black thick line marks the 20-month low-passed time series of the GECCO2 meridional overturning strength. Note that the MOVE time series represents the southward transport in the NADW layer (1200 to 4950 m) in the western Atlantic basin, and that the sign of the MOVE time series is artificially reversed to ease the comparison.

between the respective realizations at the two latitudes are more likely due to the variability of the AMOC, rather than a long-term weakening or strengthening trend of the circulation.

3.6 Conclusion

In this study, hydrographic data from trans-Atlantic sections at 14.5° N occupied in 1989 and 2013, and at 24.5° N occupied in 1992 and 2015, are presented. Through comparison between the earlier realizations (1989, 1992) and the more recent realizations (2013, 2015)

at the respective latitude, we have shown property changes of water masses over time. At 14.5° N, basin-wide warming and salinification of AAIW on neutral surfaces is observed in the γ_n range between 27.38 and 27.82 kg m^{-3} (Fig. 3.3e and 3.4e). Previous studies have also shown that at 7.5° N in the Atlantic, warming occurred in the intermediate layer (500-2000 m) through comparison of hydrographic data measured in 1957, 1993, and 2000 (*Arhan et al.*, 1998; *Sarafanov et al.*, 2007, 2008), and a significant decrease of the northward AAIW transport at this latitude (*Hernández-Guerra et al.*, 2014). *Schmidtko and Johnson* (2012) further showed warming and salinification trends of the AAIW core in the tropical North Atlantic since the mid-1970s. They attributed the trends in the Atlantic to an increase trend in winter SST in the AAIW formation region, and to a strengthened Agulhas leakage associated with a low SAM during some periods of the 20th century, which imports more warmer and saltier Indian Ocean water to the Atlantic (*Beal et al.*, 2011).

The density of the densest AABW at both latitudes decreased over the studied period, at 14.5° N from 28.1686 kg m^{-3} in 1989 to 28.1623 kg m^{-3} in 2013, and at 24.5° N from 28.1596 kg m^{-3} in 1992 to 28.1540 kg m^{-3} in 2015. This implies that the denser AABW observed previously in the western basin has depleted, and that the lighter AABW type is now present, leading to a downward displacement of the isoneutrals. As a result, differencing θ on pressure levels, we observed an overall warming in the AABW layers with γ_n larger than 28.141 kg m^{-3} at 24.5° N, whilst at 14.5° N a warming at the bottom of the continental slope (west of 55° W, and $\gamma_n > 28.141$ kg m^{-3}). This is consistent with the previous studies by *Johnson et al.* (2008), who illustrated the warming of AABW in the North Atlantic using repeated zonal and meridional sections; and by *Herrford et al.* (2017), who showed that in the equatorial region, the temperature of the coldest AABW increased since the early 1990s.

By applying a box inverse model to the trans-Atlantic sections at 14.5° N and 24.5° N for a 1989/1992 period and a 2013/2015 period, the meridional overturning transport and the horizontal circulation pattern at the two latitudes and in different periods are obtained. The zonally integrated meridional transports per water mass for different realizations at the two latitudes are summarized in Table 3.3. Corresponding to the warming and salinification of the AAIW, we observed that at 14.5° N, the northward intermediate layer transport in 2013 was considerably weaker than in 1989 (Fig. 3.10 and 3.11a). We estimated that the western boundary current transport in 1989 amounted to 27.6 ± 3.2 Sv, partitioned nearly equally into two branches confined in the narrow channel and along the continental slope. In 2013, the western boundary transport amounted to 26.9±3.7 Sv, but was confined almost entirely within

the channel, which is also supported by the LADCP data measured during the 2013 realization. Compared to an estimate of 18-24 Sv by *Klein et al.* (1995), our western boundary current in both realizations is strong, but we believe that their results are biased by an extremely large Ekman transport (15.94 Sv) used in their application of a box inverse model. The Lesser Antilles is located to the west of the 14.5° N section (Fig. 3.1), connecting the Caribbean Sea with the Atlantic. Recent observation and model study suggest that a total flow of 17-19 Sv passes through the Lesser Antilles into the Caribbean Sea (*Kirchner et al.*, 2008), implying that the western boundary current across the 14.5° N section must recirculate southward across the section in the east, as occurs in both realizations (Fig. 3.12a, b).

The DWBC transport at 14.5° N was -22.7 ± 9.6 Sv in 1989 and -17.9 ± 8.0 Sv in 2013, which is in agreement with the previous estimates ranging from -16 to -27 Sv in the tropical North Atlantic (*Speer and McCartney*, 1991; *Molinari et al.*, 1992; *Friedrichs and Hall*, 1993). Different from *Friedrichs and Hall* (1993), we found that the northward recirculation occurred both at the western flank of the MAR, and directly to the east of the southward core along the continental slope. At 24.5° N, the DWBC transport was -26.8 ± 4.6 Sv in 1992 and -25.4 ± 4.1 Sv in 2015, which are ultimately close to the a priori constraint of -26.5 ± 13.5 Sv, and agree with the estimates of -24.2 Sv, -26.5 Sv, and -32 ± 16 Sv by *Bryden et al.* (2005b), *Johns et al.* (2008), and *Meinen et al.* (2013), respectively.

The box inverse model results also show that at both latitudes the AMOC was weaker during 2013/2015 than during 1989/1992, which is consistent with the AMOC strength of the GECCO2 data at 14.5° N and 24.5° N during the corresponding periods. However, long-term records of the AMOC in GECCO2 show strong seasonal to internannual variability, indicating that the observed decrease of AMOC intensity from the inverse method should be due to the variability rather than a long-term weakening trend of the AMOC. The variability of the AMOC may arise from different contributors on different timescales. *Kanzow et al.* (2010) concluded that at 26° N on subseasonal timescales the meridional Ekman transport is the main contributor, while on annual timescales the upper mid-ocean (upper 1100 m excluding the Florida Straits) transport variability, due to seasonal changes of the wind stress curl near the eastern boundary, plays an dominant role. However, *Frajka-Williams et al.* (2016) analysed the RAPID array data of 10-year record, and concluded that the upper mid-ocean variability was mostly counteracted by the FC transport on seasonal timescales, which, as a result, has little influence on the AMOC variability. Instead, it is the variability in the Ekman transport leaving an imprint on the AMOC variability on the same timescales.

The weaker AMOC at 14.5° N and 24.5° N during 2013/2015 in the inverse model was exhibited by a weaker northward thermocline and intermediate water transport, compensated by a correspondingly weaker southward UNDAW transport. Regarding the deep water formation as a primary driver of the AMOC, the long-term variability observed at lower latitudes might be related to changes in the export rate of deep waters in the subpolar North Atlantic. The variability of the NADW transport at 16° N estimated from the MOVE array was attributed to interannual variability in LSW transport (*Send et al.*, 2011). However, studies based on the RAPID array at 26° N show that the variability of the AMOC is more related to the changes in the LNADW transport rather than the UNADW (*McCarthy et al.*, 2012; *Smeed et al.*, 2014), contrary to the MOVE-based conclusion. The discrepancy in the source of the AMOC variability between the two latitudes is still unclear and needs further studies. Observations show that the LNADW source water transport, originating from the Nordic seas, is very stable (*Hansen et al.*, 2016; *Jochumsen et al.*, 2017). Observations also suggest that the formation of Labrador Sea Water, which contribute to the UNADW, is not linked to the DWBC transport in the Labrador Sea (*Zantopp et al.*, 2017). Consequently, variability in NADW formation is not expected to correlate well with the generation and propagation of transport signals in the DWBC.

We also estimated the heat flux through the 14.5° N section as 1.03 ± 0.14 PW in 1989 and 1.11 ± 0.15 PW in 2013. Compared to the estimates of 1.22 or 1.37 PW (annual or seasonal case) using the 1989 realization at 14.5° N by *Klein et al.* (1995), our estimates are considerably smaller. This is mainly due to the anomalously strong Ekman transport applied in their version of box inverse model, as demonstrated in the sensitivity test of the box inverse model to the Ekman transport (cf. Sect. 3.4.3). At 24.5° N, the heat flux was 1.39 ± 0.10 PW in 1992 and 1.12 ± 0.11 PW in 2015, which are consistent with the previous estimates using hydrographic data ranging between 1.2 and 1.4 PW (e.g. *Ganachaud* 2003; *Hernández-Guerra et al.* 2014), and estimates based on the RAPID array of 1.25 ± 0.36 PW (*Johns et al.*, 2011).

As a closing note, we would like to raise some cautions when interpreting the box inverse model results, although we did not claim any long-term change of the AMOC at 14.5° N and 24.5° N. We argued that based on a number of box inverse studies, a time-averaged circulation can be achieved by applying time-averaged initial conditions to the box inverse model (*Ganachaud and Wunsch*, 2000; *Ganachaud*, 2003; *Lumpkin and Speer*, 2003; *Hernández-Guerra et al.*, 2014). However, it is still not possible to rule out any potential influence of the temporal variability of the AMOC captured by the non-synoptic surveys on the inverse

results; after all the two inverse boxes in this study were built on sections occupied in different seasons and different years. Intense seasonality of the equatorial current system and the tropical/subtropical cells would impact the western boundary current and the interior meridional transport. The interannual variability in the deep water formation region would also affect the returning limb of the AMOC. Through a sensitivity test, it is suggested that the hydrographic variations at one section affect the circulation at the other section, and that it is maybe important to perform a box inverse model combining sections occupied in the nearby years (cf. Sect. 3.4.3 for details).

Acknowledgement

This study is supported by the Deutsche Forschungsgemeinschaft as part of cooperative project FOR1740 and by European Union 7th Framework Programme (FP7 2007-2013) under grant agreement 603521 PREFACE project. We thank Thomas Müller for reprocessing the M09 CTD salinity, temperature, and oxygen data, and his comments on a previous version of the manuscript. We thank Toste Tanhua for closing the M96 section towards the African coast during M97. We thank Armin Köhl for providing the GECCO2 data and the information about the data. Special thanks to Takamasa Tsubouchi for his generous help on the box inverse model, as well as to Alonso Hernandez-Guerra for his help on the error estimation of the inverse model results. The inverse model was developed from DOBOX version 4.2 (*Morgan*, 1994). Data from the RAPID-WATCH MOC monitoring project are funded by the Natural Environment Research Council and are freely available from www.rapid.ac.uk/rapidmoc. This work uses data from the MOVE project (see *Kanzow et al.* 2006, DOI:10.1016/j/dsr/2005.12.007). MOVE is a contribution to the international OceanSITES project.

4 Summary

In this thesis, the ageostrophic and geostrophic components of the AMOC in the tropical Atlantic, as well as the associated water mass property changes, were investigated. Hydrographic data, directly measured current velocity data, and ship-board wind speed observations along two trans-Atlantic sections at 14.5° N and 11° S provide valuable information for analysing the vertical and horizontal structure of the ageostrophic flow, and for estimating the meridional Ekman volume, heat, and salt transport across the two sections using different methods. These results set upper-layer ageostrophic constraints for the estimation of the AMOC over the entire water column.

Repeated hydrographic sections along 14.5° N, occupied in 1989 and 2013, and along 24.5° N, occupied in 1992 and 2015, allow a comparison of water mass properties between the different periods. This shows a clear change in the salinity and temperature of the AAIW and AABW. By applying a box inverse model to the two sections, the overturning transport, and the horizontal circulation pattern during 1989/1992 and 2013/2015 were determined. Comparison between the inverse solution and the GECCO2 state estimate, the MOVE and RAPID array analysis gives insight into the changes of the AMOC strength between the two periods. Sensitivity experiments of the box inverse model also reveal the importance of the Ekman transport to the overturning structure as well as the heat transport related to the AMOC.

In the following, the scientific questions raised in Chapter 1 will be answered based on the results presented in the previous chapters.

- What is the vertical structure of meridional ageostrophic flow? What are the Ekman transports across 11° S and 14.5° N? And how deep does the Ekman flow penetrate?

  Meridional ageostrophic velocity was calculated at 14.5° N and 11° S, following *Chereskin and Roemmich* (1991) and *Wijffels et al.* (1994) by subtracting the geostrophic velocity from the meridional component of the ADCP velocity. At both latitudes, the section-averaged ageostrophic velocity shows maxima near the surface. Below the strength of the velocity reduces gradually to about zero at depths of 60 m to 100 m (Fig. 2.3). Such a structure is indicative of the Ekman spiral, and largely agrees with the ageostrophic structure observed at 11° N in the Atlantic (*Chereskin and Roemmich*, 1991), and at 10° N in the Pacific (*Wijffels et al.*, 1994). However, due to the zonal orientation of the sections, only the meridional component of the ageostrophic velocity can be derived,

not a 3-dimensional Ekman spiral. Below the surface layer of the Ekman flow, wave-like structures with vertical length scales of 50-80 m can be detected in the ageostrophic velocity profiles along both sections. Separation of the wave-like signals from the cross-section ADCP velocity shows that these wave-like signals mainly occurred below the TTP and coincide with the layer of maximum buoyancy frequency. They are characterized by vertically alternating meridional velocities with large horizontal coherence. The presence of similar wave structures within the main thermocline was previously documented by *Chereskin and Roemmich* (1991) and are believed to be associated with near-inertial internal waves.

The depth of the TTP is on average about 20 m deeper than the MLD at both latitudes. Integrating the ageostrophic velocity zonally through the section and vertically to the local TTP depth results in Ekman transports of 6.2 ± 2.3 and 11.7 ± 2.1 Sv at 14.5° N and 11° S, respectively. These values agree well with the estimates of 6.7 ± 3.5 and 13.6 ± 3.3 Sv derived by using the in-situ wind stress data. When the ageostrophic velocity is integrated to the local MLD, the Ekman transport is about one-fourth smaller at both sections, indicating that the wind-driven flow penetrates beyond the ML to the TTP. *Wijffels et al.* (1994) also showed that at 10° N in the Pacific the transport in the ML accounted for about two-thirds of the wind-stress-derived Ekman transport and that the TTP captures the total Ekman transport derived from the in-situ wind stress very well. *Chereskin et al.* (2002) further showed that at about 8.5° N in the Indian Ocean the TTP best described the vertical extent of the wind-driven flow. Therefore, together with their findings, it can be concluded that the TTP is a reasonable approximation for the Ekman depth, at least in the tropics.

Note that the Ekman transports presented above were estimated from in-situ data measured during two Atlantic transects. The uncertainty of the estimates is given by considering the aliasing effect of the near-inertial waves during the cruises. However, also the trade winds are expected to vary on seasonal to interannual timescales. Ekman transport estimated from the 6-h NCEP/CFSr wind stress from 2000 to 2011 shows a clear seasonal cycle and interannual variability at both latitudes (7.9 ± 3.5 Sv at 14.5° N and -10.4 ± 3.3 Sv at 11° S; annual climatology ± standard deviation). Therefore, a larger uncertainty should be expected, when the temporal variability of the Ekman transport is taken into account.

- How have the water mass properties in the tropical Atlantic changed over the past two decades?

  Comparison of hydrographic data between 1989 and 2013 shows that the AAIW at 14.5° N became warmer and saltier along neutral surfaces in the neutral density range between 27.38 and 27.82 kg m^{-3} across the basin. This is in agreement with previous observations of AAIW property changes. Through comparison of hydrographic data at 7.5° N measured in 1957, 1993, and 2000, *Sarafanov et al.* (2008) showed that water in the intermediate layer (500-2000 m) became warmer. *Schmidtko and Johnson* (2012) also showed that warming and salinification trends of the AAIW core have dominated the Atlantic basin north of 30° S since the mid-1970s. They attributed the warming trends in the Atlantic to a winter SST increase in the AAIW formation region, and to a strengthened Agulhas leakage associated with a low SAM during some periods of the 20th century, which imports more warmer and saltier Indian Ocean water to the Atlantic (*Beal et al.*, 2011).

  At 14.5° N and 24.5° N, the entire NADW strata have become fresher and cooler on neutral density surfaces between 1989/1992 and 2013/2015. The freshening agrees with previous studies showing the sources of the NADW in the formation region have been freshening since decades (*Dickson et al.*, 2002). Recent study by *Hummels et al.* (2015) indicates a freshening trend of the NADW further downstream at 5° S and 11° S between the periods of 2013-2014 and 2000-2004. the At both sections, AABW can only be found in the abyssal basin west of the MAR. The density of the densest AABW has decreased, at 14.5° N from 28.1686 kg m^{-3} in 1989 to 28.1623 kg m^{-3} in 2013, and at 24.5°N from 28.1596 kg m^{-3} in 1992 to 28.1540 kg m^{-3} in 2015. This implies a depletion of the denser AABW in the western basin, and a presence of the lighter type of AABW, resulting in a downward displacement of the neutral density surfaces. Consequently, if the potential temperature difference is calculated on pressure levels, it shows that at 24.5° N warming occurred all over the AABW layers ($\gamma_n > 28.141$ kg m^{-3}), whilst at 14.5° N warming was confined at the bottom of the continental slope (west of 55° W, and $\gamma_n > 28.141$ kg m^{-3}). The warming observed in this study is consistent with previous studies. *Johnson et al.* (2008) demonstrated the warming of AABW in the North Atlantic using repeated zonal and meridional sections. *Herrford et al.* (2017) also showed that the temperature of the coldest AABW has increased since the early 1990s in the equatorial region.

- Are there circulation changes corresponding to the changes in the water mass properties?

Has the AMOC at 14.5° N and 24.5° N weakened between 1989/1992 and 2013/2015, and how to interpret the changes?

Corresponding to the warmer and saltier AAIW at 14.5° N in 2013 than in 1989, the inverse solution shows a markedly weaker intermediate layer transport in 2013. This indicates that at 14.5° N the circulation changes may be responsible for the AAIW property changes. The weaker northward intermediate layer transport would reduce the northward supply of the AAIW, and consequently increase both salinity and temperature in the AAIW due to longer mixing period with the ambient waters. Corresponding to the warming of the AAIW observed at 7.5° N in the Atlantic (*Sarafanov et al.*, 2008), a significant decrease of the intermediate layer transport at the same latitude between 2011 and 1993 was reported by *Hernández-Guerra et al.* (2014), who also applied the box inverse method to determine the meridional transport. In the bottom layers, although the reduction of the density of the AABW at both latitudes is observed, the inverse solution does not show a significant change of transport in these layers.

At 14.5° N and 24.5° N, the AMOC strength from the inverse solution was weaker during 2013/2015 than during 1989/1992. However, the time series of the AMOC strength estimated using the GECCO2 data does not show any trend, instead, it shows strong seasonal to interannual variability. This implies that the variability of the AMOC is responsible for the observed change of the AMOC strength. On different timescales, the variability of the AMOC may be caused by different contributors. Using the first three years of the RAPID data, *Kanzow et al.* (2010) found that on subseasonal timescales the meridional Ekman transport played a dominant role in the AMOC variability, while on seasonal timescales the main contributor is the upper mid-ocean geostrophic transport (upper 1100 m excluding the Florida Straits), whose variability is induced by seasonal changes of the wind stress curl near the eastern boundary. However, a more recent publication based on 10 years of the RAPID data by *Frajka-Williams et al.* (2016) showed that on seasonal timescales the upper mid-ocean variability and the FC transport counteract with each other, resulting in little net effect on the AMOC variability. Instead, it is the variability in the Ekman transport leaving an imprint on the AMOC variability on the same timescales.

At both latitudes, the Ekman transport was found to be relatively stable between the two time periods. The weaker AMOC during 2013/2015 in the inverse solution was caused by

a weaker northward thermocline and intermediate water transport. Correspondingly, a weaker southward transport in the UNADW layers balanced the reduction of the northward transport in the upper layers. This indicates that if the deep water formation can be regarded as a primary driver of the AMOC, the long-term variability of the AMOC may be related to the export rate of the deep waters in the subpolar region. At 16° N, based on the MOVE array data *Send et al.* (2011) attributed the variability of the NADW transport to the variability in LSW transport. However, studies based on the RAPID array data at 26° N show that the variability of the AMOC is more likely related to the changes in the LNADW transport rather than the UNADW (*McCarthy et al.*, 2012; *Smeed et al.*, 2014). The disagreement in the sources of the AMOC variability between the two observation systems is unclear and requires further investigation.

- How does the Ekman volume transport affect the overturning structure and the total heat transport of the AMOC?

  The sensitivity experiments of the inverse solution to the Ekman transport showed that the upper-ocean transport has an immediate response to the change of Ekman transport. An abrupt increase of the Ekman transport in the surface layer causes a significant decrease of the thermocline and intermediate water transport at 14.5° N. This is consistent with the conclusion drawn from the analysis of the RAPID array data by *Cunningham et al.* (2007), who found that on subseasonal to seasonal timescales, the upper ocean responds to changes in the Ekman transport immediately. By artificially doubling the Ekman transport at 14.5° N in 1989 from 8.8 to 17.6 Sv, the total heat transport across the section increased by about 50% (from 1.03 to 1.50 PW). This is due to the excessive weighting on the warmest surface water in the heat transport calculation. If a similar experiment was conducted at the 24.5° N section, doubling the Ekman transport would increase the total heat transport by about 25%. Together with the conclusion drawn in Chapter 2 that the uncertainty in the Ekman volume transport determines the uncertainty in the Ekman heat transport, it can be concluded that the total heat transport across a section is sensitive to the Ekman volume transport in the tropical Atlantic. As mentioned earlier, the 14.5° N section is located near the maximum climatological meridional Ekman transport in the North Atlantic (Fig. 2.1). The sensitivity experiments suggest that the Ekman transport there plays a more important role in the total heat transport than at other latitudes.

In the calulation of the ageostrophic velocity, the relative geostrophic velocity was calculated independently from the CTD and uCTD datasets, respectively. This is the first application of uCTD data with high horizontal resolution on large scale geostrophic/ageostrophic velocity calculation. After sensor calibration procedure following *Ullman and Hebert* (2014), the uCTD data was quality-controlled in comparison with the CTD and TSG data (cf. Chapter 2.2 for details). The uCTD-based calculation shows consistent Ekman transport estimates with the CTD-based calculation. Given the good cost-efficiency and credible data quality, the application of the uCTD system and its advanced products (e.g. rapidCAST) should be further promoted.

Comparison between the inverse solution, the GECCO2 state estimate, the MOVE and RAPID array analysis revealed strong consistencies but also some discrepancies. In general, the overturning strength calculated from the inverse solution, the GECCO2 and the RAPID array data is in good agreement. However, the MOVE-derived AMOC strength at 16° N is generally larger than that derived from the other datasets, and shows an opposite trend to the GECCO2 or RAPID-derived AMOC strength over the overlapping period (Apr 2004 to Dec 2014). The RAPID-derived AMOC strength time series shows a decreasing trend of -3.0 Sv decade^{-1}, whilst that from the MOVE array shows an increasing trend of 8.2 Sv decade^{-1} (95% confidence interval). Note that the MOVE array is purposefully designed to observe the NADW transport in the western basin between 1200 and 4950 m, which is assumed to entirely capture the returning limb of the AMOC. Since the NADW originates from the subpolar North Atlantic, and is transported southward, any long-term signal observed in the RAPID section should appear later in the MOVE section after a transit time of 2-3 years (*Smeed et al.*, 2014). However, comparison between results from these two observation systems does not meet the expectation. On the one hand, one may question the continuity of a NADW signal from one section to another, as *Lozier* (2012) pointed out the importance of interior pathways for the NADW from the subpolar to the subtropical gyre. This indicates that a water parcel originating from the subpolar region may not be transported directly southward within the DWBC, instead, it may remain on the interior pathways for years before reaching the subtropics. On the other hand, one may also question the capability of the MOVE array to capture transport changes in the eastern basin. As shown in the absolute geostrophic transport sections at 14.5° N (Fig. 3.12), northward recirculation in the NADW layer exists over the MAR, which might not be fully resolved by the easternmost mooring of the MOVE array. The configuration of the MOVE array neglects the transport in the eastern basin, which might, however, be more important than previously thought.

Throughout the thesis, the derivation of the absolute geostrophic velocity is fundamental for calculating the ageostrophic velocity, thus the Ekman transport, as well as for estimating the strength of the AMOC. According to the thermal wind relation, a relative geostrophic velocity relative to a reference level is calculated from the density field measured by the CTD/uCTD. Yet, the determination of the reference velocity at the reference level is the key. Two methods were used to determine the reference geostrophic velocity in this thesis. The first one is by using directly observed velocity from the shipboard ADCPs. This is a straightforward calculation, however, already small instrumental error may result in large transport error if the velocity is integrated over a large depth range. Furthermore, the measured flow may not be in pure geostrophic balance. In the study on the ageostrophic transport of this thesis, the instrumental errors were less important, since only the upper 200 m of the water column were of interest. However, the ageostrophic component in the ADCP velocity complicates the calculation. Previous studies on the ageostrophic transport only used the ADCP velocity at the reference level as the reference velocity (*Chereskin and Roemmich*, 1991; *Wijffels et al.*, 1994; *Chereskin et al.*, 2002; *Garzoli and Molinari*, 2001), but in data presented as part of this thesis ageostrophic wave-like structures exist within the upper 250 m at both latitudes. To overcome this problem, the reference geostrophic velocity was determined by averaging the difference between the relative geostrophic velocity and the ADCP velocity over a common depth range. It is assumed that the ageostrophic component in the ADCP velocity should be averaged to about zero. In this way, the influence of the ageostrophic component on determining the reference geostrophic velocity should be reduced.

The other method is the box inverse method, which is a powerful tool that seeks solution for the reference geostrophic velocity in the frame of property (e.g. volume, heat, salt anomaly) conservation within a closed "box" and layers of the box. It also enables integration of a priori knowledge on the circulation, which facilitates the solution of the system. However, the drawbacks of the box inverse method must be noted. Previous box inverse studies showed that a time-averaged circulation can be achieved, provided time-averaged initial conditions (*Ganachaud and Wunsch*, 2000; *Ganachaud*, 2003; *Lumpkin and Speer*, 2003; *Hernández-Guerra et al.*, 2014). However, it is still not possible to rule out any potential influence of the temporal variability of the AMOC captured by the non-synoptic surveys on the inverse results. In the inverse study of this thesis, two boxes were built on sections occupied in different seasons and different years. In the thermocline and intermediate water layer, the western boundary current and the interior meridional geostrophic transport may be affected by the intense seasonality of the equatorial

current system and the tropical/subtropical cells. The interannual variability in the deep water formation region would also affect the returning limb of the AMOC. Sensitivity tests of the inverse models suggested that the final solution is sensitive to the initial conditions; that the hydrographic variations at one section affect the circulation at the other section; and that it might be important to perform a box inverse model combining sections occupied in the nearby years.

In this thesis, a thorough analysis of the meridional ageostrophic and geostrophic transports in the tropical Atlantic was undertaken using a variety of datasets. It is very encouraging to see that similar results of the ageostrophic (Fig. 2.7) and geostrophic (Fig. 3.14) transports can be obtained using different datasets and different methods. The transport results might be useful for other studies that estimate transports and validate numerical models. The water mass property changes presented in this thesis are in agreement with that of previous studies, especially for the AAIW at 14.5° N, which is probably the northern most section in the Atlantic where AAIW property changes are observed. Property changes in water masses reflect changes in the sources of water masses and/or in circulation patterns, which both may be consequences of large-scale climate change and therefore also influence the global hydrological cycle. These results urge further studies on water masses and ocean circulations for better understanding the climate.

4.1 Outlook

Analysis on water mass properties showed a warming and salinification of the AAIW at 14.5° N between 1989 and 2013. Many studies also confirmed the warming of the AAIW in the past decades (*Sarafanov et al.*, 2007; *Schmidtko and Johnson*, 2012; *Arbic and Owens*, 2001), but few focused on the variability of the AAIW properties at the northern latitudes of the tropical North Atlantic, probably due to lack of continuous observational data. In this thesis, the GECCO2 ocean state estimate has been proven to provide reliable transport estimates of the ageostrophic and geostrophic circulation. Therefore, it might also be expected to reasonably represent the observed water mass properties, since GECCO2 assimilates all available temperature and salinity profile data from the EN3 v2a database (*Ingleby and Huddleston*, 2007).

Fig. 4.1 shows the climatology of salinity, potential temperature, pressure, and potential density at the AAIW core depth in the Atlantic estimated using the monthly GECCO2 data from Jan 1985 to Dec 2014. The AAIW core depth is defined as the depth of the salinity

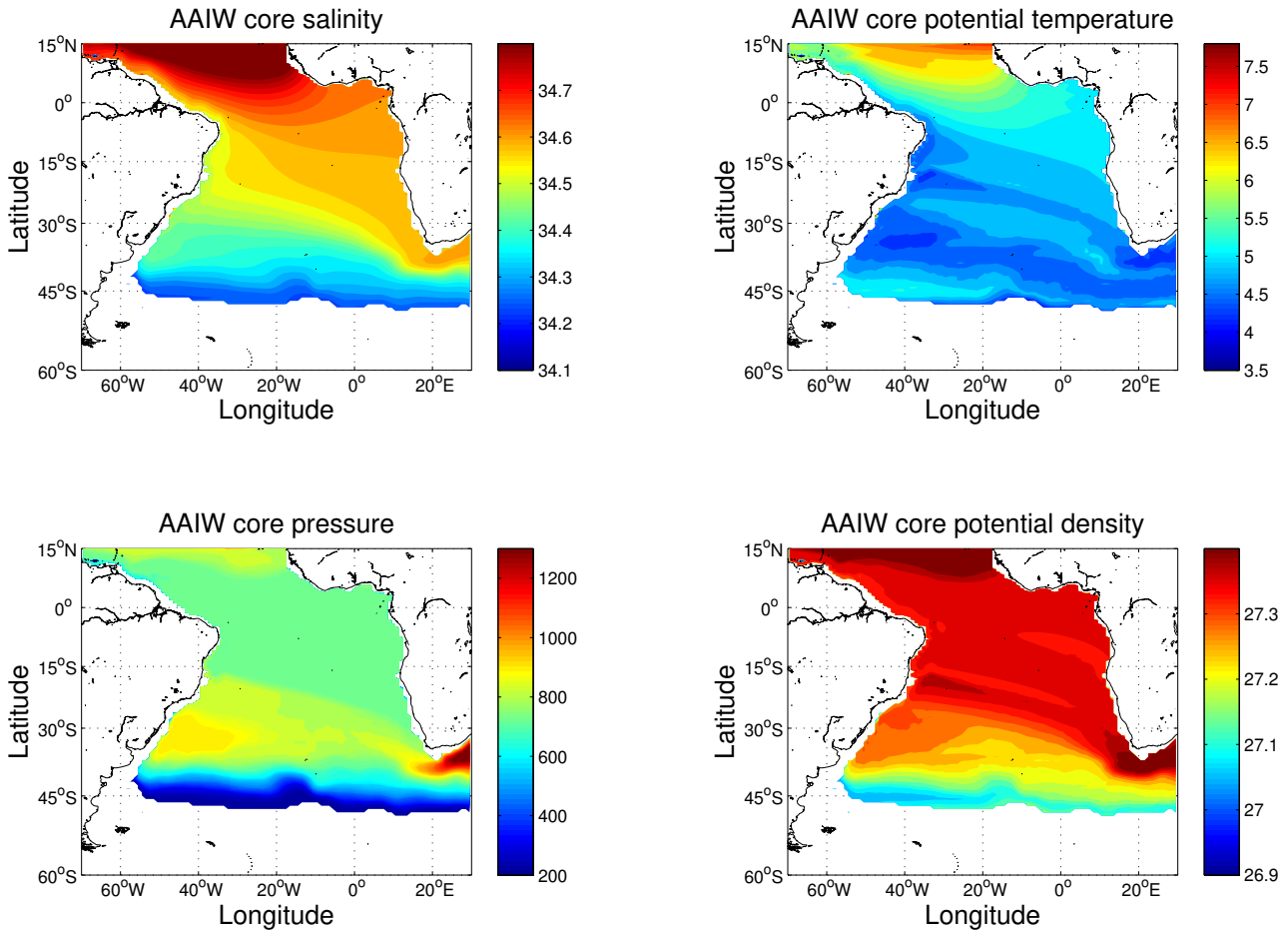

Figure. 4.1 | Climatology of the salinity, potential temperature, pressure, and potential density at the AAIW core, estimated from GECCO2.

minimum in the upper 2000 m. As shown in the core salinity map, on the way of northward spreading, the AAIW core salinity increases through mixing with surrounding waters; in the northern hemisphere the AAIW follows mainly the western boundary pathway, but the impact of more saline AAIW of Indian Ocean origin may be too strong in GECCO2 on the core salinity distribution along the eastern boundary. In the tropical Atlantic, the pressure of the AAIW core is expected to be shallow at the equator and subtropics (670 to 750 dbar), while relatively deep in the tropics away from the equator (750 to 800 dbar) in line with the subtropical gyre dynamics (*Schmid et al.*, 2000; *Schmid and Garzoli*, 2009). However, due to the coarse vertical resolution of GECCO2, the core pressure pattern cannot be adequately resolved. Nevertheless, the GECCO2 AAIW core salinity and temperature climatologies in the tropical North Atlantic are very consistent with those derived from Argo data by *Schmidtko and Johnson* (2012) (Fig. 4 in their work). This increases our confidence to analyse the variability of the AAIW properties in this region using GECCO2 data.

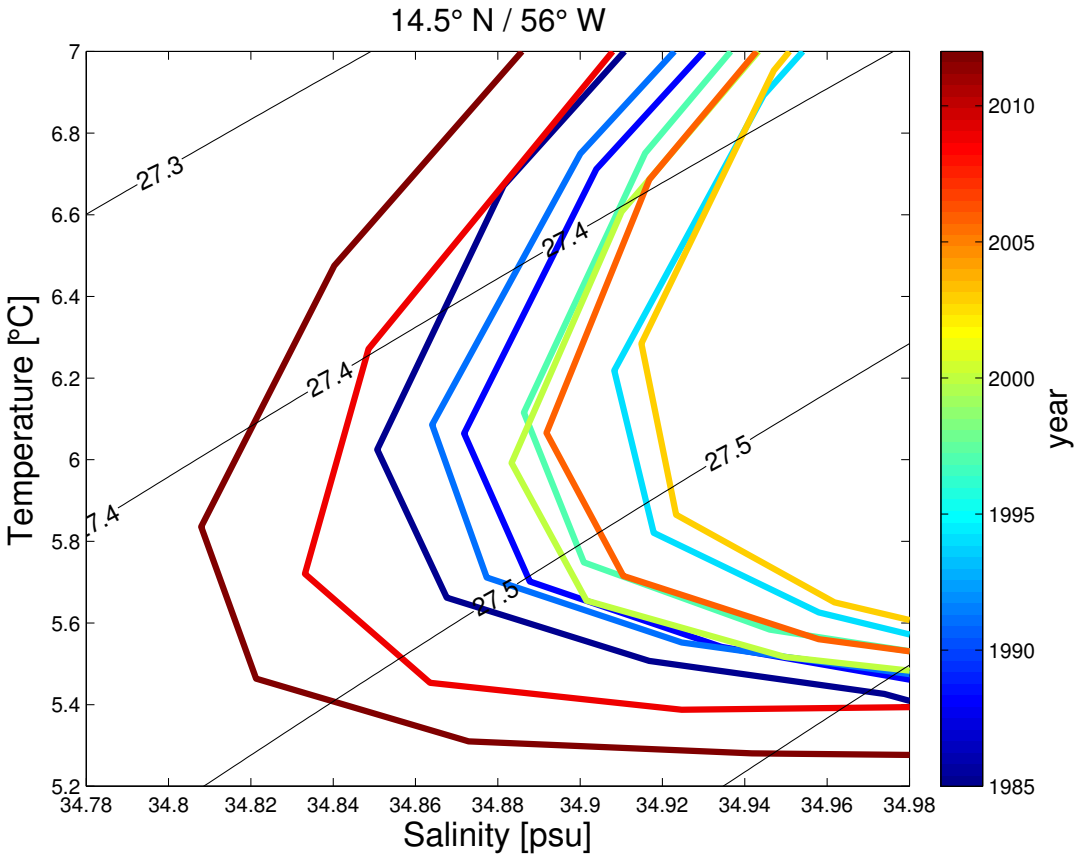

Figure. 4.2 | Annual mean θ/S diagram focusing on the salinity minimum at 14.5° N/56° W in GECCO2, plotted every 3rd year from 1985. The years are marked with different colours.

The annual mean θ/S diagram shows clear interannual variability of θ and S at the AAIW core (Fig. 4.2). In general, the AAIW had become more saline before about 2005, after which a sudden freshening occurred and has continued till recent years. This is a surprising result, since observation at this latitude suggests overall salinification between 1989 and 2013. If this freshening signal was real, which processes would be responsible for the variability at this location? The GECCO2 state estimate should assimilate the Argo float data since 2004. Could this sudden change be a correction of the pre-Argo bias in the GECCO2 data? Zonal and meridional Hovmoeller diagrams of salinity anomaly at the AAIW core (not shown) indicate that the interannual variability at 14.5° N/56° W is introduced from the east and from the south, but it is still not clear what is causing the variability. These questions should be addressed in a follow-up study.

Furthermore, the box inverse method is a universal tool to determine regional or global circulation. It can provide reliable estimates of a mean circulation with error estimates, especially when regions or sections are repeatedly occupied. In recent years, several new trans-basin sections with bottom-reaching CTD profiles in the South Atlantic have been conducted or planned,

for instance cruise MSM60 by R/V Maria S. Merian along the 34.5° S section occupied in January 2017 and a planned cruise M148 by R/V Meteor along 11° S in May/June 2018. The MSM60 expedition was the first basin-wide section in the South Atlantic following the South Atlantic MOC Basin-wide Array (SAMBA) line at 34.5° S (*Meinen et al.*, 2013). During the occupation, full-depth CTD, oxygen, and LADCP measurements, as well as underway measurements including SADCP and high-resolution Expendable Bathythermograph (XBT) were conducted. For the planned M148 expedition at 11° S, full-depth hydrographic and velocity measurements as well as underway velocity measurements will be conducted. Potentially, a box inverse model can be applied to the two sections to determine the meridional volume, heat and freshwater transport across these sections. The transport results at 34.5° S can be compared with the estimates based on the SAMBA. At 11° S, the transport estimates can be compared with the moored observations at the western and eastern boundaries (*Hummels et al.*, 2015; *Kopte et al.*, 2017). Additionally, both sections are close to the historical WOCE sections A10 at 30° S occupied in 1993 and A08 at 11° S occupied in 1994, respectively. The estimated transports and water mass properties from the newly occupied sections can also be compared with previous studies using the A10 and A08 sections (*Lumpkin and Speer*, 2003, 2007). This would provide insights into the AMOC changes and the associated water mass property changes in the South Atlantic.

In addition, as shown in Fig. 2.3 and 2.4, vertical wave structures were observed in the meridional component of the SADCP velocity. These structures are thought to be associated with near-inertial internal waves, but could not be verified from underway observations. Moored velocity measurements may help addressing this problem. A mooring located near the Cape Verde Islands at 17.6° N, 24.3° W, is equipped with an upward looking ADCP at about 120 m, which continuously measures velocity between the surface and 90 m depth. By applying a bandpass filter of near-inertial frequency at this latitude, the near-inertial motions can be separated from the total velocity, allowing identification of periods with near-inertial activities. It is of interest to see whether wave-like structures similar to that in the SADCP velocity can be observed in some periods of the mooring velocity records. Moreover, if the moored ADCP data are combined with satellite-based wind stress, SST, SSS, and sea level anomaly data, as well as Argo float profile data in that region, it may increase the potential to analyse the characteristics of near-inertial motions in detail.

References

Alford, M. H. (2003), Improved global maps and 54-year history of wind-work on ocean inertial motions, *Geophysical Research Letters*, *30*(8), 1–4, doi:10.1029/2002GL016614. 28

Arbic, B. K., and W. B. Owens (2001), Climatic warming of Atlantic intermediate waters, *Journal of Climate*, *14*(20), 4091–4108, doi:10.1175/1520-0442(2001)014⟨4091:CWOAIW⟩2.0.CO;2. 22, 109

Arhan, M., H. Mercier, B. Bourlès, and Y. Gouriou (1998), Hydrographic sections across the Atlantic at 730N and 430S, *Deep-Sea Research Part I: Oceanographic Research Papers*, *45*(6), 829–872, doi:10.1016/S0967-0637(98)00001-6. 98

Atkinson, C. P., H. L. Bryden, J. J. M. Hirschi, and T. Kanzow (2010), On the seasonal cycles and variability of Florida Straits, Ekman and Sverdrup transports at 26 N in the Atlantic Ocean, *Ocean Science*, *6*(4), 837–859, doi:10.5194/os-6-837-2010. 17, 75, 88

Atkinson, C. P., H. L. Bryden, S. A. Cunningham, and B. A. King (2012), Atlantic transport variability at 25 N in six hydrographic sections, *Ocean Science*, *8*(4), 497–523, doi:10.5194/os-8-497-2012. 12, 61, 63

Baringer, M. O., and J. C. Larsen (2001), Sixteen years of Florida current transport at 27 N, *Geophysical Research Letters*, *28*(16), 3179–3182, doi:10.1029/2001GL013246. 75

Baringer, M. O., et al. (2015), Meridional Overturning Circulation Observations in the North Atlantic, *Bull. Amer. Meteor. Soc.*, *96*(7), S78–S80. 15, 60, 96

Beal, L. M., W. P. M. De Ruijter, A. Biastoch, and R. Zahn (2011), On the role of the Agulhas system in ocean circulation and climate., *Nature*, *472*(7344), 429–36, doi:10.1038/nature09983. 98, 104

Biastoch, A., C. W. Böning, J. Getzlaff, J.-M. Molines, and G. Madec (2008), Causes of InterannualDecadal Variability in the Meridional Overturning Circulation of the Midlatitude North Atlantic Ocean, *Journal of Climate*, *21*(24), 6599–6615, doi:10.1175/2008JCLI2404.1. 16

Böning, C. W., E. Behrens, A. Biastoch, K. Getzlaff, and J. L. Bamber (2016), Emerging impact of Greenland meltwater on deepwater formation in the North Atlantic Ocean, *Nature Geoscience*, *9*(7), 523–527, doi:10.1038/ngeo2740. 17

Brandt, P., et al. (2015), On the role of circulation and mixing in the ventilation of oxygen minimum zones with a focus on the eastern tropical North Atlantic, *Biogeosciences*, *12*(2), 489–512, doi:10.5194/bg-12-489-2015. 20, 68

Brayshaw, D. J., T. Woolings, and M. Velling (2009), Tropical and extratropical responses of the North Atlantic atmospheric circulation to a sustained weakening of the MOC, *Journal of Climate*, *22*(11), 3146–3155, doi:10.1175/2008JCLI2594.1. 9

Bryden, H. L., and M. M. Hall (1980), Heat Transport by Currents Across 25 N Latitude in the Atlantic Ocean, *Science*, *207*(4433), 884–886, doi:10.1126/science.207.4433.884. 11

Bryden, H. L., H. R. Longworth, and S. A. Cunningham (2005a), Slowing of the Atlantic meridional overturning circulation at 25N, *Nature*, *438*(7068), 655–657, doi:10.1038/nature04385. 12

Bryden, H. L., W. E. Johns, and P. Saunders (2005b), Deep western boundary current east of Abaco: mean structure and transport, *Journal of Marine Research*, *63*, 35–57, doi:10.1357/0022240053693806. 75, 99

Bryden, H. L., B. A. King, and G. D. McCarthy (2011), South Atlantic overturning circulation at 24S, *Journal of Marine Research*, *69*(1), 39–56, doi:10.1357/002224011798147633. 11

Buckley, M. W., and J. Marshall (2016), Observations, inferences, and mechanisms of the Atlantic Meridional Overturning Circulation variability: A review, *Reviews of Geophysics*, *54*(1), 5–63, doi:10.1002/2015RG000493. 16

Chang, Y. S., S. Zhang, A. Rosati, T. L. Delworth, and W. F. Stern (2013), An assessment of oceanic variability for 1960-2010 from the GFDL ensemble coupled data assimilation, *Climate Dynamics*, *40*(3-4), 775–803, doi:10.1007/s00382-012-1412-2. 16

Chereskin, T. K. (1995), Direct evidence for an Ekman balance in the California Current, *Journal of Geophysical Research*, *100*(C9), 18,261, doi:10.1029/95JC02182. 50

Chereskin, T. K., and D. Roemmich (1991), A Comparison of Measured and Wind-derived Ekman Transport at 11 N in the Atlantic Ocean, *Journal of Physical Oceanography*, *21*, 869–878. 17, 18, 27, 28, 29, 38, 45, 47, 48, 49, 54, 55, 56, 102, 103, 108

Chereskin, T. K., W. D. Wilson, H. L. Bryden, A. Ffield, and J. Morrison (1997), Observations of the Ekman balance at 830 N in the Arabian Sea during the 1995 southwest monsoon, doi:10.1029/97GL01057. 18, 28, 37, 54

Chereskin, T. K., W. D. Wilson, and L. M. Beal (2002), The Ekman temperature and salt fluxes at 830N in the Arabian Sea during the 1995 southwest monsoon, *Deep Sea Research Part II: Topical Studies in Oceanography*, *49*(7-8), 1211–1230, doi:10.1016/S0967-0645(01)00168-0. 18, 26, 38, 40, 53, 103, 108

Collins, M., et al. (2013), Long-term Climate Change: Projections, Commitments and Irreversibility, *Climate Change 2013: The Physical Science Basis. Contribution of Working Group I to the Fifth Assessment Report of the Intergovernmental Panel on Climate Change*, pp. 1029–1136, doi:10.1017/CBO9781107415324.024. 9, 17

Cunningham, S. A., et al. (2007), Temporal Variability of the Atlantic Meridional Overturning Circulation at 26.5 N, *317*(August), 935–938. 14, 17, 26, 60, 106

Defant, A. (1941), Die absolute Topographie des physikalischen Meeresniveaus und der Drückflachen sowie die Wasserbewegungen im Raum des Atlantischen Ozeans, in *Wissenschaftliche Ergebnisse der Deutschen*

Atlantischen Expedition auf dem Forschungs- und Vermessungsschiff "Meteor" 1925-27, vol. 6, pp. 191–260, Berlin. 10

Dengler, M., and D. Quadfasel (2002), Equatorial deep jets and abyssal mixing in the Indian Ocean, *Journal of Physical Oceanography*, *32*(4), 1165–1180. 78, 79

Dickson, B., I. Yashayaev, J. Meincke, B. Turrell, S. Dye, and J. Holfort (2002), Rapid freshening of the deep North Atlantic Ocean over the past four decades, *Nature*, *416*(6883), 832–837, doi:10.1038/416832a. 22, 71, 104

Egbert, G. D., and S. Y. Erofeeva (2002), Efficient inverse modeling of barotropic ocean tides, *Journal of Atmospheric and Oceanic Technology*, *19*(2), 183–204, doi:10.1175/1520-0426(2002)019⟨0183:EIMOBO⟩2.0.CO;2. 78

Ekman, V. W. (1905), On the influence of the earth's rotation on ocean-currents, *Astronomy of Physics*, *2*(11). 17, 25, 27

Elipot, S., and S. T. Gille (2009), Estimates of wind energy input to the Ekman layer in the Southern Ocean from surface drifter data, *Journal of Geophysical Research: Oceans*, *114*(6), 1–14, doi:10.1029/2008JC005170. 28

Fairall, C. W., E. F. Bradley, J. E. Hare, A. A. Grachev, and J. B. Edson (2003), Bulk parameterization of air-sea fluxes: Updates and verification for the COARE algorithm, *Journal of Climate*, *16*(4), 571–591, doi:10.1175/1520-0442(2003)016⟨0571:BPOASF⟩2.0.CO;2. 35

Fischer, J., and M. Visbeck (1993), Deep Velocity Profiling with Sel-contained ADCPs, *Journal of Atmospheric and Oceanic Technology*, *10*, 764–773. 63

Fischer, J., P. Brandt, M. Dengler, M. Müller, and D. Symonds (2003), Surveying the Upper Ocean with the Ocean Surveyor: A New Phased Array Doppler Current Profiler, *Journal of Atmospheric and Oceanic Technology*, *20*(5), 742–751, doi:10.1175/1520-0426(2003)20⟨742:STUOWT⟩2.0.CO;2. 35, 63

Fraile-Nuez, E., F. Machín, P. Vélez-Belchí, F. López-Laatzen, R. Borges, V. Benítez-Barrios, and A. Hernández-Guerra (2010), Nine years of mass transport data in the eastern boundary of the North Atlantic Subtropical Gyre, *Journal of Geophysical Research*, *115*(C9), C09,009, doi:10.1029/2010JC006161. 71

Frajka-Williams, E., et al. (2016), Compensation between meridional flow components of the Atlantic MOC at 26 N, *Ocean Science*, *12*(2), 481–493, doi:10.5194/os-12-481-2016. 14, 15, 99, 105

Friedrichs, M. a. M., and M. M. Hall (1993), Deep circulation in the tropical North Atlantic, *Journal of Marine Research*, *51*(4), 697–736, doi:10.1357/0022240933223909. 9, 18, 26, 82, 90, 93, 99

Fu, Y., J. Karstensen, and P. Brandt (2017), On the meridional ageostrophic transport in the tropical Atlantic, *Ocean Science*, *13*(4), 531–549, doi:10.5194/os-13-531-2017. 60, 61, 78, 82, 88, 92

Ganachaud, A. (2003), Large-scale mass transports, water mass formation, and diffusivities estimated from World Ocean Circulation Experiment (WOCE) hydrographic data, *Journal of Geophysical Research*, *108*(C7), 3213, doi:10.1029/2002JC001565. 11, 13, 39, 60, 61, 73, 79, 80, 83, 87, 93, 100, 108

Ganachaud, A., and C. Wunsch (2000), Improved estimates of global ocean circulation, heat transport and mixing from hydrographic data., *Nature*, *408*(6811), 453–7, doi:10.1038/35044048. 11, 12, 13, 60, 77, 79, 100, 108

Garzoli, S. L., and M. O. Baringer (2007), Meridional heat transport determined with expandable bathythermographsPart II: South Atlantic transport, *Deep Sea Research Part I: Oceanographic Research Papers*, *54*(8), 1402–1420, doi:10.1016/j.dsr.2007.04.013. 11

Garzoli, S. L., and R. L. Molinari (2001), Ageostrophic transport in the upper layers of the tropical Atlantic Ocean, *Geophysical research letters*, *28*(24), 4619–4622. 17, 27, 28, 29, 37, 56, 108

Gill, A. E. (1982), *Atmosphere-Ocean Dynamics*, 662 pp., Academic Press. 9

Hall, M. M., and H. L. Bryden (1982), Direct estimates and mechanisms of ocean heat transport, *Deep Sea Research Part A. Oceanographic Research Papers*, *29*(3), 339–359, doi:10.1016/0198-0149(82)90099-1. 9

Hansen, B., K. M. Husgaro, H. Hátún, and S. Østerhus (2016), A stable Faroe Bank Channel overflow 1995-2015, *Ocean Science*, *12*(6), 1205–1220, doi:10.5194/os-12-1205-2016. 100

Hernández-Guerra, A., E. Fraile-Nuez, R. Borges, F. López-Laatzen, P. Vélez-Belchí, G. Parrilla, and T. J. Müller (2003), Transport variability in the Lanzarote passage (eastern boundary current of the North Atlantic subtropical Gyre), *Deep-Sea Research Part I: Oceanographic Research Papers*, *50*(2), 189–200, doi:10.1016/S0967-0637(02)00163-2. 71

Hernández-Guerra, A., E. Fraile-Nuez, F. López-Laatzen, A. Martínez, G. Parrilla, and P. Vélez-Belchí (2005), Canary Current and North Equatorial Current from an inverse box model, *Journal of Geophysical Research*, *110*(C12), C12,019, doi:10.1029/2005JC003032. 71

Hernández-Guerra, A., T. M. Joyce, E. Fraile-Nuez, and P. Vélez-Belchí (2010), Using Argo data to investigate the Meridional Overturning Circulation in the North Atlantic, *Deep-Sea Research Part I: Oceanographic Research Papers*, *57*(1), 29–36, doi:10.1016/j.dsr.2009.10.003. 12

Hernández-Guerra, A., J. L. Pelegrí, E. Fraile-Nuez, V. Benítez-Barrios, M. Emelianov, M. D. Pérez-Hernández, and P. Vélez-Belchí (2014), Meridional overturning transports at 7.5N and 24.5N in the Atlantic Ocean during 199293 and 201011, *Progress in Oceanography*, *128*, 98–114, doi:10.1016/j.pocean.2014.08.016. 12, 13, 61, 64, 73, 75, 76, 77, 80, 83, 87, 93, 98, 100, 105, 108

Herrford, J., P. Brandt, and W. Zenk (2017), Property changes of deep and bottom waters in the Western Tropical Atlantic, *Deep Sea Research Part I: Oceanographic Research Papers*, *124*(February 2016), 103–125, doi:10.1016/j.dsr.2017.04.007. 22, 72, 98, 104

Hood, E. M., C. L. Sabine, and B. M. Sloyan (2010), The GO-SHIP Repeat Hydrography Manual: A Collection of Expert Reports and Guidelines, *Tech. Rep. 14*. 31

Hummels, R., P. Brandt, M. Dengler, J. Fischer, M. Araujo, D. Veleda, and J. V. Durgadoo (2015), Interannual to decadal changes in the western boundary circulation in the Atlantic at 11S, *Geophysical Research Letters*, *42*(18), 7615–7622, doi:10.1002/2015GL065254. 22, 104, 112

Ingleby, B., and M. Huddleston (2007), Quality control of ocean temperature and salinity profiles - Historical and real-time data, *Journal of Marine Systems*, *65*(1-4 SPEC. ISS.), 158–175, doi:10.1016/j.jmarsys.2005.11.019. 109

Jacob, D., H. Goettel, J. Jungclaus, M. Muskulus, R. Podzun, and J. Marotzke (2005), Slowdown of the thermohaline circulation causes enhanced maritime climate influence and snow cover over Europe, *Geophysical Research Letters*, *32*(21), 1–5, doi:10.1029/2005GL023286. 9

Jayne, S. R., and J. Marotzke (2001), The dynamics of ocean heat transport variability, *Reviews of Geophysics*, *39*(3), 385–411, doi:10.1029/2000RG000084. 16

Jochumsen, K., M. Moritz, N. Nunes, D. Quadfasel, K. M. H. Larsen, B. Hansen, H. Valdimarsson, and S. Jonsson (2017), Revised transport estimates of the Denmark Strait overflow, *Journal of Geophysical Research: Oceans*, *122*(4), 3434–3450, doi:10.1002/2017JC012803. 100

Johns, W. E., L. M. Beal, M. O. Baringer, J. Molina, S. A. Cunningham, T. Kanzow, and D. Rayner (2008), Variability of shallow and deep western boundary currents off the Bahamas during 200405: results from the 26N RAPIDMOC Array, *Journal of Physical Oceanography*, *38*(3), 605–623, doi:10.1175/2007JPO3791.1. 75, 99

Johns, W. E., et al. (2011), Continuous, Array-Based Estimates of Atlantic Ocean Heat Transport at 26.5N, *Journal of Climate*, *24*(10), 2429–2449, doi:10.1175/2010JCLI3997.1. 9, 93, 100

Johnson, G. C., S. G. Purkey, and J. M. Toole (2008), Reduced Antarctic meridional overturning circulation reaches the North Atlantic Ocean, *Geophysical Research Letters*, *35*(22), L22,601, doi:10.1029/2008GL035619. 21, 22, 72, 98, 104

Kanzow, T., U. Send, W. Zenk, A. D. Chave, and M. Rhein (2006), Monitoring the integrated deep meridional flow in the tropical North Atlantic: Long-term performance of a geostrophic array, *Deep-Sea Research Part I: Oceanographic Research Papers*, *53*(3), 528–546, doi:10.1016/j.dsr.2005.12.007. 15, 101

Kanzow, T., U. Send, and M. McCartney (2008), On the variability of the deep meridional transports in the tropical North Atlantic, *Deep-Sea Research Part I: Oceanographic Research Papers*, *55*(12), 1601–1623, doi:10.1016/j.dsr.2008.07.011. 15, 60

Kanzow, T., et al. (2010), Seasonal Variability of the Atlantic Meridional Overturning Circulation at 26.5N, *Journal of Climate*, *23*(21), 5678–5698, doi:10.1175/2010JCLI3389.1. 12, 14, 17, 26, 60, 99, 105

Kinzel, J., K. Fennig, M. Schröder, A. Andersson, K. Bumke, and R. Hollmann (2016), Decomposition of Random Errors Inherent to HOAPS-3.2 Near-Surface Humidity Estimates Using Multiple Triple Collocation Analysis, *Journal of Atmospheric and Oceanic Technology*, *33*(7), 1455–1471, doi:10.1175/JTECH-D-15-0122.1. 76

Kirchner, K., M. Rhein, C. Mertens, C. W. Böning, and S. Hüttl (2008), Observed and modeled meridional overturning circulation related flow into the Caribbean, *Journal of Geophysical Research: Oceans*, *113*(3), 1–9, doi:10.1029/2007JC004320. 99

Kirchner, K., M. Rhein, S. Hüttl-Kabus, and C. W. Böning (2009), On the spreading of South Atlantic Water into the Northern Hemisphere, *Journal of Geophysical Research*, *114*(C5), C05,019, doi:10.1029/2008JC005165. 20, 68

Klein, B. (1992), Die Kapverden-Frontalzone, *Berichte Inst. f. Meereskunde, Kiel, 227*. 63

Klein, B., R. L. Molinari, T. J. Müller, and G. Siedler (1995), A transatlantic section at 14.5N: Meridional volume and heat fluxes, *Journal of Marine Research*, *53*(6), 929–957, doi:10.1357/0022240953212963. 9, 11, 21, 26, 61, 62, 64, 68, 71, 72, 77, 88, 91, 92, 99, 100

Köhl, A. (2015), Evaluation of the GECCO2 ocean synthesis: transports of volume, heat and freshwater in the Atlantic, *Quarterly Journal of the Royal Meteorological Society*, *141*(686), 166–181, doi:10.1002/qj.2347. 16, 35, 76, 94

Kopte, R., P. Brandt, M. Dengler, P. C. M. Tchipalanga, M. Macuéria, and M. Ostrowski (2017), The Angola Current: Flow and hydrographic characteristics as observed at 11S, *Journal of Geophysical Research: Oceans*, *122*(2), 1177–1189, doi:10.1002/2016JC012374. 112

Large, W. G., and S. Pond (1981), Open Ocean Momentum Flux Measurements in Moderate to Strong Winds, *Journal of Physical Oceanography*, *11*(3), 324–336, doi:10.1175/1520-0485(1981)011⟨0324:OOMFMI⟩2.0.CO;2. 47

Large, W. G., and S. G. Yeager (2004), Diurnal to decadal global forcing for ocean and sea–ice models: {The} data sets and flux climatologies., *NCAR Tech. Note*, *TN–460+ST*(May), 105pp, doi:10.5065/D6KK98Q6. 35, 36, 46

Larson, N., and M. Pedersen (1996), Temperature measurements in flowing water: Viscous heating of sensor tips, *Proceedings of the First IGHEM Meeting, Montreal, QC, Canada, IGHEM*. 32

Latif, M., et al. (2004), Reconstructing, Monitoring, and Predicting Multidecadal-Scale Changes in the North Atlantic Thermohaline Circulation with Sea Surface Temperature, *Journal of Climate*, *17*(7), 1605–1614, doi:10.1175/1520-0442(2004)017⟨1605:RMAPMC⟩2.0.CO;2. 16

Lenn, Y.-D., and T. K. Chereskin (2009), Observations of Ekman Currents in the Southern Ocean, *Journal of Physical Oceanography*, *39*(3), 768–779, doi:10.1175/2008JPO3943.1. 50

Levitus, S. (1987), Meridional Ekman Heat Fluxes for the World Ocean and Individual Ocean Basins, *Journal of Physical Oceanography*, *17*(9), 1484–1492, doi:10.1175/1520-0485(1987)017⟨1484:MEHFFT⟩2.0.CO;2. 40, 53

Locarnini, R. A., et al. (2013), World Ocean Atlas 2013. Vol. 1: Temperature., *Tech. Rep. September*, doi: 10.1182/blood-2011-06-357442. 39

Lozier, M. S. (2012), Overturning in the North Atlantic, *Annual Review of Marine Science*, *4*(1), 291–315, doi:10.1146/annurev-marine-120710-100740. 9, 19, 107

Lueck, R. G., and J. J. Picklo (1990), Thermal Inertia of Conductivity Cells: Observations with a Sea-Bird Cell, doi:10.1175/1520-0426(1990)007⟨0756:TIOCCO⟩2.0.CO;2. 32

Lumpkin, R., and K. Speer (2003), Large-Scale Vertical and Horizontal Circulation in the North Atlantic Ocean, *Journal of Physical Oceanography*, *33*(9), 1902–1920, doi:10.1175/1520-0485(2003)033⟨1902:LVAHCI⟩2.0.CO;2. 11, 12, 13, 60, 61, 80, 87, 100, 108, 112

Lumpkin, R., and K. Speer (2007), Global Ocean Meridional Overturning, *J. Phys. Oceanogr.*, *37*(10), 2550–2562, doi:10.1175/JPO3130.1. 11, 12, 112

Lumpkin, R., K. G. Speer, and K. P. Koltermann (2008), Transport across 48N in the Atlantic Ocean, *Journal of Physical Oceanography*, *38*(4), 733–752, doi:10.1175/2007JPO3636.1. 12

Lux, M., H. Mercier, and M. Arhan (2001), Interhemispheric exchanges of mass and heat in the Atlantic Ocean in JanuaryMarch 1993, *Deep Sea Research Part I: Oceanographic Research Papers*, *48*(3), 605–638, doi:10.1016/S0967-0637(00)00033-9. 11

Luyten, J. R., J. Pedlosky, and H. Stommel (1983), The Ventilated Thermocline, *Journal of Physical Oceanography*, *13*(2), 292–309, doi:10.1175/1520-0485(1983)013⟨0292:TVT⟩2.0.CO;2. 68

Macdonald, A. M. (1998), The global ocean circulation: A hydrographic estimate and regional analysis, *Progress in Oceanography*, *41*(3), 281–382, doi:10.1016/S0079-6611(98)00020-2. 60

Machín, F., and J. L. Pelegrí (2009), Northward Penetration of Antarctic Intermediate Water off Northwest Africa, *Journal of Physical Oceanography*, *39*(3), 512–535, doi:10.1175/2008JPO3825.1. 71

Machín, F., J. L. Pelegrí, E. Fraile-Nuez, P. Vélez-Belchí, F. López-Laatzen, and A. Hernández-Guerra (2010), Seasonal Flow Reversals of Intermediate Waters in the Canary Current System East of the Canary Islands, *Journal of Physical Oceanography*, *40*(8), 1902–1909, doi:10.1175/2010JPO4320.1. 71

Mason, E., F. Colas, J. Molemaker, A. F. Shchepetkin, C. Troupin, J. C. McWilliams, and P. Sangrà (2011), Seasonal variability of the Canary Current: A numerical study, *Journal of Geophysical Research: Oceans*, *116*(6), 1–20, doi:10.1029/2010JC006665. 47

McCarthy, G., et al. (2012), Observed interannual variability of the Atlantic meridional overturning circulation at 26.5N, *Geophysical Research Letters*, *39*(19), 1–5, doi:10.1029/2012GL052933. 14, 17, 26, 60, 95, 100, 106

McCarthy, G. D., et al. (2015), Measuring the Atlantic Meridional Overturning Circulation at 26N, *Progress in Oceanography*, *130*, 91–111, doi:10.1016/j.pocean.2014.10.006. 18, 26, 40

McCartney, M. S., S. L. Bennett, and M. E. Woodgate-Jones (1991), Eastward flow through the Mid-Atlantic Ridge at 11N and its influence on the abyss of the eastern basin, doi:10.1175/1520-0485(1991)021⟨1089:EFTTMA⟩2.0.CO;2. 21, 72

McCreary, J. P., and P. Lu (1994), Interaction between the Subtropical and Equatorial Ocean Circulations: The Subtropical Cell, *Journal of Physical Oceanography*, *24*(2), 466–497, doi:10.1175/1520-0485(1994)024⟨0466:IBTSAE⟩2.0.CO;2. 68

McDonagh, E. L., B. A. King, H. L. Bryden, P. Courtois, Z. Szuts, M. Baringer, S. A. Cunningham, C. Atkinson, and G. McCarthy (2015), Continuous Estimate of Atlantic Oceanic Freshwater Flux at 26.5N, *Journal of Climate*, *28*(22), 8888–8906, doi:10.1175/JCLI-D-14-00519.1. 18, 26, 82, 93

McDougall, T. J., and P. M. Barker (2011), Getting started with TEOS10 and the Gibbs Seawater (GSW) Oceanographic Toolbox, *Intergovernmental Oceanographic Commission Rep.*, (June), 28. 34

McIntosh, P. C., and S. R. Rintoul (1997), Do Box Inverse Models Work?, *Journal of Physical Oceanography*, *27*(2), 291–308, doi:10.1175/1520-0485(1997)027⟨0291:DBIMW⟩2.0.CO;2. 73, 91

Meinen, C. S., M. O. Baringer, and R. F. Garcia (2010), Florida Current transport variability: An analysis of annual and longer-period signals, *Deep Sea Research Part I: Oceanographic Research Papers*, *57*(7), 835–846, doi:10.1016/j.dsr.2010.04.001. 75

Meinen, C. S., W. E. Johns, S. L. Garzoli, E. van Sebille, D. Rayner, T. Kanzow, and M. O. Baringer (2013), Variability of the Deep Western Boundary Current at 26.5N during 2004-2009, *Deep-Sea Research Part II: Topical Studies in Oceanography*, *85*, 154–168, doi:10.1016/j.dsr2.2012.07.036. 75, 99, 112

Merz, A. (1925), Die Deutsche Atlantische Expedition auf dem Vermessungs- und Forschungsschiff "Meteor". 1. Bericht. Sitzungsberichte der Preussischen Akademie der Wissenschaften, *Physikalische-Mathematische Klasse*, pp. 562–586. 19

Molinari, R. L., R. A. Fine, and E. Johns (1992), The Deep Western Boundary Current in the tropical North Atlantic Ocean, *Deep Sea Research Part A. Oceanographic Research Papers*, *39*(11-12), 1967–1984, doi:10.1016/0198-0149(92)90008-H. 64, 89, 90, 91, 99

Montgomery, R. B. (1974), Comments on "Seasonal variability of the Florida Current", by Niiler and Richardson, *Journal of Marine Research*, *32*, 533–535. 39

Morgan, P. (1994), Box Inverse Modelling with Dobox 4.2, *CSIRO Marine Laboratories Report*, (225), 26. 101

Owens, W. B., and R. C. Millard (1985), A New Algorithm for CTD Oxygen Calibration, *Journal of Physical Oceanography*, *15*(5), 621–631, doi:10.1175/1520-0485(1985)015⟨0621:ANAFCO⟩2.0.CO;2. 62

Pérez-Hernández, M. D., G. D. McCarthy, P. Vélez-Belchí, D. A. Smeed, E. Fraile-Nuez, and A. Hernández-Guerra (2015), The Canary Basin contribution to the seasonal cycle of the Atlantic Meridional Overturning Circulation at 26N, *Journal of Geophysical Research: Oceans*, *120*(11), 7237–7252, doi:10.1002/2015JC010969. 47

Pickart, R. S. (1992), SpaceTime Variability of the Deep Western Boundary Current Oxygen Core, *Journal of Physical Oceanography*, *22*(9), 1047–1061, doi:10.1175/1520-0485(1992)022⟨1047:SVOTDW⟩2.0.CO;2. 21, 71

Price, J. F., R. A. Weller, and R. R. Schudlich (1987), Wind-Driven Ocean Currents and Ekman Transport, *Science*, *238*(4833), 1534–1538, doi:10.1126/science.238.4833.1534. 27, 50

Rabe, B., F. a. Schott, and A. Köhl (2008), Mean Circulation and Variability of the Tropical Atlantic during 19522001 in the GECCO Assimilation Fields, *Journal of Physical Oceanography*, *38*(1), 177–192, doi:10.1175/2007JPO3541.1. 25

Rahmstorf, S., et al. (2005), Thermohaline circulation hysteresis: A model intercomparison, *Geophysical Research Letters*, *32*(23), L23,605, doi:10.1029/2005GL023655. 17

Rahmstorf, S., J. E. Box, G. Feulner, M. E. Mann, A. Robinson, S. Rutherford, and E. J. Schaffernicht (2015), Exceptional twentieth-century slowdown in Atlantic Ocean overturning circulation, *Nature Climate Change*, *5*(5), 475–480, doi:10.1038/nclimate2554. 17

Roach, A. T., K. Aagaard, C. H. Pease, S. A. Salo, T. Weingartner, V. Pavlov, and M. Kulakov (1995), Direct measurements of transport and water properties through the Bering Strait, *Journal of Geophysical Research*, *100*(95), 1844–18,457, doi:10.1029/95JC01673. 76

Roberts, C. D., et al. (2013), Atmosphere drives recent interannual variability of the Atlantic meridional overturning circulation at 26.5N, *Geophysical Research Letters*, *40*(19), 5164–5170, doi:10.1002/grl.50930. 16, 18

Roemmich, D., and J. Gilson (2009), The 20042008 mean and annual cycle of temperature, salinity, and steric height in the global ocean from the Argo Program, *Progress in Oceanography*, *82*(2), 81–100, doi:10.1016/j.pocean.2009.03.004. 40

Roemmich, D., and C. Wunsch (1985), Two transatlantic sections : meridional circulation and heat flux in the subtropical North Atlantic Ocean, *Deep Sea Research*, *32*(6). 11, 60, 61, 64, 71

Rosón, G., A. F. Ríos, F. F. Pérez, A. Lavin, and H. L. Bryden (2003), Carbon distribution, fluxes and budgets in the subtropical North Atlantic Ocean (24.5N), *Journal of Geophysical Research*, *108*, 3144, doi:10.1029/1999JC000047. 93

Rudnick, D. L., and J. Klinke (2007), The underway conductivity-temperature-depth instrument, *Journal of Atmospheric and Oceanic Technology*, *24*(11), 1910–1923, doi:10.1175/JTECH2100.1. 32, 34

Sarafanov, A., A. Sokov, and A. Demidov (2007), Water mass characteristics in the equatorial North Atlantic: A section nominally along 6.5N, July 2000, *Journal of Geophysical Research: Oceans*, *112*(12), 1–11, doi: 10.1029/2007JC004222. 98, 109

Sarafanov, A., A. Demidov, and A. Sokov (2008), On the warming of intermediate and deep waters in the equatorial North Atlantic, *Russian Meteorology and Hydrology*, *33*(3), 175–179, doi:10.3103/S1068373908030060. 21, 70, 98, 104, 105

Sato, O. T., and P. S. Polito (2005), Comparison of the Global Meridional Ekman Heat Flux Estimated from Four Wind Sources, *Journal of Physical Oceanography*, *35*(1), 94–108, doi:10.1175/JPO-2665.1. 53

Schmid, C., and S. L. Garzoli (2009), New observations of the spreading and variability of the Antartic Intermediate Water in the Atlantic, *Journal of Marine Research*, *67*, 815–843. 110

Schmid, C., G. Siedler, and W. Zenk (2000), Dynamics of Intermediate Water Circulation in the Subtropical South Atlantic*, *Journal of Physical Oceanography*, *30*(12), 3191–3211, doi:10.1175/1520-0485(2000)030⟨3191:DOIWCI⟩2.0.CO;2. 110

Schmidtko, S., and G. C. Johnson (2012), Multidecadal warming and shoaling of antarctic intermediate water, *Journal of Climate*, *25*(1), 207–221, doi:10.1175/JCLI-D-11-00021.1. 21, 22, 70, 98, 104, 109, 110

Schott, F. A., J. P. McCreary, and G. C. Johnson (2004), Shallow Overturning Circulations of the Tropical-Subtropical Oceans, *Earth's Climate*, pp. 261–304, doi:10.1029/147GM15. 25, 55, 68

Schott, F. A., M. Dengler, R. Zantopp, L. Stramma, J. Fischer, and P. Brandt (2005), The Shallow and Deep Western Boundary Circulation of the South Atlantic at 511S, *Journal of Physical Oceanography*, *35*(11), 2031–2053, doi:10.1175/JPO2813.1. 42

Send, U., M. Lankhorst, and T. Kanzow (2011), Observation of decadal change in the Atlantic meridional overturning circulation using 10 years of continuous transport data, *Geophysical Research Letters*, *38*(24), 1–5, doi:10.1029/2011GL049801. 15, 60, 89, 95, 96, 100, 106

Sloyan, B. M., and S. R. Rintoul (2001), The Southern Ocean Limb of the Global Deep Overturning Circulation*, *Journal of Physical Oceanography*, *31*(1), 143–173, doi:10.1175/1520-0485(2001)031⟨0143:TSOLOT⟩2.0.CO;2. 11, 73, 80

Smeed, D., G. McCarthy, D. Rayner, B. I. Moat, W. E. Johns, M. O. Baringer, and C. S. Meinen (2016), Atlantic meridional overturning circulation observed by the RAPID-MOCHA-WBTS (RAPID-Meridional Overturning Circulation and Heatflux Array-Western Boundary Time Series) array at 26N from 2004 to 2015., doi:10.5285/35784047-9B82-2160-E053-6C86ABC0C91B. 93

Smeed, D. A., et al. (2014), Observed decline of the Atlantic meridional overturning circulation 2004-2012, doi:10.5194/os-10-29-2014. 14, 15, 60, 95, 96, 100, 106, 107

Smethie, W. M., R. A. Fine, A. Putzka, and E. P. Jones (2000), Tracing the flow of North Atlantic Deep Water using chlorofluorocarbons, *Journal of Geophysical Research: Oceans*, *105*(C6), 14,297–14,323, doi: 10.1029/1999JC900274. 21, 71

Smith, S. D. (1988), Coefficients for sea surface wind stress, heat flux, and wind profiles as a function of wind speed and temperature, *Journal of Geophysical Research: Oceans*, *93*(C12), 15,467–15,472, doi:10.1029/ JC093iC12p15467. 35

Smyth, W. D., T. S. Durland, and J. N. Moum (2015), Energy and heat fluxes due to vertically propagating Yanai waves observed in the equatorial Indian Ocean, *Journal of Geophysical Research: Oceans*, *120*(1), 1–15, doi:10.1002/2014JC010152. 46

Speer, K. G., and M. S. McCartney (1991), Tracing lower North Atlantic deep water across the equator, *Journal of Geophysical Research*, *96*(C11), 20,443, doi:10.1029/91JC01878. 90, 99

Stramma, L., S. Schmidtko, L. A. Levin, and G. C. Johnson (2010), Ocean oxygen minima expansions and their biological impacts, *Deep-Sea Research Part I: Oceanographic Research Papers*, *57*(4), 587–595, doi: 10.1016/j.dsr.2010.01.005. 68

Takahashi, T., et al. (2009), Climatological mean and decadal change in surface ocean pCO2, and net sea-air CO2 flux over the global oceans, *Deep-Sea Research Part II: Topical Studies in Oceanography*, *56*(8-10), 554–577, doi:10.1016/j.dsr2.2008.12.009. 9

Talley, L. D. (2003), Shallow, Intermediate, and Deep Overturning Components of the Global Heat Budget, *Journal of Physical Oceanography*, *33*(3), 530–560, doi:10.1175/1520-0485(2003)033⟨0530:SIADOC⟩2.0.CO;2. 11

Talley, L. D., and M. S. McCartney (1982), Distribution and Circulation of Labrador Sea Water, doi:10.1175/ 1520-0485(1982)012⟨1189:DACOLS⟩2.0.CO;2. 21, 71

Talley, L. D., G. L. Pickard, W. J. Emery, and J. H. O. Swift (2011), *Descriptive physical oceanography : an introduction*, sixth edit ed., 555 pp., Academic Press, Boston. 20, 21, 41

Tsubouchi, T., et al. (2012), The Arctic Ocean in summer: A quasi-synoptic inverse estimate of boundary fluxes and water mass transformation, *Journal of Geophysical Research: Oceans*, *117*(1), C01,024, doi:10.1029/2011JC007,174, doi:10.1029/2011JC007174. 13, 73, 79, 91

Tsuchiya, M. (1989), Circulation of the Antarctic Intermediate Water in the North Atlantic Ocean, *Journal of Marine Research*, *47*(4), 747–755, doi:10.1357/002224089785076136. 21, 69

Ullman, D. S., and D. Hebert (2014), Processing of underway CTD data, *Journal of Atmospheric and Oceanic Technology*, *31*(4), 984–998, doi:10.1175/JTECH-D-13-00200.1. 31, 107

van Sebille, E., M. O. Baringer, W. E. Johns, C. S. Meinen, L. M. Beal, M. F. de Jong, and H. M. van Aken (2011), Propagation pathways of classical Labrador Sea water from its source region to 26N, *Journal of Geophysical Research*, *116*(C12), C12,027, doi:10.1029/2011JC007171. 96

Visbeck, M. (2002), Deep Velocity Profiling Using Lowered Acoustic Doppler Current Profilers: Bottom Track and Inverse Solutions*, *Journal of Atmospheric and Oceanic Technology*, *19*(5), 794–807, doi: 10.1175/1520-0426(2002)019⟨0794:DVPULA⟩2.0.CO;2. 63

Wang, C., and L. Zhang (2013), Multidecadal ocean temperature and salinity variability in the tropical north atlantic: Linking with the AMO, AMOC, and subtropical cell, *Journal of Climate*, *26*(16), 6137–6162, doi: 10.1175/JCLI-D-12-00721.1. 16

Wang, W., and R. Huang (2004), Wind Energy Input to the Ekman Layer*, *Journal of physical oceanography*, *34*, 1267–1275. 28

Watanabe, M., and T. Hibiya (2002), Global estimates of the wind-induced energy flux to inertial motions in the surface mixed layer, *Geophysical Research Letters*, *29(8)*(8), 1239, doi:10.1029/2001GL014422. 28

Wijffels, S., E. Firing, and H. L. Bryden (1994), Direct Observations of the Ekman Balance at 10N in the Pacific, *Journal of Physical Oceanography*, *24*(7), 1666–1679, doi:10.1175/1520-0485(1994)024⟨1666:DOOTEB⟩2.0.CO;2. 18, 26, 27, 37, 38, 48, 49, 50, 54, 55, 56, 102, 103, 108

Wijffels, S. E., R. W. Schmitt, H. L. Bryden, and A. Stigebrandt (1992), Transport of Freshwater by the Oceans, *Journal of Physical Oceanography*, *22*(2), 155–162, doi:10.1175/1520-0485(1992)022⟨0155:TOFBTO⟩2.0.CO;2. 93

Wijffels, S. E., J. M. Toole, H. L. Bryden, R. A. Fine, W. J. Jenkins, and J. L. Bullister (1996), The water masses and circulation at 10N in the Pacific, *Deep Sea Research Part I: Oceanographic Research Papers*, *43*(4), 501–544, doi:10.1016/0967-0637(96)00006-4. 26, 41

Wilburn, A. M., E. Johns, and M. Bushnell (1990), Current velocity and hydrographic observa- tions in the southwestern North Atlantic Ocean: Subtropical Atlantic Climate Studies (STACS), 1989, *NOAA Data Report ERL AOML-18*, p. 97. 63

Willis, J. K. (2010), Can in situ floats and satellite altimeters detect long-term changes in Atlantic Ocean overturning?, *Geophysical Research Letters*, *37*(6), n/a–n/a, doi:10.1029/2010GL042372. 12

Woodgate, R. A., K. Aagaard, and T. J. Weingartner (2005), Monthly temperature, salinity, and transport variability of the Bering Strait through flow, *Geophysical Research Letters*, *32*(4), doi:10.1029/2004GL021880. 76

Wunsch, C. (1977), Determining the general circulation of the oceans: a preliminary discussion., *Science (New York, N.Y.)*, *196*(4292), 871–875, doi:10.1126/science.196.4292.871. 13, 61

Wunsch, C. (1978), The North Atlantic general circulation west of 50W determined by inverse methods, *Reviews of Geophysics*, *16*(4), 583–620, doi:10.1029/RG016i004p00583. 11

Wunsch, C. (1996), *The ocean circulation inverse problem*, 442 pp., Cambridge University Press. 13, 61, 80

Wunsch, C. (2005), The Total Meridional Heat Flux and Its Oceanic and Atmospheric Partition, *Journal of Climate*, *18*(21), 4374–4380, doi:10.1175/JCLI3539.1. 59

Wunsch, C., and P. Heimbach (2009), The Global Zonally Integrated Ocean Circulation, 19922006: Seasonal and Decadal Variability, *Journal of Physical Oceanography*, *39*(2), 351–368, doi:10.1175/2008JPO4012.1. 16

Wunsch, C., and P. Heimbach (2013), Dynamically and kinematically consistent global ocean circulation and ice state estimates, *International Geophysics*, *103*, 553–579, doi:10.1016/B978-0-12-391851-2.00021-0. 16

Wunsch, C. I., and P. Heimbach (2006), Estimated decadal changes in the North Atlantic Meridional overturning circulation and heat flux 1993-2004, *Journal of Physical Oceanography*, *36*, 2013–2024, doi:10.1175/JPO2957.1. 35, 76

Wüst, G. (1935), Schichtung und Zirkulation des Atlantischen Ozeans, Die Stratophäre, in *Wissenschaftliche Ergebnisse der Deutschen Atlantischen Expedition auf dem Forschungs- und Vermessungsschiff "Meteor" 1925-1927*, vol. 6, p. 180, Berlin. 10, 21, 72

Wüst, G. (1949), Die Kreisläufe der atlantischen Wassermassen, ein neuer Versuch räumlicher Darstellung, *Forschungen und Fortschritte*, *25*, 285–289. 10

Wüst, G. (1957), Stromgeschwindigkeiten und Strommengen in den Tiefen des Atlantischen Ozeans unter besonderer Berücksichtigung des Tiefen- und Bodenwassers, in *Wissenschaftliche Ergebnisse der Deutschen Atlantischen Expedition auf dem Forschungs—und Vermessungsschiff "Meteor" 1925–1927*, vol. 6, second, chap. second par, p. 180, Berlin. 10

Zantopp, R., J. Fischer, M. Visbeck, and J. Karstensen (2017), From interannual to decadal: 17 years of boundary current transports at the exit of the Labrador Sea, *Journal of Geophysical Research: Oceans*, *122*(3), 1724–1748, doi:10.1002/2016JC012271. 100

Zhang, J., and D. Rothrock (2000), Modeling Arctic sea ice with an efficient plastic solution, *Journal of Geophysical Research*, *105*(C2), 3325, doi:10.1029/1999JC900320. 35

Zweng, M. M., et al. (2013), World Ocean Atlas 2013, Volume 2: Salinity, *Tech. Rep. 1*, doi:10.1182/blood-2011-06-357442. 39

5 Acknowledgements

First of all, I would like to thank Johannes Karstensen and Peter Brandt for their support, help, and instruction during my P.h.D. work. I appreciate profoundly the experience working with them, during which I learned how they dealt with and solved problems professionally and scientifically. I have benefit a lot from their thorough knowledge and deep understanding of the ocean. I am grateful for their considerateness, patience, and trust.

Special thanks to my friends and colleagues in the PO, Robert Kopte, Florian Schütte, Johannes Hahn, Josefine Herrford, Rebecca Hummels, Tim Fischer, Sören Thomsen, Kristin Burmeister, Marilena Oltmanns, Patricia Handmann, Philip Tuchen, Thilo Klenz, Jan Lüdke, Sunke Schmidtko, Yunchang He, and many others, for the useful discussion and memorable time we had during daily work, at sea, and many many other occasions. I am very grateful to Robert, Josefine, Philip, Yunchang and Marilena for reading the my thesis and their helpful comments and suggestions.

I would also thank Richard Greatbatch, Martin Claus, and Hui Ding for their help during my master study, which has laid an important foundation in my research knowledge and skills. Thanks also go to Takamasa Tsubouchi for his instruction on the box inverse model. Without his help it would be very difficult to conduct the inverse study of this work.

Particularly, I would like to thank my parents, for their generous support for my study in Germany. Your love, understanding, respect, and motivation are most valuable for every important decision I made.

In the end, to my wife Qian, thank you so much for your support and patience with me all the way. Without you I would not have made this far. And to my son Zhuangzhuang, you are a gift, you made me more concentrate, taught me to distribute my time more efficiently. And hopefully you would also be interested in science in the future.

Erklärung

Hiermit erkläre ich, dass ich die vorliegende Arbeit - abgesehen von der Beratung durch den Betreuer Prof. Dr. Peter Brandt - selbstandig erarbeitet und verfasst. Die Arbeit hat weder ganz noch zum Teil schon einer anderen Stelle im Rahmen eines Prüfungsverfahrens vorgelegen, ist nicht veröffentlicht und auch nicht zur Veröffentlichung eingereicht. Sie ist unter Einhaltung der Regeln guter wissenschaftlicher Praxis der Deutschen Forschungsgemeinschaft entstanden.

Kiel, 2017 _____

Yao Fu